JOHANNES GUTENBERG
UNIVERSITÄT MAINZ

Dissertation zur Erlangung des akademischen Grades
"**Doktor der Naturwissenschaften**"
im Promotionsfach Chemie

am Fachbereich Chemie, Pharmazie und Geowissenschaften
der Johannes Gutenberg-Universität Mainz

In-situ Characterization of Surface Restructuring and Molecular Self-Assembly at the Calcite-Water Interface

Martin Matthias Nalbach

geboren in Neuwied

Mainz, den 16. Oktober 2017

This thesis was supervised by [redacted] and was carried out at the Institute of Physical Chemistry at the Johannes Gutenberg-Universität Mainz from October 2014 to September 2017.

D77 (Dissertation Johannes Gutenberg-Universität Mainz)

Dean of the Faculty	[redacted]
1st report	[redacted] Johannes Gutenberg-Universität Mainz
2nd report	[redacted] Max-Planck-Institut for Polymerforschung
Submitted:	October 16th, 2017
Oral examination:	November 20th, 2017

Für meine Familie

> *End? No, the journey doesn't end here. All we have to decide is what to do with the time that is given us. Look to my coming, at first light, on the fifth day. At dawn, look to the East.*
>
> **— Gandalf**

Contents

I Introduction 1

1 Introduction 3

II *In-situ* Dynamic Atomic Force Microscopy 7

2 *In-situ* Dynamic Atomic Force Microscopy 9
2.1 Atomic Force Microscopy 9
2.2 *In-situ* Atomic Force Microscopy Setup 12
2.3 Instrumentation 15
2.4 Measurement Conditions 15

III Organic Molecules at the Calcite (10.4)-Water Interface 17

3 Organophosphonate-Induced Calcite (10.4) Surface Restructuring 19
3.1 Introduction - Organophosphonates 21
3.2 Results and Discussion - Organophosphonates 24
3.3 Summary and Conclusion - Organophosphonates 30

4 Molecular Self-Assembly Versus Surface Restructuring 33
4.1 Introduction - Eriochrome Azo Dyes 34
4.2 Results and Discussion - Eriochrome Azo Dyes 36
4.3 Summary and Conclusion - Eriochrome Azo Dyes 45

5 Controlling Molecular Self-Assembly on Calcite (10.4) 47
5.1 Introduction - Benzopurpurine 48
5.2 Results and Discussion I - Benzopurpurine 50

6 Benzopurpurine Self-Assembly at the Calcite (10.4)-Water Interface 59
6.1 Molecular Dynamics Setup - Benzopurpurine 60
6.2 Results and Discussion II - Benzopurpurine 62
6.3 Summary and Conclusion - Benzopurpurine 73

IV Calcite Nucleation and Growth **75**

7 Influence of Initial pH on Calcite Nucleation and Growth **77**
7.1 Introduction - Ammonia Diffusion Method 78
7.2 Instrumentation - Ammonia Diffusion Method 80
7.3 Results and Discussion 81
7.4 Summary and Conclusion 87

V Summary **89**

8 Summary **91**

Bibliography **93**

List of Figures **103**

List of Tables **105**

List of Acronyms **107**

Publications & Contributions **109**

Acknowledgment **115**

Part I

Introduction

1 Introduction

The Calcite-Water Interface...
... in the Presence of Organic Molecules

Mineral–water interfaces are everywhere:[1] from the separation of continents by oceans, the formation of coral reefs to the growth of speleothems, mineral–water interfaces are ubiquitous on the Earth's surface. Reactions occurring at the interface between minerals and aqueous solutions are of tremendous importance for a wide range of natural and technological processes, such as: dissolution and growth, precipitation, weathering and soil production.[2–5] In this thesis, I particularly focus on calcite, the most thermodynamically stable polymorph of calcium carbonate ($CaCO_3$) and an omnipresent rock-forming[6,7] and biogenic[8] mineral. Due to its abundance in the Earth's crust, the calcite-water interface is of utmost interest for a wide range of geochemical processes,[9] synthetic[10,11] and industrial systems.[12]

Organic molecules at mineral-water interfaces are known to alter the morphology and composition of the interface in various ways. Hence, the presence of organic additives exhibits a decisive influence on dynamic processes on the surface, such as: dissolution, growth, surface restructuring, mineral replacement and molecular self-assembly.[13–19] Especially for calcite, the impact of organic additives in biomineralization,[20,21] scale inhibition[22] and decalcification[23,24] has been studied extensively with experimental, as well as with computational techniques.[25,26] Nevertheless, very little is known about the detailed mode of action of organic molecules at interfaces and a comprehensive molecular understanding of surface processes (*e.g.* adsorption and molecular self-assembly) is still missing.

The aim of this thesis is therefore to characterize interfacial interactions of organic molecules at the nanoscale and therewith to contribute to a molecular-scale knowledge of the composition of mineral-water interfaces. In particular, I systematically elucidate the impact of organophosphonates and organic azo dyes on the calcite (10.4)-water interface. Both classes of organic molecules have been chosen as they are well-known to strongly interact with the surfaces and ions of various minerals and hence, are extensively used as scale growth inhibitors or for water hardness determination.[27,28]

Atomic force microscopy (AFM) has been proven to be the ideal tool for investigating surfaces and interfaces in real space and with atomic precision, even in liquid environment.[29] Using *in-situ* high-resolution dynamic AFM, I focus specifically on two dynamic interfacial processes: molecule-induced surface restructuring of the dissolving calcite (10.4) surface and molecule adsorption of the organic additives onto the calcite (10.4) substrate and subsequent their self-assembly into ordered structures.

The mode of action of all investigated additive molecules is studied through the variation of different functional groups and structural patterns, as well as the molecule concentration, solution pH and calcium ion concentration. My results demonstrate that the interplay of surface restructuring and molecular self-assembly in the complex environment of a mineral-water interface is the result of the subtle balance between molecule-molecule, molecule-surface, molecule-water, surface-water and water-water interactions. For the twelve molecules studied in this thesis, I provide nanoscopic insights into adsorption, structure formation and surface restructuring processes on and of the calcite (10.4) surface. Furthermore, for the first time, results from molecular dynamic (MD) simulations highlight the decisive impact of the hydration structure on interfacial processes in the presence of organic molecules. The latter finding emphasizes the impact of considering the entire interface rather than only the mineral surface when studying the impact of organic molecules.

Thesis Structure

In this thesis, the calcite (10.4)-water interface is characterized in the presence of organic molecules using *in-situ* high-resolution dynamic AFM. Therefore, I will briefly outline the theoretical foundations of dynamic AFM in chapter 2. Moreover, I will describe in detail the used experimental *in-situ* AFM setup, the measurement conditions, as well as the sample preparation procedure in section 2.2, section 2.3 and section 2.4.

In chapter 3, the influence of both the size of an additive molecule, as well as its number of functional groups on the surface restructuring process of calcite (10.4) is explored. I systematically study the impact of six different organophosphonate molecules (three tetraphosphonates and three disphophonates) on the calcite (10.4) dissolution process. For each molecule, a very pronounced restructuring of the calcite (10.4) surface is observed, resulting in the formation of characteristically shaped etch pits.

The complex interplay of surface restructuring and molecular self-assembly at the calcite (10.4)-water interface is elucidated for five different organic molecules from the class of Eriochrome azo dyes in chapter 4. Here, I demonstrate that the ability to restructure the calcite (10.4) surface by the adsorption to specific step edges during calcite dissolution appears to be a general property of these molecules, irrespective of the specific molecular structure, conformation, protonation and deprotonation state. In contrast, the formation of self-assembled structures on calcite (10.4) terraces is observed for only one out of the five Eriochrome azo dyes.

For the specific example of the organic azo dye molecule Benzopurpurine 4B (BPP), I discuss the formation of well-ordered molecular islands on the calcite (10.4) substrate in chapter 5. Furthermore, for the first time, the results demonstrate three possibilities regarding how the adsorption of BPP molecules and the formation of the well-ordered molecular islands on calcite (10.4) can be systematically controlled. By varying the molecule concentration, the pH and the concentration of calcium ions in the solution, the coverage of BPP molecules adsorbed onto calcite (10.4), as well as the timescale of the molecule adsorption and island growth processes can be precisely controlled.

The decisive impact of the hydration structure on the adsorption behavior of organic molecules and subsequent their self-assembly at the calcite (10.4)-water interface is highlighted and discussed in chapter 6. MD simulations reveal that BPP adsorbs at the interface, but is not in direct contact with the calcite (10.4) surface. Instead, the molecules adsorb onto the second hydration layer, which seems to be the most hydrophobic region in the system. This somewhat surprising finding is corroborated by comparing the results with other mineral surfaces that exhibit different interfacial hydration structures.

Finally, in chapter 7, I explore the nucleation and growth process of calcite using the ammonia diffusion method (ADM). By varying the starting pH of the crystallization solution, I study the impact of the initial pH on the resulting calcite crystal number and size. The results disclose a decisive dependence on the pH, as the calcite crystal number and size can be directly controlled by changing the initial pH.

Part II

In-situ Dynamic Atomic Force Microscopy

2 *In-situ* Dynamic Atomic Force Microscopy

2.1 Atomic Force Microscopy

The atomic force microscope (AFM) was invented by Binnig, Quate and Gerber in 1986 to resolve the atomic surface structure of bulk insulators.[30] In AFM, a very sharp tip (ideally an atomically sharp tip), mounted at the free end of a so-called cantilever, is scanned in close proximity above a sample surface. Forces (attractive and repulsive in origin) acting on the tip cause a deflection of the cantilever. The detection and analysis of the resulting deflection finally provides information about the tip-sample force. The detection of the cantilever deflection is often realized by using a laser beam, which is focused on the free end of the cantilever and from there reflected to a position-sensitive detector (PSD).[31]

Dynamic Atomic Force Microscopy

Since the invention of AFM, a variety of different dynamic operation modes have been implemented.[32] In all dynamic AFM modes, the cantilever is excited with an external excitation force F_{exc}, causing the cantilever to move (eq. (2.1)).

$$F_{\mathrm{exc}} = F_0 \cdot \cos(2\pi\nu_{\mathrm{exc}}t) \tag{2.1}$$

In eq. (2.1), F_0 represents the excitation force amplitude, ν_{exc} the excitation frequency and t the time. The movement of the cantilever, as a consequence of the excitation, can be expressed through its deflection q (eq. (2.2)), as well as the tip-sample distance z_{ts} (eq. (2.3)).

$$q = q_{\mathrm{s}} + A \cdot \cos(2\pi\nu_{\mathrm{exc}}t + \varphi) \tag{2.2}$$

$$z_{\mathrm{ts}} = z_{\mathrm{c}} + A \cdot \cos(2\pi\nu_{\mathrm{exc}}t + \varphi) \tag{2.3}$$

Here, q_s is the static deflection of the cantilever, z_c its center position, A the amplitude of the cantilever oscillation and φ the corresponding phase shift. The two equations, eq. (2.2) and eq. (2.3) are the harmonic approximation.[33] The latter implies that at all times of a dynamic AFM experiment, the oscillating cantilever is in a steady state, *i.e.* all observables q_s, A, φ, as well as ν_{exc} and F_0 are constant and the velocity of the cantilever is given by $\dot{z}_{ts} = \dot{q}$.

Hence, the movement of the cantilever can be described with three observables only: the static deflection q_s, the amplitude A and phase shift φ.[33] In practicality, the three observables result in at least four different dynamic AFM operation modes, in which either the excitation parameters (F_0 and ν_{exc}), as well as the three observables (q_s, A and φ) are kept constant or are varied, respectively.

In-situ dynamic AFM is used in this thesis as it allows for imaging surfaces and molecular structures with true atomic[34] and molecular resolution.[35] Compared to static AFM, the vertical movement of the cantilever significantly reduces lateral friction forces,[35] which enables to probe very sensitively even weakly bound molecular structures on surfaces.

Frequency Modulation Atomic Force Microscopy

The main body of AFM experiments in this thesis is conducted using the dynamic frequency modulation AFM (FM-AFM) mode.[36] As in all dynamic AFM modes, the cantilever is externally excited with F_{exc} in FM-AFM. Through the implementation of three feedback loops, the amplitude and the phase shift of the cantilever oscillation are kept constant, while the excitation force amplitude and the excitation frequency are given by these feedback loops and q_s results from the measurement. All FM-AFM measurements in this thesis are performed in the constant frequency shift mode. In this operating mode, the main measuring parameter is the excitation frequency ν_{exc}, while a predetermined frequency shift $\nu_{exc} - \nu_e$ (ν_e being the eigenfrequency of the cantilever, determined far away from the sample surface) is kept constant by adjusting the z-position of the cantilever z_p. In addition to the excitation frequency ν_{exc}, the z-position of the cantilever z_p, the amplitude A and phase shift φ of the cantilever oscillation and F_0 are measured signals.

The working principle of FM-AFM is illustrated in fig. 2.1. Far away from the sample surface, the cantilever is excited with F_0 and ν_e. Reducing the tip-sample distance creates forces from tip-sample interactions, which affect the oscillating cantilever. The forces acting on the cantilever result in a change of the oscillation properties. The dynamic deflection signal is detected *via* the optical beam deflection technique and converted into electronic signals.

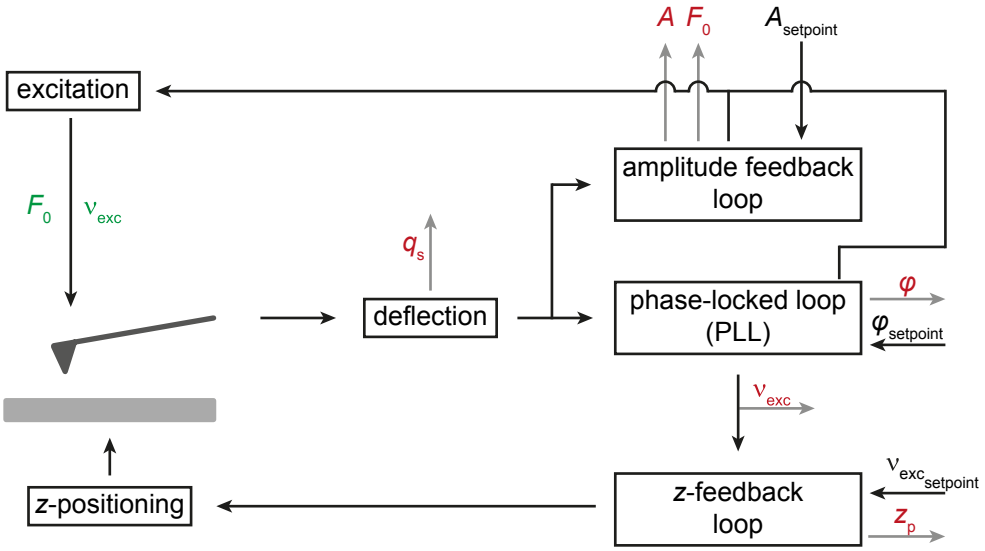

Fig. 2.1: Schematic drawing of the FM-AFM setup. The excitation parameters F_0 and ν_{exc} are displayed in green, the reference setpoints A_{setpoint}, $\varphi_{\text{setpoint}}$ and $\nu_{\text{exc}_{\text{setpoint}}}$ are highlighted in black and the measuring signals z_{p}, ν_{exc}, q_{s}, A, φ and F_0 are illustrated in red.

On the one hand, the signals are fed into a phase-locked loop (PLL), which determines the phase shift of the current cantilever oscillation. Furthermore, the PLL compares the detected phase shift to a phase shift setpoint $\varphi_{\text{setpoint}}$. Usually the phase shift setpoint is set to be at $-\pi/2$.[33] If the measured phase shift is dissimilar to the reference phase shift, the PLL adjusts the excitation frequency to maintain the constant phase shift. The new excitation frequency is then used to excite the cantilever, as well as to feed into a z-feedback loop. The z-feedback loop adjusts the tip-sample distance to maintain the frequency shift $\nu_{\text{exc}} - \nu_{\text{e}}$ at a constant set point $\nu_{\text{exc}_{\text{setpoint}}}$ which is picked by the experimentalist.

On the other hand, the dynamic deflection signals are also fed into an amplitude feedback loop. This feedback loop determines the amplitude of the current cantilever oscillation. Similar to the PLL, the amplitude feedback loop compares the measured amplitude to an amplitude setpoint $A_{setpoint}$, picked by the experimentalist. A discrepancy causes the amplitude feedback loop to adjust the excitation force amplitude. The new excitation force amplitude is subsequently used to excite the cantilever.

2.2 *In-situ* Atomic Force Microscopy Setup

All measurements presented in this thesis are conducted at a constant temperature of 28 °C with a commercial AFM from Bruker Corporation (MultiMode V with Nanoscope V controller) that has been modified for *in-situ* high-resolution imaging. Besides a rigorous noise reduction,[37] photothermal excitation has been implemented[38] to avoid the problem with the so-called "forest of peaks".[39] The *in-situ* AFM setup, including the home-built isolation chamber, as well as a detailed view on the home-built AFM scanhead are shown in fig. 2.2.

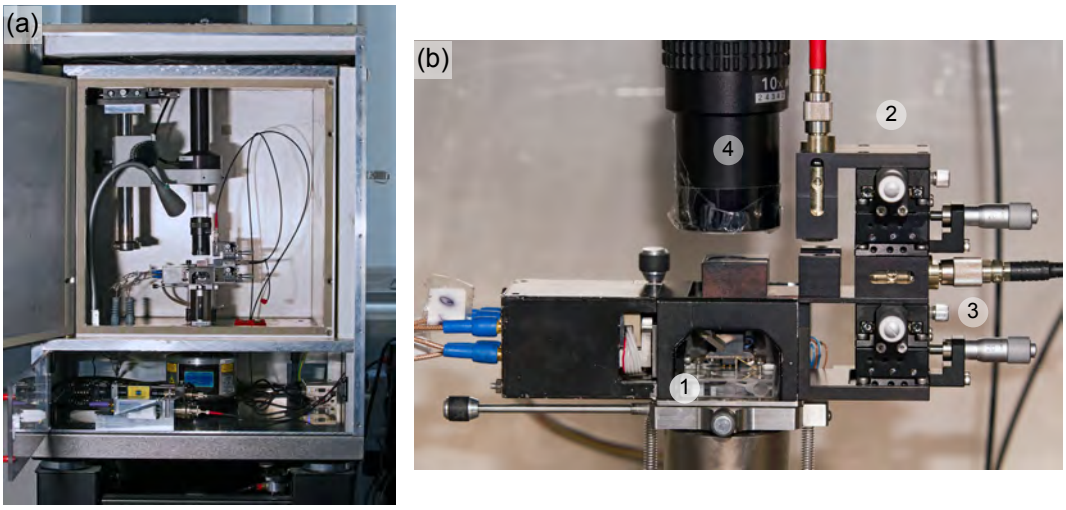

Fig. 2.2: AFM setup for *in-situ* high-resolution imaging. (a) Home-built isolation chamber with air suspension. (b) Home-built AFM scanhead.[38] The main components are (1) the sample holder and liquid cell, (2) the excitation laser and (3) the detection laser input coupling. An overhead magnifying camera (4) enables the laser alignments, as well as the sample adjustments.

AFM Liquid Cell

AFM liquid cells from Bruker Nano Surfaces Division are used in two modifications, an open and a closed cell system (fig. 2.3). The commercially available liquid cell without any additional components is called the open cell system as the injected solution is in contact with air at all times (fig. 2.3, left liquid cell). Due to its easy handling when mounting and during tip approach, the open cell system is used for most of the experiments in this thesis. The injection volume ranges from $0.2\,\mathrm{ml}$ to $0.3\,\mathrm{ml}$ and is injected into the liquid cell *via* a syringe. All *in-situ* solution exchange experiments are conducted using the closed cell system (fig. 2.3, right liquid cell). For closing the cell system an O-ring is carefully fitted into the notch around the cantilever holder. The O-ring locks up the space between the sample holder and the liquid cell preventing the contact of the solution with air. In- and outlet tubes enable a continuous re-filling and exchange of solutions during the *in-situ* AFM experiments. As the O-ring hampers the view onto the cantilever-sample surface distance, care has

to be taken when approaching the sample holder. Furthermore, too much pressure of the O-ring onto the sample holder can cause image distortion during large scan area changes. This is why the closed cell system is only used when conducting *in-situ* solution exchange experiments.

Fig. 2.3: AFM liquid cells from Bruker Nano Surfaces Division. Open cell system (left) and closed cell system with O-ring and in- and outlet tubing (right).

Cantilever

The *in-situ* AFM experiments are conducted using two types of gold-coated and p-doped silicon cantilevers, PPP-NCHAuD from Nanosensors and Tap300GD-G from BudgetSensors. The cantilevers exhibit a typical eigenfrequency of 100-150 kHz in liquids, a spring constant of approximately 40 N/m, as well as a quality factor of 7-10.

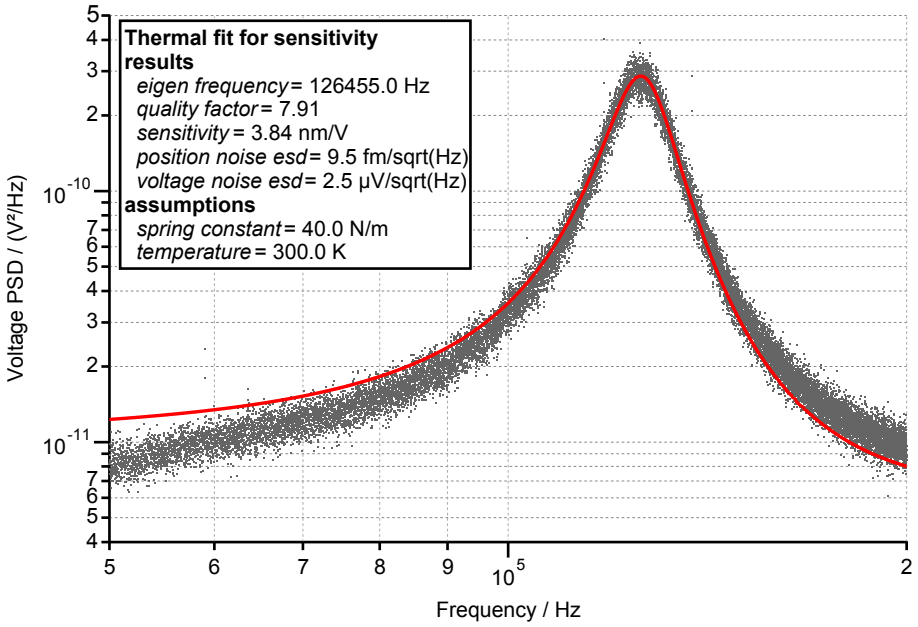

Fig. 2.4: Representative thermal noise spectrum obtained for a PPP-NCHAuD cantilever from Nanosensors in an aqueous solution far away from the sample surface.

After injecting the solution into the liquid cell, a thermal noise spectrum is obtained for each cantilever far away from the sample surface using the digital lock-in amplifier HF2LI from Zurich Instruments. The analysis of the cantilever resonance curve reveals the eigenfrequency of the cantilevers, as well as its quality factor. A representative thermal noise spectrum for a PPP-NCHAuD cantilever from Nanosensors is shown in fig. 2.4. The oscillation amplitude of the cantilever is adjusted during the *in-situ* AFM measurements to be between 0.1 and $1\,\mathrm{nm}$.

Calcite Crystal Sample Holder

All *in-situ* AFM measurements are conducted on calcite crystals with a sample size of 4 x 4 mm^2. The crystals are purchased from Korth Kristalle GmbH and cut into the desired orientation by Vario Kristallbearbeitung GmbH.

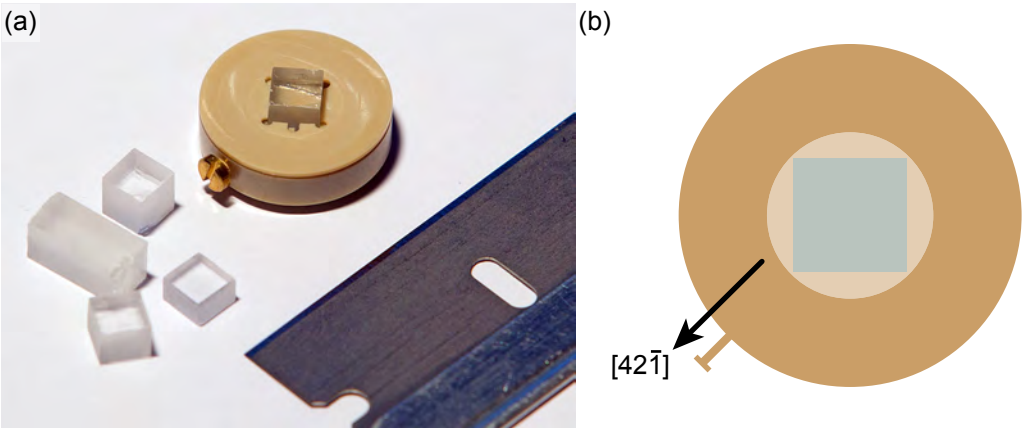

Fig. 2.5: (a) Home-built sample holder for calcite crystals with a sample size of 4 x 4 mm^2. (b) Schematic drawing illustrating the crystallographic orientation of the calcite crystal mounted into the sample holder.

The calcite crystals are placed in a home-built calcite crystal sample holder (fig. 2.5 a) made out of polyether ether ketone (PEEK). Prior to each experiment, the calcite crystals are freshly cleaved with a razor blade and cleaned under a nitrogen flow. The absolute orientation of the calcite (10.4) surface is determined by evaluating the birefringence of calcite. A (10.4) projected split vector between the ordinary and extraordinary ray proceeds exactly along the [42$\bar{1}$] direction.[40] After identifying the [42$\bar{1}$] direction, the calcite crystals are placed in the sample holder so that the [42$\bar{1}$] direction points exactly towards the locking screw of the sample holder (fig. 2.5 b). The knowledge of the absolute orientation is essential for assigning the correct directions of the calcite (10.4) surface in the obtained AFM images.

The cutting and mounting process of the calcite crystals often causes a slightly inclined plane. Therefore, the AFM scan angle is always adjusted to almost minimize the height difference in the fast scan direction.

2.3 Instrumentation

Sample Preparation

Pure water (18 MΩ·cm) is produced using a purification setup from Merck Millipore. Sodium hydroxide (NaOH, 0.1 M and 1 M) and hydrochloric acid (HCl, 0.1 M and 1 M) standard solutions are purchased from Carl Roth GmbH & Co. KG and are used to adjust the pH of the solutions. For varying the calcium concentration in the solutions, I use a calcium ion solution ($CaCl_2$, 0.1 M) from Sigma-Aldrich.

The additive molecules are dissolved in pure water during stirring or ultrasonication. The pH of the solutions is recorded before and after adding NaOH, HCl or $CaCl_2$. After the sample preparation, the temperature of the measuring solutions is stabilized to 28 °C prior to the injection into the AFM liquid cell.

pH Measurements

All pH measurements are conducted using a Schott laboratory pH meter (CG 842) equipped with a BlueLine pH electrode (Schott Instruments, 18 pH). The pH electrode is calibrated weekly utilizing buffer standard solutions with a pH value of 4 and 7 (HANNA instruments, type Hi6004 and Hi6007).

2.4 Measurement Conditions

With respect to calcite solubility, all *in-situ* AFM measurements are conducted in an undersaturated solution, only consisting of pure water, the solute organic molecules and, depending on the starting conditions, hydrochloric acid, sodium hydroxide or calcium chloride, respectively. An immersed calcite crystal in an undersaturated solution dissolves at all times, independent of the pH, until the dynamic carbonate equilibrium is reached. Calcite dissolution releases calcium (Ca^{2+}) and carbonate ions (CO_3^{2-}) into the surrounding solution, the latter causing the pH to converge to a pH of around 8.3,[41] which corresponds to the pH of the carbonate equilibrium. The small injection volume (approximately $0.2\,\mathrm{ml}$ to $0.3\,\mathrm{ml}$) of the liquid cell disables pH measurements during and after the *in-situ* AFM experiments. Therefore, all pH values stated in this thesis correspond to the initial pH of the solution, which is adjusted and measured prior to the injection into the liquid cell. Furthermore, as the used liquid cell is open to air, the solution evaporates undoubtedly at all times during the *in-situ* AFM experiment. Hence, this evaporation increases the concentration of all components in the solution. Therefore, the indicated molecule and calcium concentrations refer to the initially prepared concentrations.

Part III

Organic Molecules at the Calcite (10.4)-Water Interface

3

Organophosphonate-Induced Calcite (10.4) Surface Restructuring

The following chapter 3 is based on the article "*Structure-Dependent Dissolution and Restructuring of Calcite Surfaces by Organophosphonates*" by M. Nalbach, A. Moschona, K. D. Demadis, S. Klassen, R. Bechstein and A. Kühnle, which has been accepted for publication in *Crystal Growth & Design*.[42] The molecules studied in this project were synthesized by A. Moschona and K. D. Demadis. I performed or supervised the AFM measurements (some AFM measurements were performed by S. Klassen), analyzed the experimental data, prepared the figures and wrote the manuscript (with the exception of the molecular details in the introduction and the organophosphonate synthesis section) with comments by K. D. Demadis and A. Kühnle. Parts of the article are reproduced verbatim, changes have been made to make this chapter consistent with the other sections in this thesis.

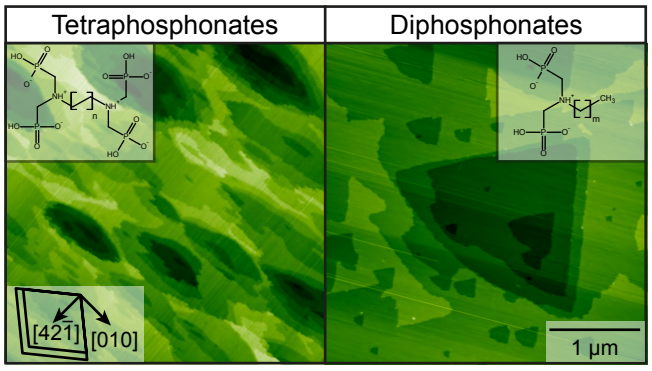

Organophosphonates are well known to strongly interact with the surfaces of various minerals, such as brucite, gypsum and barite. In this work, we study the influence of six systematically varied organophosphonate molecules (tetraphosphonates and diphosphonates) on the dissolution process of the (10.4) surface of calcite. In order to pursue a systematic study, we have selected organophosphonates that exhibit similar structural features, but also systematic architectural differences. The effect of this class of additives on the dissolution process of the calcite (10.4) surface is evaluated using in-situ dynamic atomic force microscopy. For all of the six organophosphonate

derivatives we observe a pronounced restructuring of the (10.4) cleavage plane of calcite, demonstrated by the formation of characteristically shaped etch pits. To elucidate their specific influence on the dissolution process of calcite (10.4), we vary systematically the number of functional end groups (two for the tetraphosphonates and one for the diphosphonates), the spacing between the functional ends through separating methylene groups (two, six and twelve), as well as the pH of the solution (ranging from 2.6 up to 11.7). For each of the two groups of the organophosphonate derivatives, we observe the very same formation of etch pits (olive-shaped for the tetraphosphonate and triangular-shaped for the diphosphonate molecules), respectively. This finding indicates that the number of functional ends decisively determines the resulting calcite (10.4) surface morphology whereas the size of the organophosphonate molecule within one group seems not play any important role. For all of the molecules, the restructuring process of calcite (10.4) is qualitatively independent of the pH of the solution and, therefore, independent of the protonation / deprotonation states of the molecules. Our results reveal a general property of organophosphonate derivatives to induce surface restructuring of the calcite (10.4), which seems to be very robust against variations in both, different molecular structures and different protonation / deprotonation states.

3.1 Introduction - Organophosphonates

Organo*phosphonic* acids are molecules that possess a direct phosphorus-carbon (P-C) bond between the phosphonate tetrahedral moiety and the organic part, in contrast to organo*phosphates*, which possess a phosphorus-oxygen-carbon (P-O-C) linkage.[43] The presence of the robust P-C bond (dissociation energy of 513 kJ/mol[44]) renders these molecules resistant to hydrolysis and thermal decomposition.[45] More specifically, all organophosphonates belong to the aminomethylenephosphonate family, bearing the aminomethylenephosphonate ($-N^+(H)-CH_2-PO_3H^-$) zwitterionic moiety. Due to the high affinity of the phosphonate group towards metal ions and mineral surfaces, organophosphonates have been used extensively in the construction of metal-organic frameworks,[46] as scale growth inhibitors[28] and already have been studied intensively on various surfaces like calcite,[47–49] gypsum,[50] barium sulfate,[51] and brucite.[52]

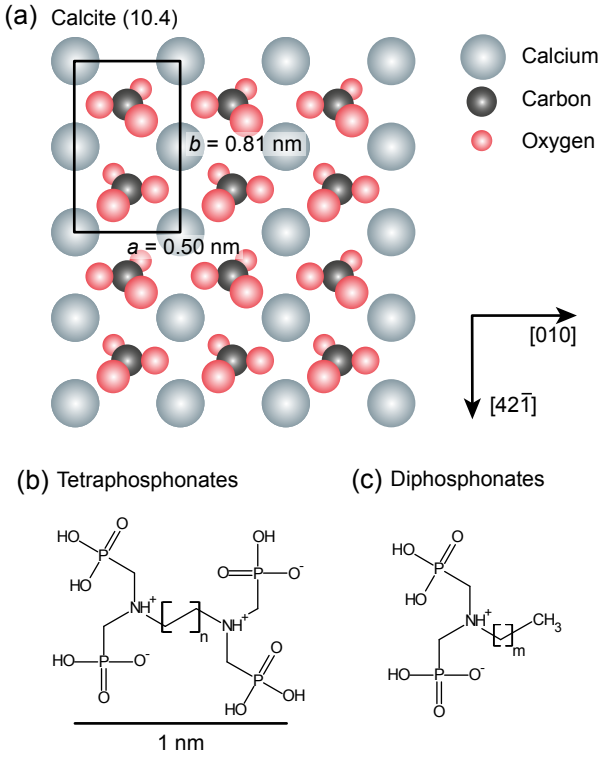

Fig. 3.1: (a) Model of the calcite (10.4) cleavage plane. (b) Schematic structure of the tetraphosphonates. We study molecules with a number of methylene spacing groups of $n = 1, 3, 6$. (c) Schematic structure of the diphosphonates. Here, the number of methylene spacing groups equals $m = 1, 5, 11$. The scale bar in (b) applies to all subfigures.

Organic additives are known to alter the surface morphology of minerals in various ways, *e.g.* affecting dissolution and growth, as well as inducing a restructuring of the surface.[17,18,53–57] For example, ancient polysaccharide[57] adsorbs with a high affinity to calcite step edges, resulting in a modified and characteristically restructured surface morphology during both, calcite dissolution and calcite growth.

Here, we study the influence of three tetraphosphonate and three diphosphonate molecules on the dissolution process of the calcite (10.4) surface, the thermodynamically most stable cleavage plane of calcite (fig. 3.1 a). The schematic structures for each family of organophosphonates are given in fig. 3.1 b and fig. 3.1 c, the detailed molecule names and abbreviations are given in table 3.1.

Tab. 3.1: Names and abbreviations of the organophosphonate molecules. The abbreviation includes the acronym for the name, the number of methylene spacing groups (C_x), as well as a labeling for the number of phosphonic acid end groups. T denotes *tetra* for the four phosphonic acid groups in the tetraphosphonates and D denotes *di* for the two phosphonic acid groups in the diphosphonates.

Additive Name	Additive Abbreviation
Ethylenediamine-*tetrakis*(methylenephosphonic acid)	EDTMP-C_2-T
Hexamethylenediamine-*tetrakis*(methylenephosphonic acid)	HDTMP-C_6-T
Dodecamethylenediamine-*tetrakis*(methylenephosphonic acid)	DDTMP-C_{12}-T
Ethylamine-*bis*(methylenephosphonic acid)	EABMP-C_2-D
n-Hexamethylamine-*bis*(methylenephosphonic acid)	HABMP-C_6-D
n-Dodecamethylamine-*bis*(methylenephosphonic acid)	DABMP-C_{12}-D

For our studies, we focus on two principal structural differences of the additive molecules. On the one hand, within each group of organophosphonate molecules, we study the influence of the spacing between the functional ends through a variation of the number of methylene (-CH_2-) groups. We compare molecules with only two separating methylene groups (EDTMP-C_2-T and EABMP-C_2-D), six (HDTMP-C_6-T and HABMP-C_6-D) and twelve (DDTMP-C_{12}-T and DABMP-C_{12}-D). On the other hand, we compare for each of the three pairs of organophosphonate molecules the difference in the number of functional end groups, which consists of phosphonic acid (-PO_3H_2) groups connected *via* a tertiary amine (R-N(CH_2)$_2$) group. The tetraphosphonate molecules possess two amino-*bis*(methylenephosphonate) functional ends (fig. 3.1b), the diphosphonate molecules only one identical amino-*bis*(methylenephosphonate) functional end (fig. 3.1 c), respectively. Finally, we systematically vary for all molecules the solution pH to elucidate the pH dependence of the surface restructuring process of calcite (10.4) in the presence of organophosphonate molecules. We find that independent of the solution pH, all six organophosphonate molecules significantly restructure the (10.4) surface of calcite by the formation of characteristically shaped etch pits. This observation indicates a general property of molecules

with functional ends consisting of phosphonate groups connected *via* a tertiary amine group to enable surface restructuring of the calcite (10.4) cleavage plane. The number of phosphonate end groups alone seems to exert no influence on the ability of the molecules to restructure the calcite (10.4) surface, however, it seems to determine decisively the resulting surface morphology. For the three tetraphosphonate molecules we observe characteristic olive-shaped etch pits, while for the diphosphonate molecules a triangular etch pit geometry is predominant on the calcite (10.4) cleavage plane. The results of the surface restructuring within each group of organophosphonate molecules are independent of the spacing between the functional ends, revealing that the size of an organophosphonate molecule does not have an influence on the dissolution process of calcite (10.4) and only the presence of at least one functional end plays a decisive role.

Organophosphonate Synthesis

Ethylenediamine (99 %), 1,6-diaminohexane (> 98 %), 1,12-diaminododecane (> 98 %), ethylamine (70 %), *n*-hexylamine (99 %) and *n*-dodecylamine (97 %) are purchased, from Alfa Aesar, formaldehyde (36.5 % aqueous solution) is purchased from Riedel-de Haen, and phosphorus acid (99 %), as well as hydrochloric acid (37 % aqueous solution) are purchased from Sigma-Aldrich. The reactants are all used without further purification. All organophosphonic acid molecules are synthesized *via* the Mannich-type (Irani-Moedritzer) reaction. In principle, this reaction allows the clean transformation of a primary amine to an amino-*bis*(methylenephosphonic acid) moiety. Literature procedures are followed.[58–60] All organophosphonic acids are isolated as high-purity solids in > 50 % yields, except EDTMP-C_2-T which is kept dissolved in water and used as a 25.4 % w/w stock solution.

Further experimental details about solution preparation, instrumentation, measurement condition and information about the *in-situ* AFM setup are given in are given in section 2.2, section 2.3 and section 2.4.

3.2 Results and Discussion - Organophosphonates

We study aqueous organophosphonate solutions with additive concentration ranging from 0.19 μM up to 309 μM. For all additives, we find that a dissolving calcite (10.4) surface restructures under shrinkage of calcite terraces and the formation of characteristically shaped etch pits (fig. 3.2). Compared to a calcite (10.4) surface dissolving in pure water (in the absence of additives), the calcite (10.4) surface appears to be much more rough and uneven in the presence of the three tetraphosphonate molecules (fig. 3.2 a-c). We observe irregular shaped calcite (10.4) terraces and several, but small etch pits. During the experiment, these etch pits grow mainly in size while exposed calcite terraces vanish almost completely.

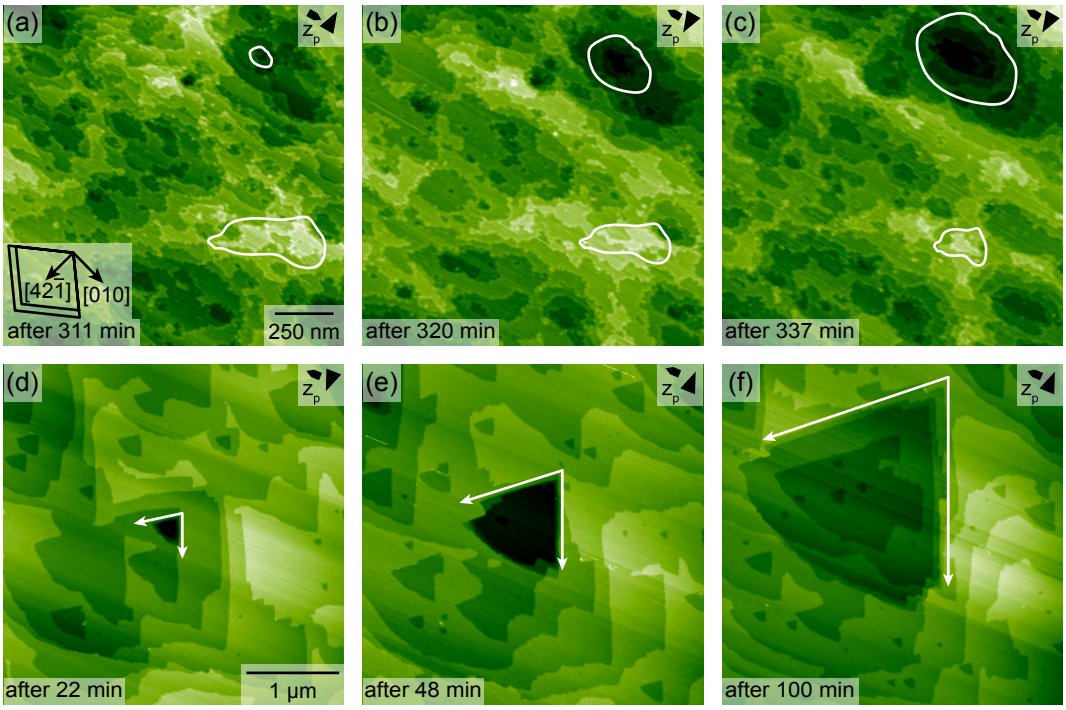

Fig. 3.2: Representative AFM image series of a calcite (10.4) surface in the presence of the organophosphonate molecules demonstrating calcite dissolution and etch pit formation. Images (a-c) are taken in the presence of 0.37 μM EDTMP-C_2-T at a pH of 3.1. A rough and uneven calcite (10.4) surface with predominant etch pits and less distinct terraces is found. Perimeters of a shrinking calcite terrace and a growing etch pit are exemplarily marked by white lines. The scale bar in image (a) applies to all images in the series (a-c). Images (d-f) are taken in the presence of 258 μM EABMP-C_2-D at a pH of 6.7. Here, the area of distinct calcite terraces is larger compared to image series (a-c). The dimension of one dominant growing etch pit is marked by white arrows. The scale bar in image (d) applies to all images in the series (d-f). The images color scale represents a height difference of 3.3 nm (a, e), 4.3 nm (b), 5.0 nm (c), 3.5 nm (d) and 2.8 nm (f).

For all three tetraphosphonate molecules (EDTMP-C_2-T, HDTMP-C_6-T and DDTMP-C_{12}-T), the very same restructured surface morphology of calcite (10.4) is revealed. This indicates a general property for the group of tetraphosphonate molecules to be able to restructure calcite (10.4) during dissolution. Therefrom, the spacing

between the functional ends seems to have no influence on the surface restructuring process as no differences between two, six and twelve separating methylene groups are observed. For the three diphosphonate molecules (EABMP-C_2-D, HABMP-C_6-D and DABMP-C_{12}-D), a very similar situation can be found during calcite dissolution. We also observe a restructured calcite (10.4) surface, however, compared to the tetraphosphonate molecules, now with a larger area of distinct terraces and triangular-shaped etch pits (fig. 3.2 d-f). Here, during the course of the experiment the etch pits also grow in size and depth as the confining step edges retreat. However, the calcite (10.4) substrate appears to be less rough and uneven as compared to when the diphosphonate molecules are present. Variation of the spacing between the functional ends within the group of diphosphonate molecules (*i.e.* the length of the alkyl side-chain) again shows no difference in the surface restructuring of a dissolving calcite (10.4) surface. This finding also points towards a general property for diphosphonate molecules to restructure calcite (10.4) during dissolution.

As all six organophosphonate molecules studied here show the very same influence on calcite (10.4) dissolution, we can conclude that the existence of at least one functional end (two phosphonate groups connected *via* a tertiary amine group) enables calcite (10.4) surface restructuring. Furthermore, as we can see qualitative differences in the surface morphology between the presence of tetra- and diphosphonate molecules, but no differences within each group, we can deduce that the number of functional end has a significant influence whereas the spacing between the functional ends seems not to play an important role.

Etch pit geometries on calcite (10.4). The dissolution process of calcite (10.4) in pure water is characterized by the formation of rhombohedral etch pits (fig. 3.3 a). These etch pits are terminated by the thermodynamically most stable step edges running along the $[4\bar{4}\bar{1}]$ and $[48\bar{1}]$ directions (fig. 3.3 b). All four step edges of an etch pit are neutral because of an alternating arrangement of calcium ions and carbonate groups. Tilting of the carbonate groups in the calcite (10.4) surface structure results in two different edges pits sides, namely acute and obtuse. The two obtuse step edge sides are known to exhibit a more rounded shape, resulting in the asymmetric etch pit appearance in fig. 3.3 a.[61–63]

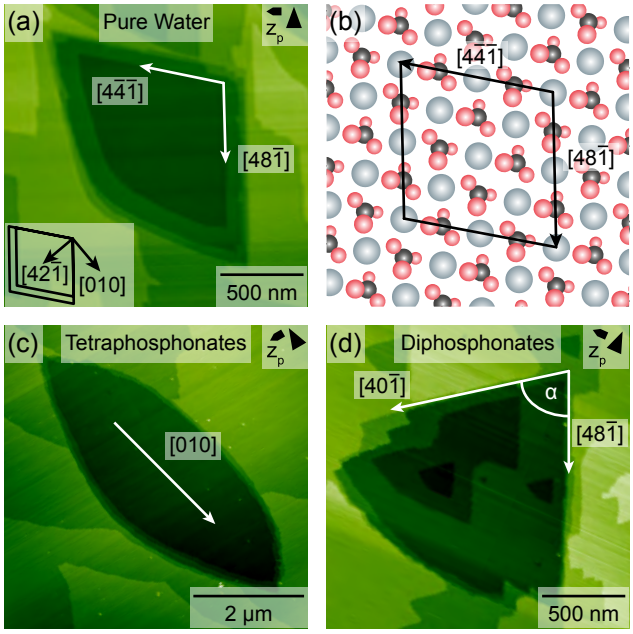

Fig. 3.3: Etch pit geometries observed on the calcite (10.4) surface in the absence and presence of the organophosphonate molecules. (a) Amplitude modulation atomic force microscopy (AM-AFM) image of the calcite (10.4) surface in pure water showing characteristic rhombohedral etch pits. (b) Model of the calcite (10.4) surface illustrating the etch pit termination by the thermodynamically most stable step edges running along the [4$\bar{4}\bar{1}$] and [48$\bar{1}$] directions. (c) Characteristic olive-shaped etch pit in the presence of the three tetraphosphonate molecules EDTMP-C_2-T, HDTMP-C_6-T and DDTMP-C_{12}-T. The long diagonal of the etch pit is running along the [010] direction, the short diagonal along the [42$\bar{1}$] direction. The obtuse step edge sides are rounded similarly to the one in etch pit in (a). (d) A characteristic triangular etch pit geometry is found when the diphosphonate molecules EABMP-C_2-D, HABMP-C_6-D and DABMP-C_{12}-D are present. The etch pits observed here only show the [48$\bar{1}$] direction as one of the usually seen acute step edges directions. However, the obtuse step edge side is slightly rounded too. The angle α to the other acute edge is measured to be 75°. The images color scale represents a height difference of 3.8 nm (a), 3.5 nm (c) and 3.0 nm (d).

In the presence of the three tetraphosphonate molecules EDTMP-C_2-T, HDTMP-C_6-T and DDTMP-C_{12}-T etch pits with an olive shape are observed all over the calcite (10.4) surface (fig. 3.3 c). The geometry of the olive shaped etch pits is much related to etch pits in pure water. The long diagonal is also running along the [010] direction, likewise the short diagonal is running along the [42$\bar{1}$] direction. The two obtuse step edge sides are rounded in a similar same way as it is observed in the asymmetric etch pit appearance in pure water. Due to the symmetry of the olive shaped etch pits also the obtuse step edge sides are now rounded. For the three diphosphonate molecules EABMP-C_2-D, HABMP-C_6-D and DABMP-C_{12}-D, we find etch pits with a predominant triangular etch pit geometry (fig. 3.3 d). These etch pits only show one of the commonly seen thermodynamically most stable acute step edges directions, the [48$\bar{1}$] direction. Nevertheless, the obtuse step edge side is slightly rounded too and therefore comparable to the etch pit curvature for pure water and for the presence of the Tetraphosphonates. The pronounced angle in the acute step edge corner is measured to be 75°.

pH-independent dissolution process. Organophosphonic acids produce a plethora of chemical species in aqueous solutions, depending on the pH.[64]

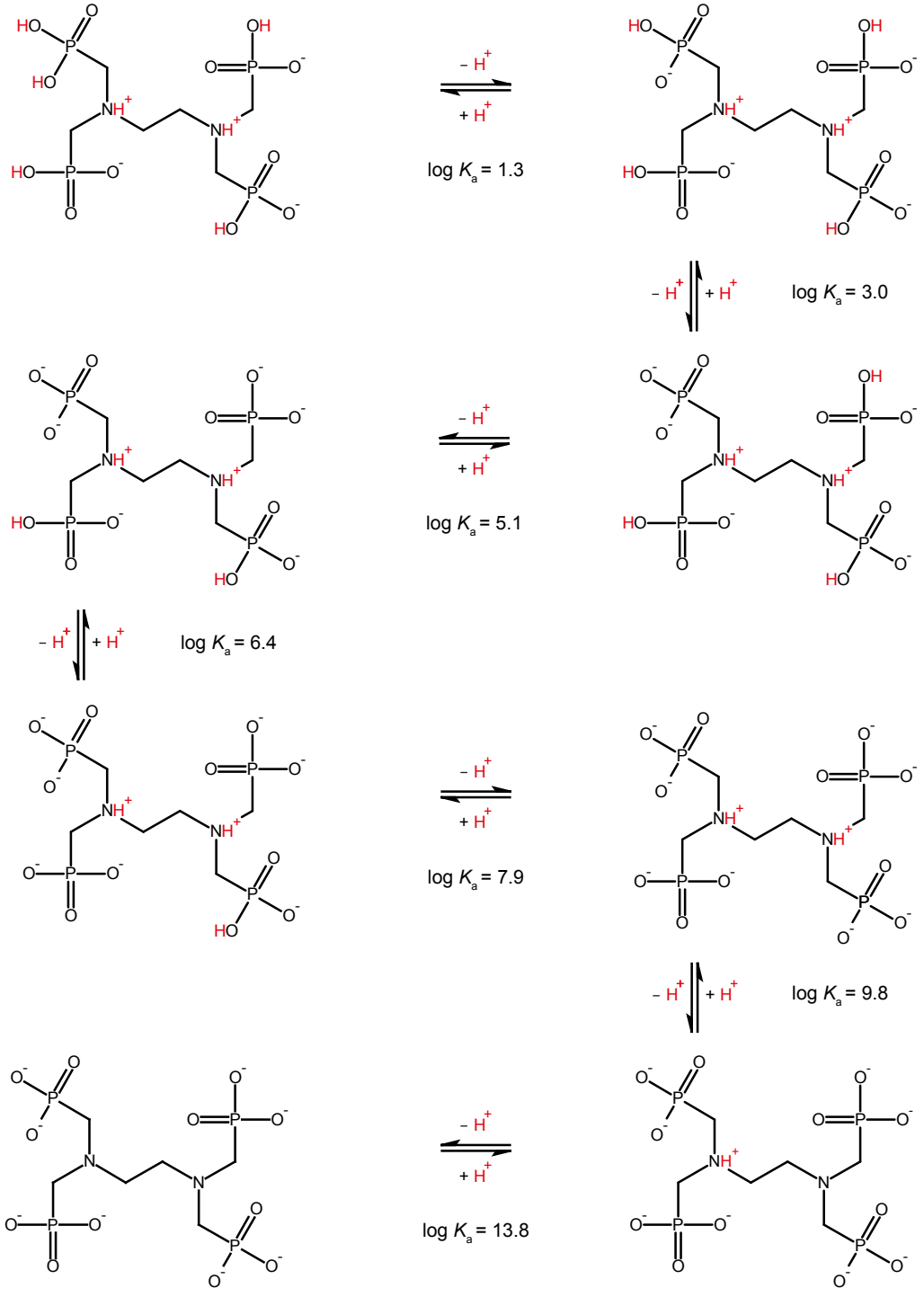

Fig. 3.4: Protonation / deprotonation sequence for EDTMP-C_2-T, showing eight experimentally detected species. The stepwise deprotonation behavior, starting from the three-fold deprotonated ($H_7EDTMP{-}C_2{-}T^{-}$) species to the fully deprotonated ($EDTMP{-}C_2{-}T^{8-}$) species, is displayed from left to right and top to bottom. Values for the logarithmic acid dissociation constant (log K_a) for each protonation / deprotonation step are provided.[65] Relevant protons for each protonation / deprotonation step are highlighted in red.

Popov *et al.*[65] have summarized a large portion of the available literature on critical stability constants for a number of phosphonic acids. Based on the reported data, we draw the scheme in fig. 3.4, illustrating the protonation / deprotonation of EDTMP-C_2-T, exemplarily for the tree tetraphosphonates, as well as the scheme in fig. 3.5, showing the protonation / deprotonation of EABMP-C_2-D, exemplarily for the tree diphosphonates. Such data and related speciation diagrams[66] can be very useful in interpreting experimental results, particularly for mineral scale inhibition[22] and decalcification of biominerals,[23,24] but should be used with caution due to the different experimental conditions employed in measuring the pK_a's of the phosphonic acids.

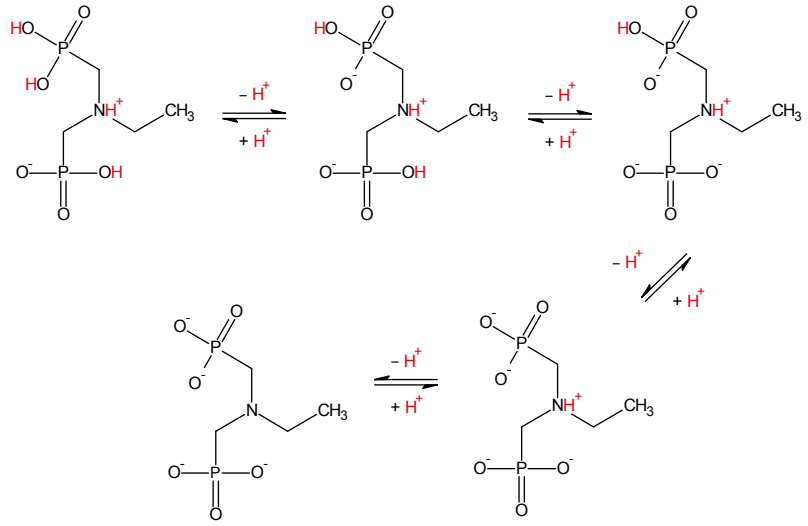

Fig. 3.5: Protonation / deprotonation for EABMP-C_2-D, showing five experimentally detected species. The stepwise deprotonation behavior, starting from the neutral (H_4EABMP$-C_2-$D) species to the fully deprotonated (EABMP$-C_2-D^{4-}$) species. Relevant protons for each protonation / deprotonation step are highlighted in red.

To study the pH-dependence of calcite (10.4) surface restructuring in the presence of the organophosphonate molecules, we perform *in-situ* AFM experiments with solution pH values ranging from 2.6 up to 11.7. The results for the measurements with varying solution pH are illustrated in fig. 3.6. Here, we show representative results for the tetraphosphonate EDTMP-C_2-T at solution pH values of 4.1, 8.2 and 11.7 (fig. 3.6 a-c), and for the diphosphonate EABMP-C_2-D at solution pH values of 3.5, 5.7 and 9.5 in fig. 3.6 d-f.

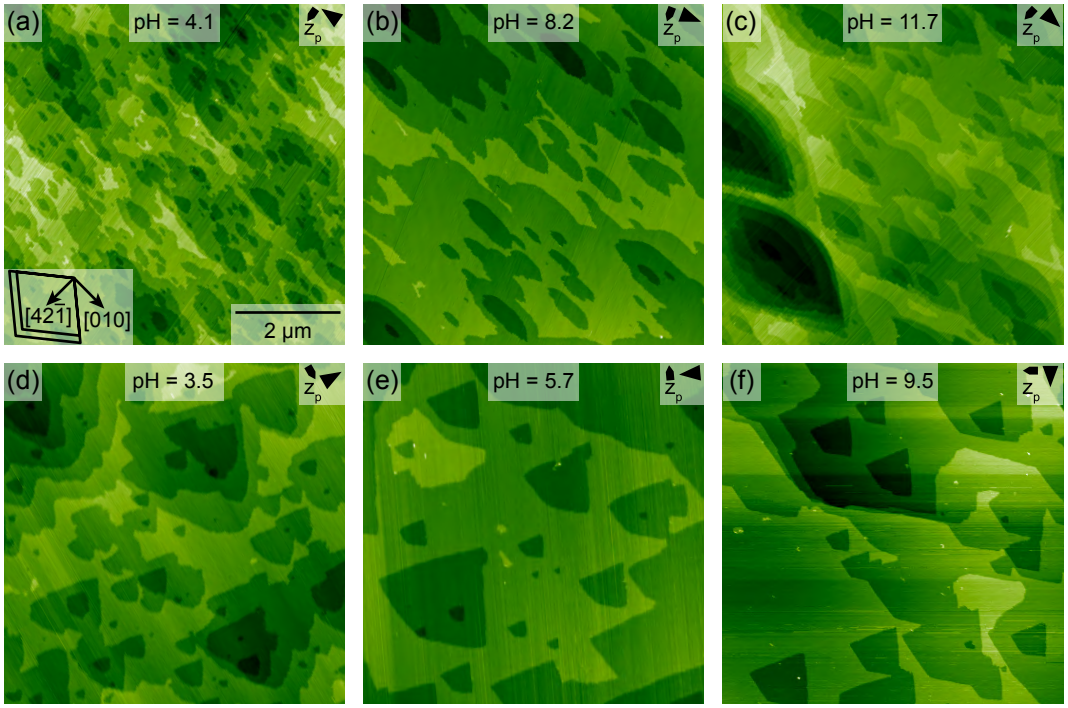

Fig. 3.6: Representative AFM images demonstrating the pH independence of the surface restructuring of calcite (10.4) in the presence of the organophosphonate molecules. The images (a), (b) and (c) are taken in the presence of 0.19 μM EDTMP-C_2-T at solution pH values of 4.1, 8.2 and 11.7, respectively. The images (d) and (f) are taken in the presence of 309 μM EABMP-C_2-D, image (e) in the presence of 258 μM EABMP-C_2-D at solution pH values of 3.5, 5.7 and 9.5, respectively. The scale bar in (a) applies to all images. The images color scale represents a height difference of 3.0 nm (a), 2.5 nm (b, d), 5.0 nm (c), 3.3 nm (e) and 2.1 nm (f).

We find no significant differences in the surface restructuring, depending on the pH value and regardless of the specific molecule studied. We observe for both families of organophosphonate molecules the very same etch pit shape (olive for the tetraphosphonate and triangular for the diphosphonate molecules) as the result of the dissolution process, independent of solution pH. This observation indicates that the surface restructuring process seems to be insensitive against variations in both factors, *i.e.* structural differences due to the alkyl spacing between the functional ends and different protonation / deprotonation states caused by the solution pH. The pH independence of calcite (10.4) surface restructuring has been recently also observed in *in-situ* AFM studies in the presence of organic dye molecules[19] and, hence, might indicate a more general surface restructuring mechanism in the presence of chemical additives.

3.3 Summary and Conclusion - Organophosphonates

Herein, we systematically study the impact of six different organophosphonate molecules, three tetraphosphonates (EDTMP-C_2-T, HDTMP-C_6-T and DDTMP-C_{12}-T) and three diphosphonates (EABMP-C_2-D, HABMP-C_6-D and DABMP-C_{12}-D) on the dissolution process of calcite (10.4) using *in-situ* dynamic AFM. For each molecule, a pronounced surface restructuring is observed, resulting in the formation of characteristically shaped etch pits for each group of organophosphonate molecules. From that, we can conclude that the existence of at least one functional end (two phosphonate groups connected *via* methylene linkers to a tertiary amine group) is sufficient to enable calcite (10.4) surface restructuring. This observation points towards a general property of organophosphonate molecules to alter and restructure the (10.4) surface of calcite during dissolution.

Furthermore, the difference in the number of functional phosphonate end groups (four for the tetraphosphonates and two for the diphosphonates) decisively determines the resulting surface morphology. We observe olive-shaped etch pits for the tetraphosphonate and triangular-shaped ones for the diphosphonate molecules. In contrast to the number of functional end groups, changing the spacing between the functional ends through a variation of the number of methylene groups (two, six and twelve) has no influence on the dissolution process of calcite (10.4). For all three tetraphosphonate, as well as for the three diphosphonate derivatives, we observe the very same etch pit geometry, respectively. Finally, the dissolution process of calcite (10.4) in the presence of each of all six molecules is independent of solution pH and, therefore, not affected by the protonation / deprotonation state of the molecules. The surface restructuring process of calcite (10.4) during dissolution in the presence of the organophosphonate molecules studied here appears to be very robust against variations in both, additive molecular structure and solution pH.

Although precise information on the interaction of the phosphonate group with the calcite surface at the molecular level cannot be drawn from AFM studies, it is well established that the doubly-deprotonated R-$PO_3{}^{2-}$ group interacts much more strongly with the calcite surface than the singly-deprotonated R-PO_3H^- group.[49] This is consistent with the pH-independent restructuring process observed for all organophosphonate additives. Furthermore, the second additive side moiety (a second amino-*bis*(methylenephosphonate) group for the tetraphosphonates and an alkyl group for the diphosphonates) does not seem to directly interact with the surface of calcite (10.4).

However, it may indirectly influence the interaction of the entire molecule by creating a hydrophilic (for tetraphosphonates) or a hydrophobic (for diphosphonates) microenvironment on the calcite surface. The structural differences in the non-interacting side-groups between tetraphosphonates and diphosphonates are consistent with the morphology of the etch pits observed. The important observation that within the same family the side chain-length does not seem to influence the restructuring process confirms that one amino-*bis*(methylenephosphonate) moiety alone is necessary for the process to occur.

4 Molecular Self-Assembly Versus Surface Restructuring

The following chapter 4 is based on the article "*Molecular Self-Assembly Versus Surface Restructuring During Calcite Dissolution*" by M. Nalbach, S. Klassen, R. Bechstein and A. Kühnle, which has been published in *Langmuir*.[19]
I performed or supervised the AFM measurements for this project (some of the AFM measurements were performed by S. Klassen), analyzed the experimental data, prepared the figures and wrote the manuscript with comments by R. Bechstein and A. Kühnle. For this thesis, parts of the article are reproduced verbatim. Changes have been made to make this chapter consistent with the other sections in this thesis. For this chapter, I included large-scale AFM data about the surface restructuring in the presence of Eriochrome Black T.

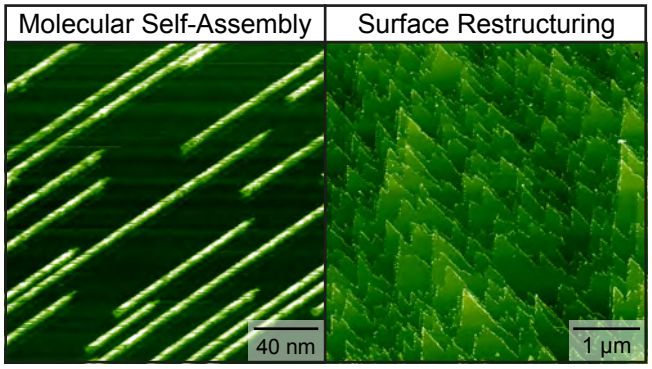

Organic additives are known to alter the mineral-water interface in various ways. On the one hand, organic molecules can self-assemble into ordered structures wetting the surface. On the other hand, their presence can affect the interfacial morphology, referred to as surface restructuring. Here, we investigate the impact of a class of calcium-complexing azo dyes on the dissolution of calcite (10.4) using in-situ high-resolution dynamic atomic force microscopy, with a focus on the two constitutional isomers Eriochrome Black T and Eriochrome Black A. A very pronounced surface restructuring is observed in the presence of the dye solution, irrespective of the specific dye used and independent of the pH. This surface restructuring is obtained by the stabilization of both the non-polar acute and the polar [010] step edges, resulting in a greatly altered, characteristic interface morphology. In sharp contrast to the prevalence of the surface restructuring, an ordered molecular structure on the crystal terraces is observed

only under very specific conditions. This formation of an ordered stripe-like molecular structure is obtained from Eriochrome Black A only and limited to a very narrow pH window at a pH value of around 3.6. Our results indicate that such molecular self-assembly requires a rather precise adjustment of the molecular properties including control of the conformation and deprotonation state. This is in sharp contrast to the additive-induced surface restructuring, which appears to be far more robust against both pH changes and variations in the molecular conformation.

4.1 Introduction - Eriochrome Azo Dyes

The interaction of organic molecules with mineral surfaces within their natural environment is decisive for a wide range of processes within fields such as: geochemistry[2,5,16] and biomineralization,[13,14,67,68] as well as within industry.[12,69] Especially calcite, the most stable polymorph of calcium carbonate ($CaCO_3$), has attracted great attention due to its abundance in the earth crust and its pivotal role in the above mentioned areas.[15,17,41,53,70–77] Consequently, additive-induced changes of the calcite-water interface have been studied in an attempt to rationalize processes during biomineralization and biomimetic crystallization.[17,18,47,78–81]

To this end, microscopy techniques have been proven to provide high-resolution insights into additive-controlled calcite dissolution, growth and surface restructuring, as these techniques offer the ability to directly visualize the mineral-water interface,[26] as well as the hydration structure above the surface.[77,82,83] This real-space insight is often combined with complementary experimental information, *e.g.*, spectroscopic or X-ray reflectivity measurements, and theoretical investigations, such as: molecular dynamics (MD) simulations.[84] However, despite considerable effort in this field, elucidating the detailed mode of action of organic additives in calcite nucleation, dissolution and growth remains a challenge in most cases.

In this context, an interesting question addresses the competition between additive-induced surface restructuring[17,18,57] and the formation of a self-assembled molecular structure[1] on the mineral surface.[15] While both processes can, in principle, occur at the same time, the vast majority of studies reported so far have revealed distinct surface restructuring, often resulting in the formation of otherwise thermodynamically unstable step edges, *e.g.*, the polar [010] step edge.[17] In contrast, reports on the formation of ordered, self-assembled molecular structures on the mineral surface are comparatively rare. On the one hand, this might be in part due to the fact that massive surface restructuring can be readily detected, while

[1] We note that the term “self-assembly“ is usually used for equilibrium structures while “self-organization“ is used for kinetically trapped structures. As it can be far from trivial to evaluate whether a given structure is the equilibrium structure, we decided to use the term “self-assembly“ regardless of whether it is in equilibrium or not.

self-assembled structure might be more challenging to be observed as they require high-resolution techniques capable of monitoring a weakly bound molecular monolayer at the mineral-water interface. On the other hand, this observation could also be indicative of a more general principle at play during interaction of organic molecules with the mineral-water interface.

In this work, we investigate molecules from the class of Eriochrome azo dyes (fig. 4.1 a and b), which are known to interact with magnesium and calcium ions, as well as other di- and trivalent metal ions as they are used for chelatometric titration.[27,85–87] Stability constants of the magnesium and calcium complexes and their binding motives have been studied intensively using extinction experiments.[85]

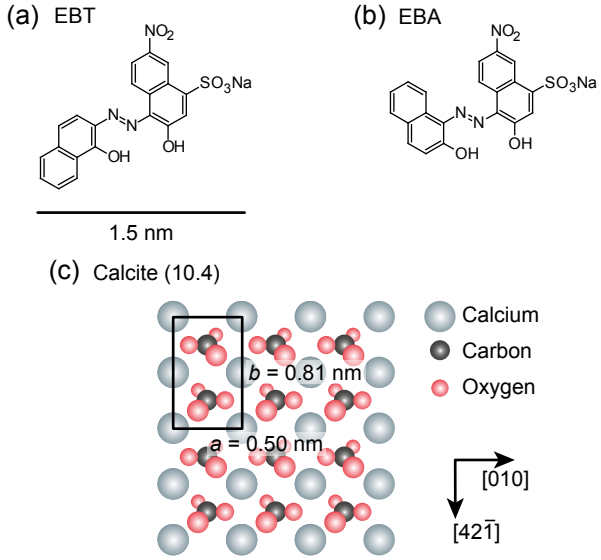

Fig. 4.1: Model of the two constitutional isomers of the Eriochrome azo dyes, namely, (a) Eriochrome Black T (EBT) and (b) Eriochrome Black A (EBA), which are used for main body of experiments this study. (c) Model of the calcite (10.4) surface. The scale bar in (a) applies to all subfigures.

Due to their complexation ability, the Eriochrome azo dyes, especially Eriochrome Black T, are therefore used to determine water hardness. We demonstrate that the ability to restructure the (10.4) surface of calcite (fig. 4.1 c) into a characteristic morphology appears to be a general property of these molecules, irrespective of the specific molecular structure and solution the pH value. In contrast, the formation of an ordered self-assembled structure is more delicate to achieve. We observe molecular self-assembled structures only for one out of the five Eriochrome dyes tested and only in a narrow pH window.

Our work indicates that molecular self-assembly requires a precise tuning of the molecule's properties including control of conformation and deprotonation state, while surface restructuring appears to be more robust against variations in the molecular properties.

Materials and Methods

Eriochrome Black T (EBT, ACS reagent, indicator grade), Eriochrome Blue Black B (EBBB, indicator (for complexometry)) and Eriochrome Blue Black R (EBBR, indicator (for complexometry (Al, Fe, Zr))) are purchased from Sigma Aldrich. Eriochrome Black A (EBA) and Eriochrome Red B (ERB) are purchased from TCI Deutschland GmbH. All dye molecules are used in the experiments without further purification.

Further experimental details about solution preparation, instrumentation, measurement condition and information about the *in-situ* AFM setup are given in section 2.2, section 2.3 and section 2.4.

4.2 Results and Discussion - Eriochrome Azo Dyes

***In-situ* solution exchange**. To assess the impact of the class of Eriochrome Black molecules on the calcite (10.4)-water interface, we perform *in-situ* solution exchange experiments as shown in fig. 4.2. Here, the etch pits characteristic for calcite (10.4) are revealed in the absence of the additive molecules (fig. 4.2 a).

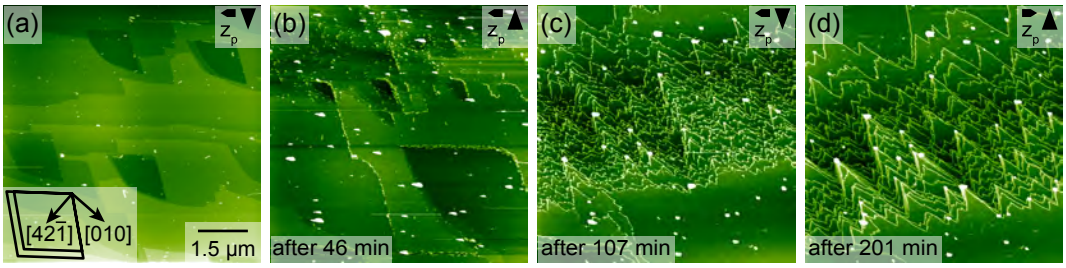

Fig. 4.2: *In-situ* solution exchange experiment demonstrating the additive-induced changes in the calcite surface morphology upon adding EBT to the solution. Image (a) is taken before exchanging the pure water by a 0.14 mM solution of EBT with an initial pH value of 3.6. Images (b), (c), and (d) are taken 46, 107, and 201 min after the addition of EBT. After molecule addition, large bright features appear on the surface as can be seen in image (b). These features remain on the surface after the restructuring and appear to constitute the terminating sites at the tip of the triangular-shaped terraces. The scale bar in image (a) applies to all images in this series.

These etch pits are characterized by a rhombohedral shape with the two acute step edges being straight, while the obtuse step edges are known to develop into curved steps.[61–63,70] Upon exchange of the pure water by a 0.14 mM EBT solution, the surface is observed to restructure. Already 46 min after injection of the molecules, the acute step edges appear to be decorated by molecules, while the obtuse step edges seem less covered (fig. 4.2 b). In the course of the experiment, the obtuse step edges vanish and steps along the [010] direction appear instead (fig. 4.2 c).

These newly formed steps in [010] direction are found to be decorated with molecules. Overall, a characteristic triangular-shaped terrace termination emerges from this restructuring (fig. 4.2 d).

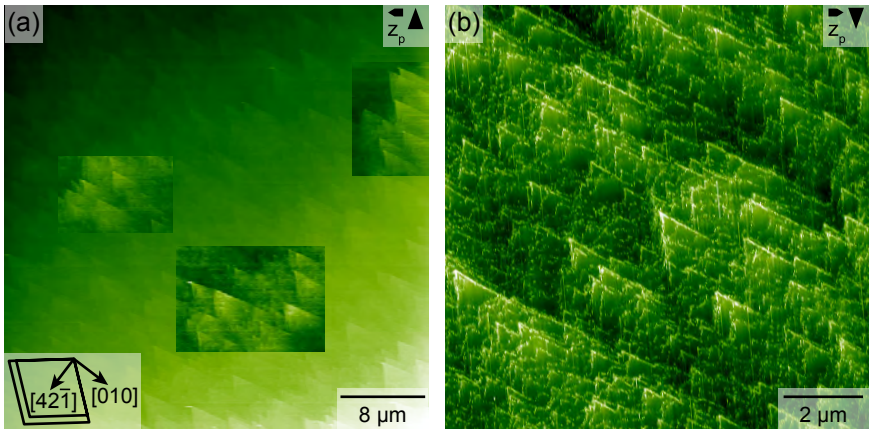

Fig. 4.3: Large-scale AFM images of a restructured calcite (10.4) surface. (a) 40 μm AFM image of calcite (10.4) in the presence of 0.15 mM solution of EBT at an initial solution pH of 3.6. The image color scale is adjusted to color code the height difference between the highest (lower right corner) and the lowest (upper left corner) position on the surface. The three cut-out images with a different image color scale show the characteristic triangular-shaped terrace termination. (b) Zoom into the terraced structure in image (a), indicating the step edges decoration with molecular structures.

This triangular-shaped terrace pattern can be found on large areas of the calcite (10.4) surface (fig. 4.3). In fig. 4.3 a, the terrace termination is shown on a 40 μm AFM image of calcite (10.4). Here, the color scale demonstrates the significant height difference between the highest (lower right corner) and the lowest (upper left corner) position on the surface, as well as the multiplicity of small terraces in between. The zoom into this terraced structure indicates clearly step edges running along the [010] direction and their decoration with molecular structures.

Step edge models. A model for the observed step edges in the absence and presence of EBT is given in fig. 4.4. The characteristic edge pits in the absence of molecules are terminated by two steps running in the [4$\bar{4}\bar{1}$] and [48$\bar{1}$] directions (fig. 4.4 a). All four step edges have in common that they are neutral with an alternating arrangement of calcium ions and carbonate groups (fig. 4.4 b). However, the edges differ due to the tilt in the carbonate groups, resulting in acute and obtuse edges, as indicated by the unit cell symbol in the lower left corner of fig. 4.4 a. The edge pit termination at the two obtuse sides are known to develop into a rounded shape, resulting in an asymmetric etch pit appearance.[61–63,70] An image showing the characteristic triangular-shaped terrace terminations in the presence of EBT is given in fig. 4.4 c with the corresponding surface model in fig. 4.4 d. While the acute step edge running along the [48$\bar{1}$] substrate direction is still present in this image, all other edges of the edge pit have vanished. Instead, new edges are obtained that run along the [010] direction. Steps in [010] direction are characterized by the

fact that they are formed either by calcium ions or by carbonate groups exclusively. Thus, these step edges are polar. Both, the acute, non-polar steps along the [48$\bar{1}$] direction and the polar steps along the [010] direction are observed to be decorated by molecules.

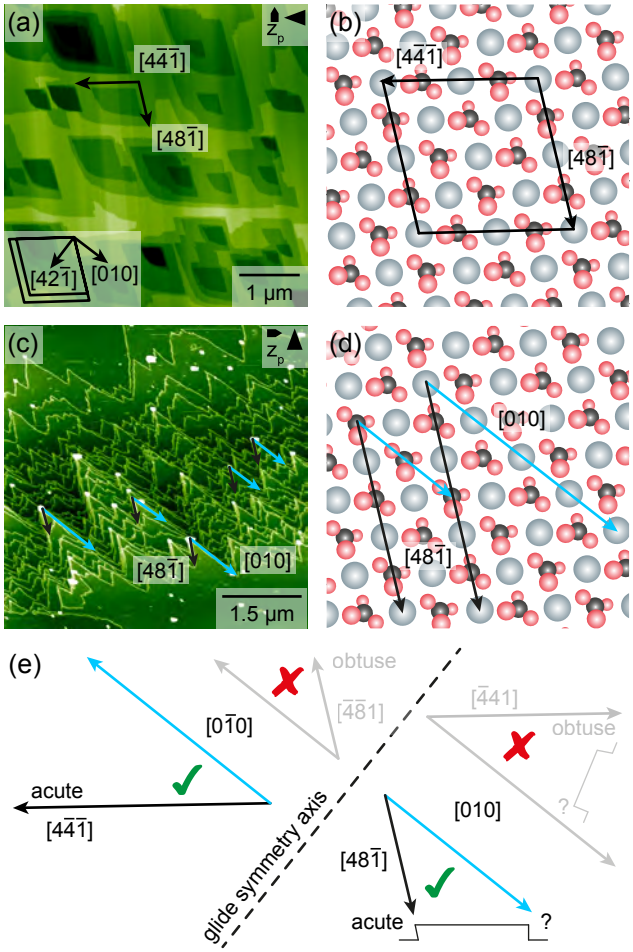

Fig. 4.4: Model for the observed step edges in the absence and presence of EBT. (a) Amplitude modulation AM-AFM image of the bare calcite (10.4) surface, exhibiting the characteristic rhombohedral etch pits. The obtuse step edges are known to exhibit a curved shape.[61–63,70] (b) Model of the calcite (10.4) surface showing the thermodynamically most stable step edges that terminate the etch pits, running along the [4$\bar{4}\bar{1}$] and [48$\bar{1}$] directions. (c) Surface morphology in the presence of 0.14 mM EBT. Triangular-shaped terrace terminations are formed. (d) Model of the surface indicating the two predominant directions marked with black and blue arrows in (c). The step edge marked in black is the originally existing acute step edge in the [48$\bar{1}$] direction. The direction marked in blue is the [010] direction. Steps in this direction are polar because they are terminated by either calcium or carbonate groups exclusively. (e) Model illustrating the different terrace terminations and the glide reflection symmetry of the surface.

Due to the glide reflection symmetry of the surface with the glide reflection axis along the [42$\bar{1}$] direction, an equivalent situation is obtained when step edges along the acute [4$\bar{4}\bar{1}$] and the [010] direction are formed, resulting in the very same triangular-shaped termination of the terraces (fig. 4.3 e). This situation is, indeed, equally observed experimentally. Thus, the presence of the EBT molecules appears to stabilize both the acute non-polar edges, as well as the polar edges along [010]. Interestingly, the obtuse edges are not stabilized by the presence of the EBT molecules and, thus, vanish in the course of the experiment in favor for the polar edges along the [010] direction.

Step edge analysis. To obtain further insights into the step edge decoration, we performed high-resolution images directly at a step. As shown in fig. 4.5 a, the step edge decoration is not limited to a single molecular row, but is imaged as a broad stripe with an apparent width of several tens of nanometers and an apparent height of 1-2 nm, as can be deduced from the line profile given in fig. 4.5 b. No internal order can be resolved within the molecular stripe.

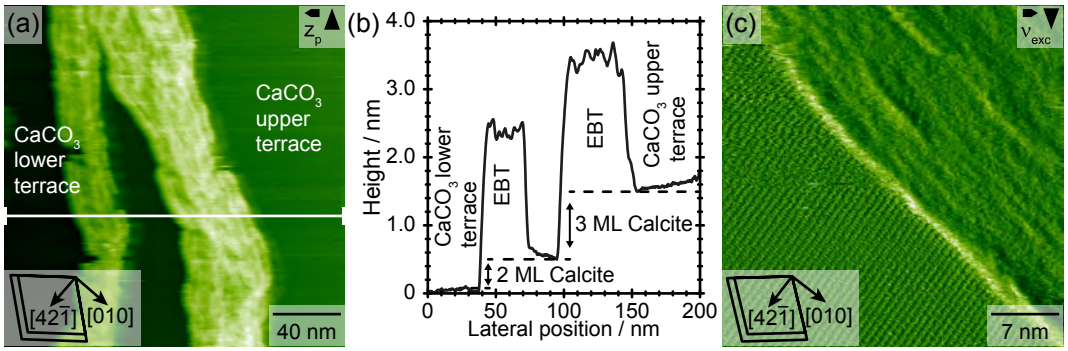

Fig. 4.5: Step edge termination in the presence of EBT. (a) Zoom onto a step edge highlighting the molecule-covered step edges. (b) Line profile taken at the indicated position in (a), revealing an apparent height of the molecular structure of 1-2 nm. (c) Zoom onto the boundary of the molecular structure and the bare calcite, revealing atomic resolution on the calcite (10.4) surface (lower left part).

A further zoom onto the molecular stripe and the calcite substrate as shown in fig. 4.5 c reveals atomic resolution of the underlying calcite lattice. This high resolution is indicative of a sharp tip termination. Despite the good tip quality, no further structure can be resolved in the molecular stripe, suggesting a poorly ordered molecular stripe or rapidly moving end groups rather than a rigid and ordered molecular structure at the edges.

Variation of the solution pH. Next, we investigate the pH dependence of the observed additive-induced surface restructuring. Changing the pH of the solution changes the deprotonation state of EBT. In fig. 4.6 a, the species distribution is given as a function of the pH value of the solution. While one-fold deprotonated molecules are the dominant species at a pH around 3-4, the dominant species at a pH value around 9 is two-fold deprotonated. At a pH of 6.3, the one-fold and two-fold deprotonated species are equally present. Moreover, we note that EBT can undergo an azo-hydrazo tautomerization[88] (fig. 4.6 b), resulting in three (four, one) different species for the one-fold (two-fold, three-fold) deprotonated molecule, respectively.

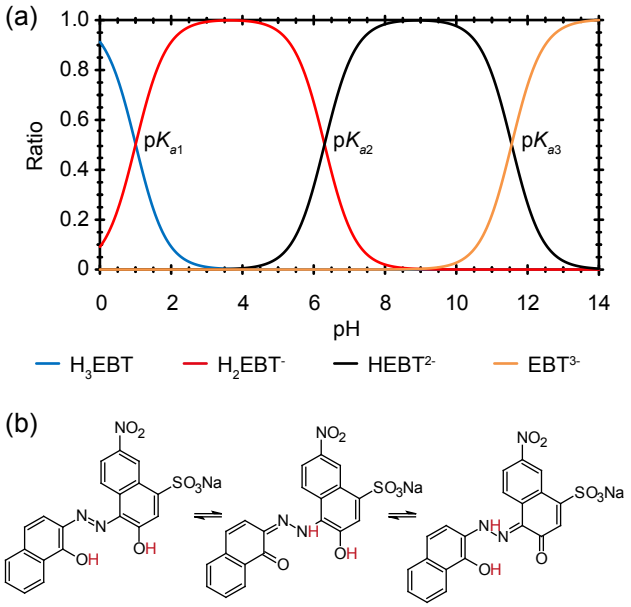

Fig. 4.6: (a) Species distribution of EBT as a function of the pH value. (b) Azo-hydrazo tautomerization of a one-fold deprotonated EBT molecule. Relevant protons for each tautomerization step are highlighted in red.

Species distribution calculation. EBT and EBA possessing one sulfonate ($-SO_3^-$) and two hydroxyl ($-$OH) groups are both triprotic acids. For each protonation / deprotonation step, the acid dissociation constant (K_{ai}) is defined by the quotient of the respective equilibrium concentrations.

$$K_{ai} = \frac{c(\mathrm{H_3O^+}) \cdot c(H_{n-1}A^{i-})}{c(H_{n-i+1}A^{(i-1)-})} \tag{4.1}$$

For EBT and EBA the acid dissociation constants (K_{ai}) for the second and third protonation / deprotonation step are given in table 4.1.[85]

Tab. 4.1: Acid dissociation constants for the second and third protonation / deprotonation step of EBT and EBA.[85]

Molecule	-log K_{a2} = pK_{a2}	-log K_{a3} = pK_{a3}
EBT	6.35	11.55
EBA	6.20	13.00

Calculation of the EBT and EBA species distribution is performed using the relevant protonation / deprotonation equilibrium equations[89] for an *n*-protic acid ($H_{n-i+1}A^{(i-1)-}$).

$$H_{n-i+1}A^{(i-1)-}(aq) + \mathrm{H_2O} \rightleftharpoons H_{n-i}A^{i-}(aq) + \mathrm{H_3O^+}(aq) \tag{4.2}$$

The total concentration (C) for EBT and EBA is the sum over all protonated / deprotonated species being present in the solution at every pH.

$$C = \sum_{i=0}^{n} c\left(H_{n-i}A^{i-}(aq)\right) \tag{4.3}$$

Numerical analysis of the resulting system of linear equations enables the precise determination of the equilibrium concentration of all protonated / deprotonated species at a given pH.

$$c\left(H_{n-i+1}A^{(i-1)-}\right) = \frac{c^{n-1}(\mathrm{H_3O^+}) \cdot C(H_nA) \cdot \prod_{j=1}^{i} K_{Sj}}{\sum_{r=0}^{n}\left[c^{n-r}(\mathrm{H_3O^+}) \cdot \prod_{j=1}^{r} K_{Sj}\right]} \tag{4.4}$$

The species distribution of EBT is illustrated in fig. 4.5 a, the species distribution of EBA is illustrated in fig. 4.7.

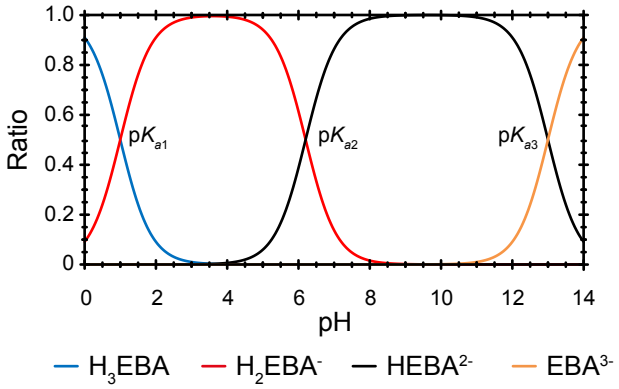

Fig. 4.7: Species distribution of EBA as a function of the pH value.

Azo-hydrazo tautomerization. We note that the Eriochrome azo dyes can undergo an azo-hydrazo tautomerization,[88] resulting in three, four and one different species for the one-fold, two-fold and three-fold deprotonated molecule, respectively. The azo-hydrazo tautomerization of an one-fold deprotonated EBT molecule is shown in fig. 4.5 a, the azo-hydrazo tautomerization of a two-fold deprotonated EBT molecule is shown in fig. 4.8.

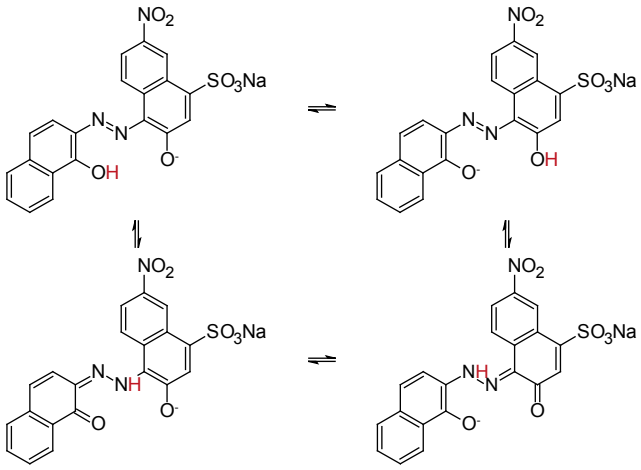

Fig. 4.8: Azo-hydrazo tautomerization of a two-fold deprotonated EBT molecule. Relevant protons for each tautomerization step are highlighted in red.

pH-independent surface restructuring. As demonstrated in fig. 4.9, the characteristic triangular terrace termination is found for all pH values tested here, ranging from a pH of 3.6 to 9.1. This fact indicates that the surface restructuring ability appears to be independent of the specific deprotonation state of the molecule.

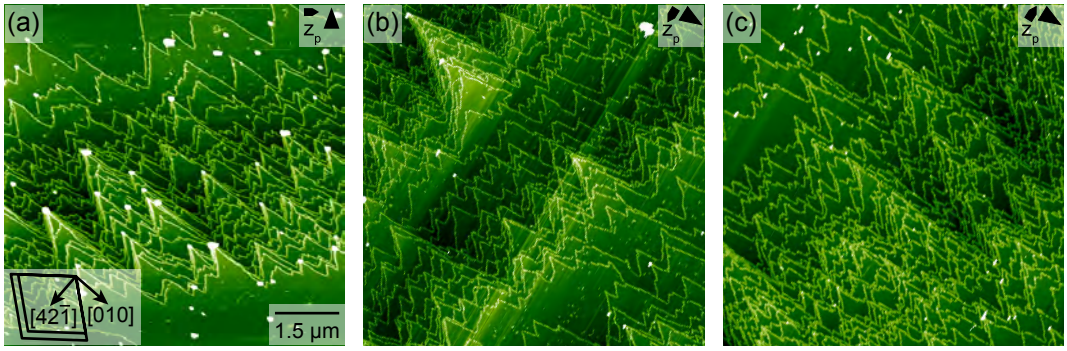

Fig. 4.9: Demonstration of the pH independence of surface restructuring by EBT. Calcite (10.4) surface in the presence of 0.11-0.14 mM EBT at an initial solution pH of (a) 3.6, (b) 6.3 and (c) 9.1. The scale bar in image (a) applies to all images in this series.

Moreover, while we show the surface restructuring induced by EBT as a representative example, the very same surface morphology is revealed for all Eriochrome Black dyes studied here. Thus, the ability to restructure the surface into a characteristic morphology with triangular-shaped terrace terminations appears as a general property of the entire class of the Eriochrome Black dye family.

The restructuring is insensitive against changes in the molecular conformer or even molecular structure. Moreover, the specific deprotonation state of the molecule seems not to affect the restructuration ability.

Stripe formation on calcite (10.4) terraces. In sharp contrast to the prevalence of substrate restructuring, ordered self-assembled structures are observed only for one out of the five tested Eriochrome Black azo dyes, namely, EBA. As shown in fig. 4.10 a, the presence of EBA results in the characteristic triangular terrace termination as reported above. Interestingly, when zooming into a terrace, molecular rows are observed that run along the [42$\bar{1}$] substrate direction (fig. 4.10 b). A line profile taken at the position indicated in fig. 4.10 c reveals an apparent height of about 1.5 nm (fig. 4.10 d). The width of the stripes is uniform, indicating a highly ordered molecular structure.

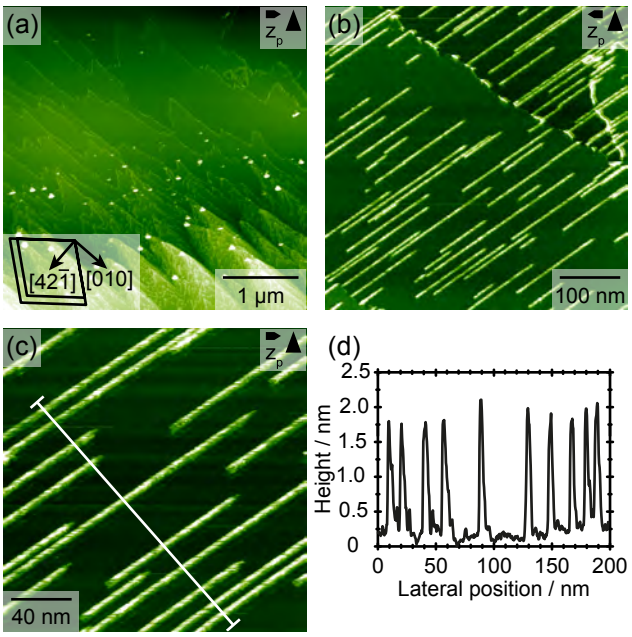

Fig. 4.10: Coexistence of surface restructuring and molecular self-assembly induced by addition of 0.16 mM EBA solution at an initial pH value of 3.6. (a) Large-scale image illustrating the characteristic surface restructuring. (b) Zoom onto a calcite (10.4) terrace, revealing unidirectional rows. (c) Further zoom onto the molecular rows with position marked of the line profile shown in panel (d).

Most importantly, these stripes are only observed for an initial pH value of the solution of 3.6, not for the solution with initial pH value of 6.3 nor 9.1. From this, we conclude that the formation of an ordered self-assembled structure requires precise control of the molecular deprotonation state. Apparently, only the one-fold deprotonated EBA species can form a self-assembled structure on the calcite (10.4) terrace. Moreover, EBT, which is a conformational isomer of EBA, does not exhibit these rows. Thus, also the conformational structure is decisive for the formation of the self-assembled rows.

Interplay of self-assembly and surface restructuring. A detailed discussion of the observed prevalence of molecule-induced surface restructuring in contrast to molecular self-assembly requires a quantitative analysis of all involved interactions, but this is a very complicated problem. A qualitative statement can, however, be made to identify the main mechanism responsible for this observation. The resulting equilibrium structure arises from a competition of all involved interactions (fig. 4.11). In solution, the water-soluble molecules possess a hydration shell and can form complexes with the dissolved species, *e.g.*, calcium ions. The surface - being hydrophilic - is covered by hydration layers with the first water layer being strongly bond to the calcium ions. For the molecules to adsorb on the surface (regardless of the position on the surface), therefore, requires breaking the molecule's hydration shell and the water-surface bond.

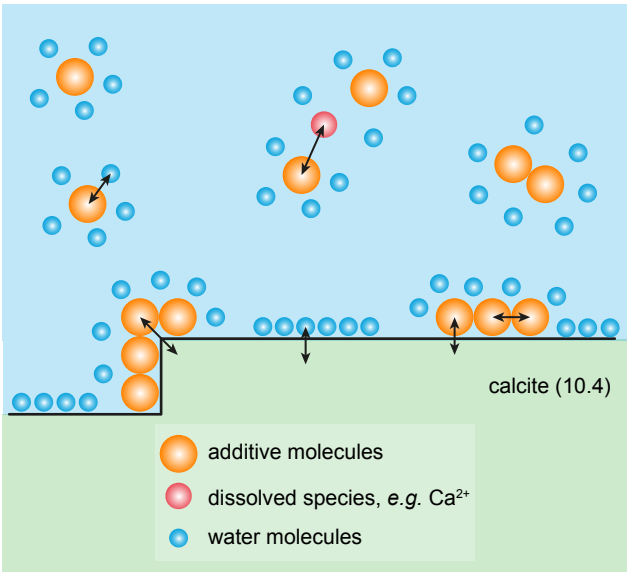

Fig. 4.11: Schematic drawing illustrating the major interactions involved. For simplicity, only few water molecules are drawn exemplarily. Several important interactions are indicated by arrows.

In the case of a water-soluble molecule and a hydrophilic surface, these two processes are typically non-favored. If reactive sites such as step edges are present on the surface, the molecule-surface interaction can become very strong, effectively dominating over all other interactions. In this case, molecule-induced surface restructuring can occur as molecules can stabilize otherwise non-favored step edges. When molecules adsorb on the defect-free terrace as in the case of a self-assembled structure, in contrast, the molecule-surface interaction is typically weaker than for adsorption at step edges. Still, it needs to be strong enough for replacing the adsorbed water molecules. Furthermore, an ordered self-assembled structure requires an intermolecular interaction that is of the same order of magnitude as the molecule-surface interaction. In essence, the formation of a self-assembled structure on the terrace is, therefore, limited to very special conditions.

Thus, the precise control of the molecule's properties required for achieving a self-assembled structure might be explained by the fact that self-assembly is based on a subtle balance between molecule-surface and molecule-molecule interactions. This balance might easily be perturbed by a small conformational change only. Additive-induced reconstruction, on the other hand, is dominated by molecule-surface interactions, which can be more insensitive to variations in the molecular structure and apparently also deprotonation state.

4.3 Summary and Conclusion - Eriochrome Azo Dyes

The impact of a class of Eriochrome azo dyes on the calcite (10.4)-water interface is studied using *in-situ* high-resolution FM-AFM. A characteristic surface restructuring is observed during calcite dissolution in the presence of the additives, irrespective of the specific dye structure, conformation and deprotonation state. The restructuring appears to be a result of specific step edge decoration by the molecules, favoring the non-polar, acute step edges and the polar step edge along the [010] direction. In sharp contrast to this prevalent surface restructuring, self-assembly of molecular rows on the terrace of the (10.4) surface is observed for one Eriochrome dye only and limited to a very narrow pH range around a pH value of 3.6. Our results indicate that while molecular self-assembly appears to require precise control over the molecular structure and deprotonation state, the surface restructuring mechanism is a more general property of the Eriochrome dyes that is robust against variations in the molecular structure and deprotonation state. This finding might be explained by the fact that molecular self-assembly is based on a subtle balance of molecule-molecule and molecule-surface interactions, while surface restructuring will be dominated by molecule-surface interactions with less impact of the molecule-molecule interaction. This insight contributes to attaining rational control in additive-induced surface modifications.

5

Controlling Molecular Self-Assembly on Calcite (10.4)

The following chapter 5 is based on the first part of the article "*Where is the Most Hydrophobic Region? Benzopurpurine Self-Assembly at the Calcite-Water Interface*" by M. Nalbach, P. Raiteri, S. Klassen, S. Schäfer, J. D. Gale, R. Bechstein and A. Kühnle, which has been accepted for publication in *The Journal of Physical Chemistry C*.[90] I performed the AFM measurements, analyzed the experimental data, prepared the figures and wrote this part of the manuscript with comments by P. Raiteri, J. D. Gale and A. Kühnle. Parts of the article are reproduced verbatim, changes have been made to make this chapter consistent with the other sections in this thesis. For this chapter, I included additional AFM data about the molecule adsorption and island growth process of Benzopurpurine on calcite (10.4).

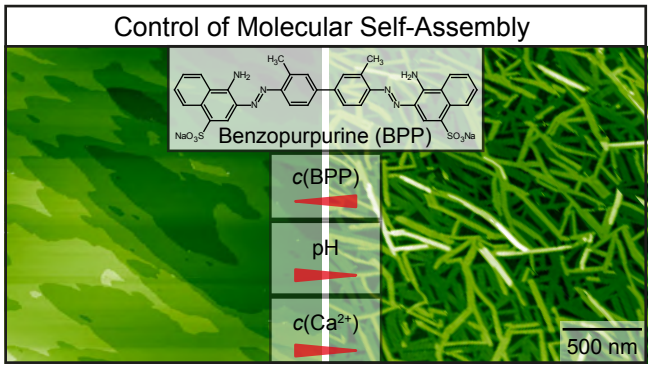

Control of molecular self-assembly at solid-liquid interfaces is challenging due to the complex interplay between molecule-molecule, molecule-surface, molecule-solvent, surface-solvent and solvent-solvent interactions. Here, we use in-situ dynamic atomic force microscopy to study the self-assembly of Benzopurpurine 4B into oblong islands with a highly ordered inner structure, yet incommensurate with the underlying calcite (10.4) surface. Molecular dynamics and free energy calculations provide insights by showing that Benzopurpurine 4B molecules do not anchor to the surface directly, but instead assemble on top of the second hydration layer.

This seemingly peculiar behavior was then rationalized by considering that hydrophobic molecules placed atop the second water layer cause the least distortion to the already existing hydration structure. Further experiments for the adsorption of Benzopurpurine 4B on other minerals indicate that the specific interfacial water structure on calcite is decisive for rationalizing the self-assembly of Benzopurpurine 4B in this system.

5.1 Introduction - Benzopurpurine

Self-assembly is a powerful tool for creating functional molecular structures at surfaces.[91,92] So far, however, most reported examples are limited to systems kept in ultra-high vacuum (UHV)[93–98] or at ambient conditions.[99,100] At solid-liquid interfaces, despite being of tremendous importance both in nature and technology,[2–5] only limited progress has been made in terms of rationally controlling molecular self-assembly by an informed choice of suitable molecules and/or solvent.[101–105] The formation of well-ordered structures on solid surfaces is steered by the subtle balance of molecule-surface and molecule-molecule interactions.[106]

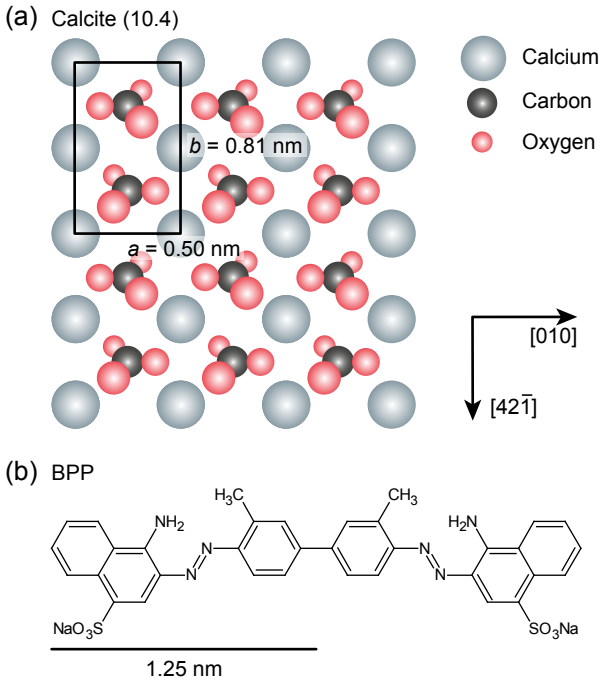

Fig. 5.1: Structure of the calcite (10.4) surface. (b) Chemical structure of Benzopurpurine 4B (BPP). The scale bar below (b) applies to both parts of the figure.

At solid-liquid interfaces, the complexity of the situation is increased because additionally molecule-solvent and surface-solvent interactions play a decisive role in determining the adsorption configuration. This complexity severely hampers the rational control of self-assembly at the mineral-water interface. For example, for many molecules studied at the mineral-water interface, it even remains impossible to predict whether or not an ordered structure will form.

In-situ dynamic atomic force microscopy (AFM) has been shown to provide atomic and molecular-resolution information for mineral surfaces,[34,72] molecular structures,[15,17,19,35,107,108] hydration structures,[77,82,83,109–112] as well as the possibility of chemical identification at the solid-liquid interface.[113] Nevertheless, a comprehensive molecular understanding of adsorption and self-assembly processes is still missing and computer modelling has been often used to further our knowledge. For calcite, the most stable polymorph of calcium carbonate at ambient conditions, and its natural cleavage plane, (10.4) (fig. 5.1a), extensive simulation studies have helped yield a molecular scale picture of the interfacial structure, which agrees remarkably well with experiment.[9,84,114,115] Computational work has also been used to understand the interaction of organic molecules with calcium carbonate.

Benzopurpurine 4B (BPP, fig. 5.1 b) is a commonly used textile dye[116,117] and structurally closely related to Congo Red, which has previously been studied with *in-situ* dynamic AFM on the calcite (10.4) cleavage plane.[17] Congo Red has been shown to drastically restructure the calcite (10.4) surface, indicative of a strong molecule-surface interaction perhaps mediated through the negatively charged sulfonate (SO_3^-) groups. Therefore, a strong molecule-calcite interaction might be expected for BPP as well. In the present study, we use a combination of *in-situ* AFM and computer simulation to examine whether this is indeed the case.

Materials and Methods

Solution preparation. Benzopurpurine 4B (BPP) is purchased from TCI Deutschland GmbH as a disodium salt (Na_2BPP) and used without further purification.

Further experimental details about solution preparation, instrumentation, measurement condition and the *in-situ* AFM setup information can be found in section 2.2, section 2.3 and section 2.4.

5.2 Results and Discussion I - Benzopurpurine

Structure formation of BPP on calcite (10.4). Here, *in-situ* dynamic AFM shows the formation of oblong islands (fig. 5.2 and fig. 5.3) that exhibit a rather uniform width of between 40 to 70 nm.

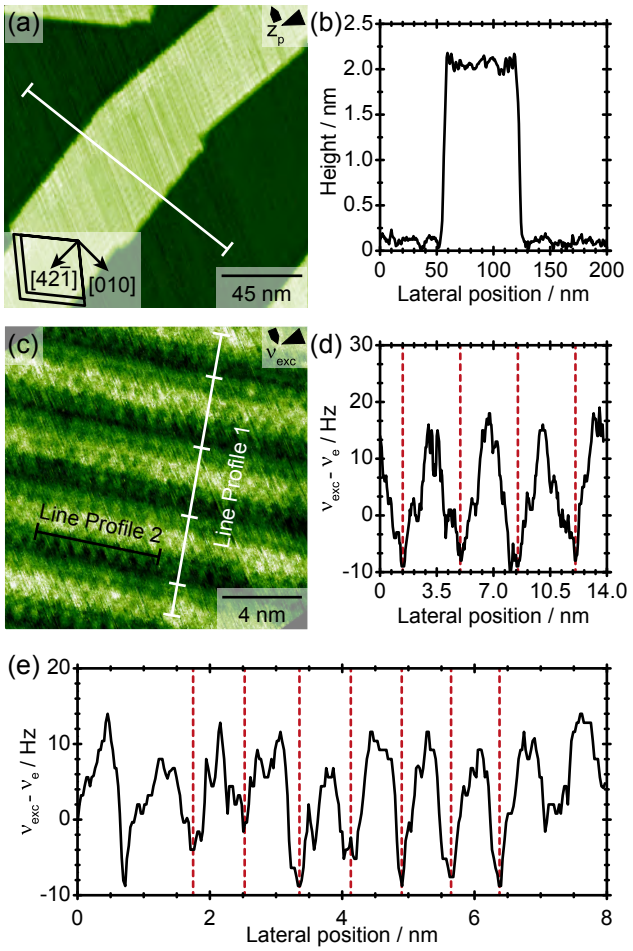

Fig. 5.2: Molecular adsorption of BPP on the calcite (10.4) surface. (a) AFM image showing a BPP island on calcite (10.4) at a solution pH of 7.7 (c(BPP) = 72 μM). (b) Line profile taken at the indicated position in (a), revealing an island width of 70 nm and an apparent island height of approximately 2.2 nm. (c) Drift corrected, high-resolution frequency shift image of the molecular structure of a BPP island on the same sample. (d) Line profile 1 taken at the indicated position in (c), revealing a stripe-to-stripe distance of approximately 3.5 nm. (e) Line profile 2 taken at the indicated position in (c), revealing a periodicity of approximately 0.8 nm within a molecular stripe.

At low concentration, the profile line measured across one 70 nm wide BPP island (fig. 5.2 a) shows an apparent height of 2.2 nm (fig. 5.2 b), while at high concentrations the formation of multilayer islands with heights of up to 10 nm is observed. It should be stressed that AFM – similar to other scanning probe microscopy techniques – does not provide true topography information. Therefore, while lateral periodicities can be provided with high accuracy, vertical heights have to be considered with care, which is why we refer to an apparent height. A high-resolution image of one

of the BPP islands reveals ordered molecular stripes within the island (fig. 5.2 c) with a stripe-to-stripe distance of approximately 3.5 nm (fig. 5.2 d). Additionally, a periodicity within one stripe of approximately 0.8 nm can also be measured (fig. 5.2 e).

Variation of the BPP concentration. We study BPP solutions with a concentration ranging from 1.7 up to 110 μM at a solution pH of 3.5. Below a BPP concentration of 3.0 μM, no structure formation can be observed, indicating a minimum concentration for BPP to assemble onto calcite (10.4). In fig. 5.3, the calcite (10.4) surface is shown in the presence of 3.0, 4.7, 5.8 and 8.3 μM BPP at a solution pH of 3.5.

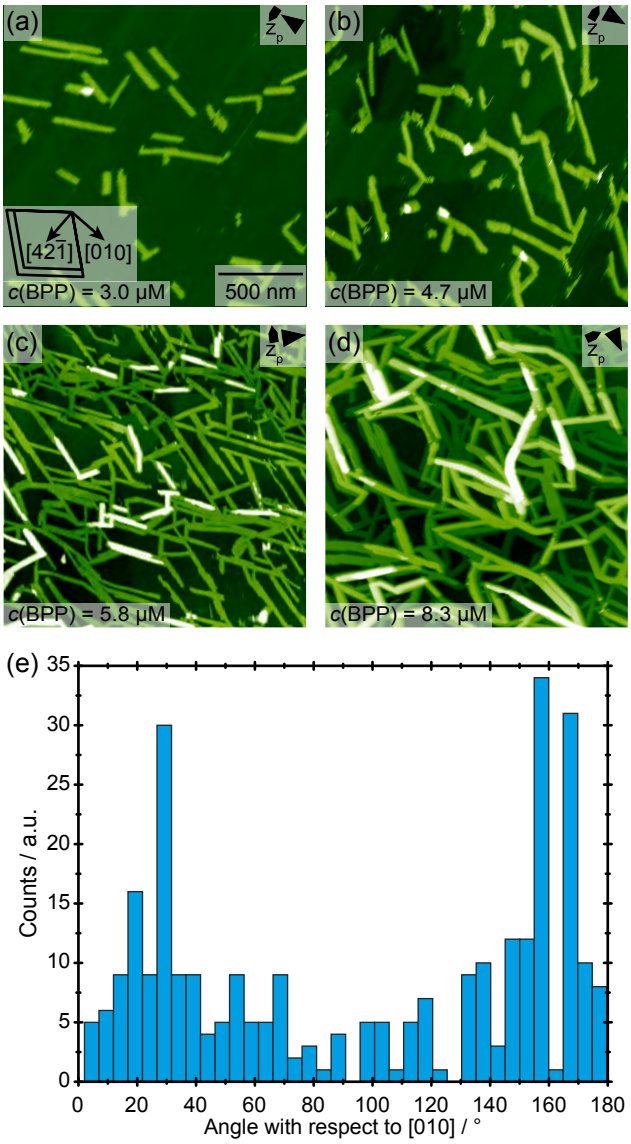

Fig. 5.3: Representative AFM images illustrating the oblong BPP islands on calcite (10.4) as a function of BPP concentration. (a)-(d) Calcite (10.4) surface in the presence of 3.0, 4.7, 5.8 and 8.3 μM BPP, from left to right, at a fixed solution pH of 3.5. Variation of the pH in a range from pH 3.5 to 11 does not reveal any influence of the pH on the island shape reported here. The scale bar in image (a) applies to all images in this series. (e) Angle histogram illustrating the orientation of the islands with respect to the underlying calcite lattice.

For concentrations below 5.0 μM, almost exclusively monolayer height BPP islands are present (fig. 5.3 a and fig. 5.3 b). Increasing the BPP concentration increases preferentially the coverage of the first layer, meaning a higher density of monolayer islands on the calcite (10.4) substrate. In fig. 5.3 c, a significantly higher coverage of the first layer, as well as a second layer, which grows perfectly on top of first-layer islands, is visible. From this, we can deduce that BPP is able to adsorb on both, the calcite (10.4) surface, indicating sufficient molecule-substrate interaction, as well as onto already existing BPP islands, showing adequate molecule-molecule interaction. Further increasing the BPP concentration still increases the coverage in the first layer, but now the BPP molecules tend to adsorb more commonly onto monolayer or even higher-layer islands. At a BPP concentration of 8.3 μM already up to four layers of molecular islands can be observed (fig. 5.3 d). For all concentration measured, even for the highest ones of 110 μM, a complete full coverage of the first layer can not be achieved. Interestingly, the islands exhibit various orientations with respect to the underlying substrate lattice. In particular, the high symmetry directions [010], and $[0\bar{1}0]$, $[42\bar{1}]$ and $[\bar{4}2\bar{1}]$, as well as the etch pit directions $[4\bar{4}\bar{1}]$, $[\bar{4}41]$ and $[48\bar{1}]$, $[\bar{4}\bar{8}1]$ - corresponding to the angles 0°, 90°, 39°, 129° with respect to the [010] and $[0\bar{1}0]$ direction – do not appear to be favored. To quantify the latter observation, we present an angle histogram in fig. 5.3 e, illustrating that a broad angle distribution can be found with no clear tendency for a certain island orientation.

BPP coverage analysis. The coverage of BPP molecules on calcite (10.4) is determined quantitatively using the software Gwyddion.[118]

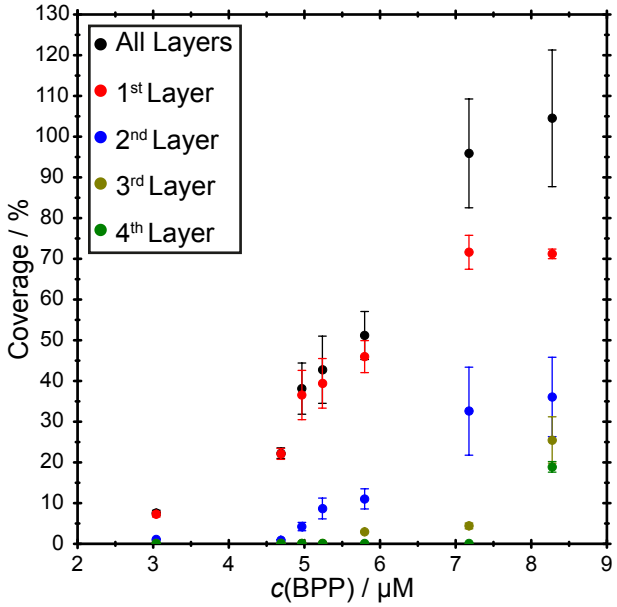

Fig. 5.4: Estimated coverage of BPP islands on calcite (10.4) as a function of the BPP concentration for all layers combined (black dots) and each layer separately (red, blue, olive and green dots). The error is given by the standard deviation.

In fig. 5.4, the sum of the coverage for all layers (black dots) and each of the four layers separately (red, blue, olive and green dots) are plotted as a function of the BPP concentration. For each experiment, at least five consecutively obtained images, in which qualitatively no more change in coverage is observable, are used to measure the coverage. The values for the coverages plotted in fig. 5.4 correspond to the average over all analyzed images for each experiment with a different BPP concentration. The combined coverage for all layers, as well as for the first layer, is determined with respect to the total scan area of the calcite (10.4) substrate. The coverage for the second, third and fourth layer instead, is determined with respect to the covered area of the underlying molecular layer.

The total coverage, as well as for all layers separately, increases with increasing BPP concentration, as expected. Below a BPP concentration of 5.0 μM, the total coverage of about 40% is contributed by the first layer alone. The second layer reaches a coverage of 20% not until a BPP concentration of 7.0 μM. From this point on, the coverage of the first layer does not increase any longer and remains nearly constant at around 70%, while the coverage of the second, third and fourth layer further increases. This indicates that the maximum density of monolayer islands in the first layer is reached. Furthermore, it shows that the adsorption onto already existing molecular islands gets more and more favored with increasing BPP concentration, rather than a further adsorption onto the calcite (10.4) substrate.

The quantitative analysis of the coverage of BPP molecules on calcite (10.4) shows that the molecules are able to adsorb onto both, the underlying substrate, as well as already existing molecular islands, indicating sufficient molecule-substrate and molecule-molecule interaction at the same time. Furthermore, increasing the molecule concentration reveals that the preference for BPP to adsorb either onto underlying substrate or the already existing molecular islands is not the same in the concentration range measured here. For lower concentration, BPP adsorbs more likely directly onto the calcite (10.4) substrate. With increasing concentration, the BPP molecules tend to adsorb more preferentially onto already existing molecular islands, rather than onto the underlying calcite (10.4) substrate.

Variation of the solution pH. In previous *in-situ* AFM studies it has been shown that controlling the pH of the solution is crucial for achieving molecular self-assembly on calcite (10.4),[15] but this is a very complicated problem. Not only does the solution pH dictate the protonation / deprotonation state of BPP, but it also significantly affects the structure of the surface and the entire mineral-water interface, and hence changes the adsorption behavior of the dye molecule onto the calcite (10.4) substrate.

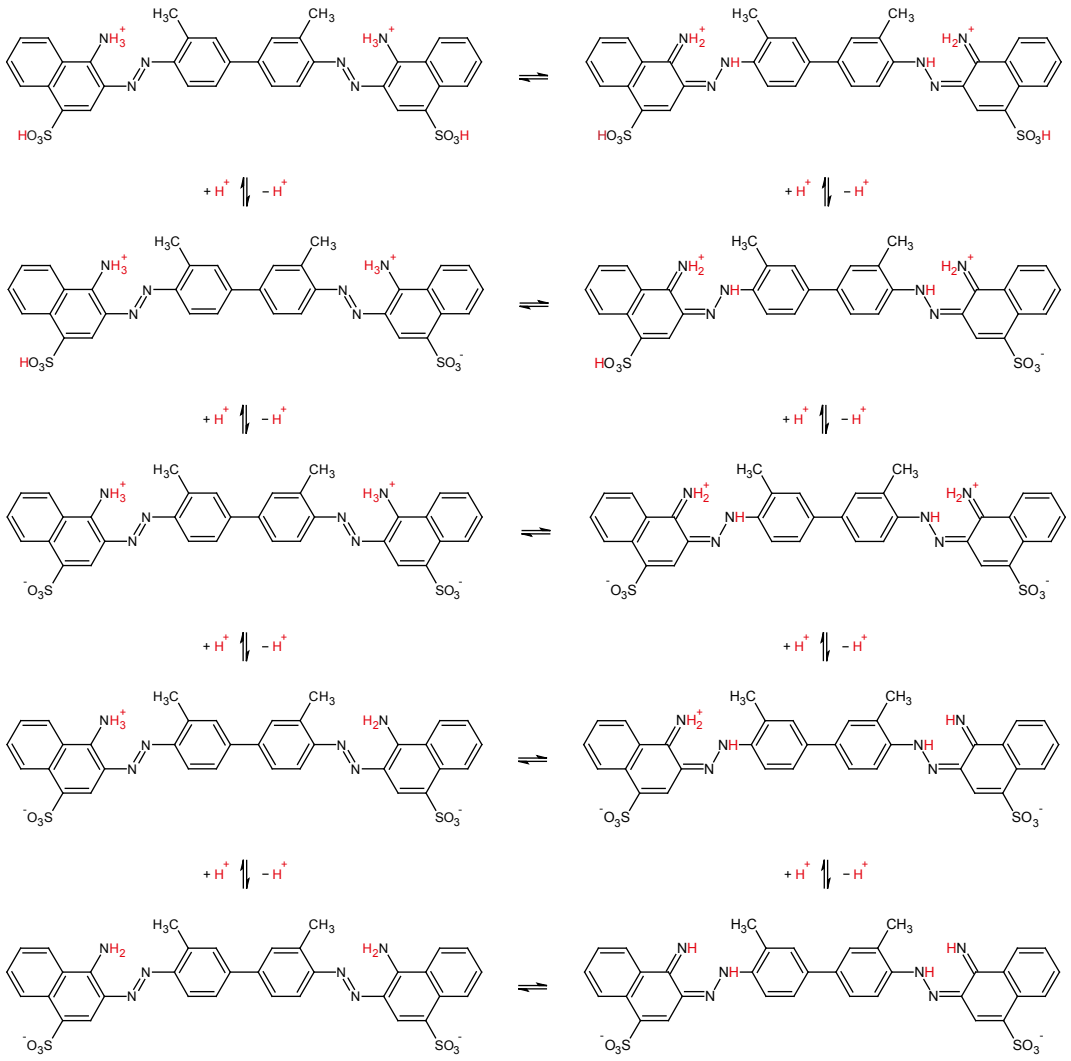

Fig. 5.5: Protonation / deprotonation behavior and azo-hydrazo tautomerization of BPP. The stepwise deprotonation behavior, starting from the fully protonated (H_4BPP^{2+}) species to the four-fold deprotonated (BPP^{2-}) species, is displayed from top to bottom. The azo-hydrazo tautomerization for each protonated / deprotonated species is illustrated from left to right. Relevant protons for the protonation / deprotonation are highlighted in red. For simplicity only the symmetric tautomers are shown.

The structure of a BPP molecule (fig. 5.1 b) consists of two sulfonate ($-SO_3^-$) and two amino groups ($-NH_2$), resulting in five different possible protonated / deprotonated species (a fully protonated (H_4BPP^{2+}), a one-fold deprotonated (H_3BPP^+), a neutral two-fold deprotonated (H_2BPP), a three-fold deprotonated ($HBPP^-$) and four-fold deprotonated (BPP^{2-}). Additionally, every protonated / deprotonated species of BPP can undergo an azo-hydrazo tautomerization,[119–121] leading to a total number of 20 species (10 symmetric and 10 antisymmetric) being theoretically present in the solution (fig. 5.5).

pH-dependent molecule adsorption and island growth. To study the pH dependence of the structure formation of BPP on calcite (10.4), we study BPP solutions with a pH ranging from 3.5 up to 11. The results for the *in-situ* AFM experiments with different solution pH illustrate that the formation of the molecular islands itself does not depend on the pH. With the possible exception of the most alkaline condition (pH $\sim$ 11), we find the same molecular self-assembly of the BPP islands. However, the timescale of the process of molecule adsorption and island growth is strongly pH-dependent (fig. 5.6).

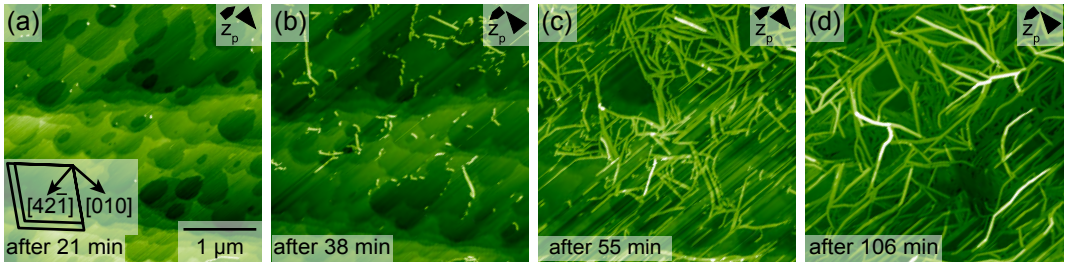

Fig. 5.6: Image series of the calcite (10.4) surface in the presence of BPP demonstrating the molecule adsorption and island growth process. Image (a) is taken 21 minutes after injecting a 66 μM solution of BPP with a pH of 7.3 showing an restructured, but molecule free calcite (10.4) surface. The images (b), (c) and (d) are taken 38, 55 and 106 minutes after the start of the experiment. With increasing time of the experiment, BPP molecules adsorb onto step edges and terraces and BPP islands grow from there on in plane and height. The scale bar in (a) applies to all images in this series.

Fig. 5.6 a represents the first image of the calcite (10.4) surface 21 minutes after injecting a 66 μM solution of BPP with a pH of 7.3. The calcite (10.4) substrate is characteristically restructured but no molecules are adsorbed. After 17 minutes, the first molecular islands are visible; the BPP molecules adsorb preferentially onto step edges and the molecular islands grow from there (fig. 5.6 b). Only 60 minutes after solution injection, the calcite (10.4) surface is almost 50% covered in the first layer with BPP molecules and additionally also the second layer starts to form (fig. 5.6 c). After 106 minutes from the time of injecting the solution, qualitatively no further change in coverage is observable (fig. 5.6 d).

System state analysis. Fig. 5.7 summarizes the pH dependence of the molecule adsorption and islands growth process of BPP on calcite (10.4) for three different BPP concentration ranging of 66 to 110 μM, 18-21 μM and 8-13 μM. For each concentration (high, medium and low), AFM imaging series are taken at a given pH value. The time that has elapsed since the injection of the solution into the liquid cell is given on the ordinate axis. The minimum time between solution injection and first image being recorded is about 15 minutes, meaning there is a short time frame that is not accessible within the *in-situ* AFM experiment. In fig. 5.7, a green dot represents a molecule free calcite (10.4) surface. A blue dot corresponds to the situation where BPP molecules adsorb and BPP islands grow on the surface, causing an increase of the coverage with time. Finally, all images, where qualitatively no change in coverage is observable anymore, is labelled with a red dot.

In fig. 5.7 a, all images from measurements with a BPP concentration ranging from 66 to 110 μM are plotted. Starting with a pH of 3.5, all measurements up to a pH of 4.5 show directly after injecting the solution qualitatively no further change in coverage. Above a pH of 4.5 and up to a pH of around 8.0, the coverage on the first image recorded is decreased compared to the measurements with lower pH. Additionally, the time necessary to reach the point at which no further coverage change is observed increases too. Above a pH of 8.0, no BPP molecules can be observed in the first images after solution injection. Similar to the growth of BPP islands for pH values between 4.5 and 8.0, here, with increasing pH, the time of first molecules adsorbing on the calcite (10.4) surface increases and the time of reaching the situation of no more coverage change increases even further. For the pH of almost 11, no molecules can be observed at all within the measuring time of the experiment of about 350 minutes. Adjusting the pH, thus, enables controlling the time of adsorption of BPP molecules for starting condition above a pH of 4.5, as well as the time of reaching the situation of no more coverage change. Additionally, for high alkaline pH, it allows for a complete inhibition of the adsorption of BPP onto calcite (10.4).

For the lower concentration range of 18-21 μM (fig. 5.7 b) and 8-13 μM (fig. 5.7 c) the above-described trend of the pH dependence still remains valid. For a pH of 3.5, the situation of no more coverage change is directly observable after injecting the solution. Increasing the pH for the medium and low concentrations also decelerates the molecule adsorption and island growth process for BPP, resulting in the same system state, where no molecules are present in the first image taken after the solution injection.

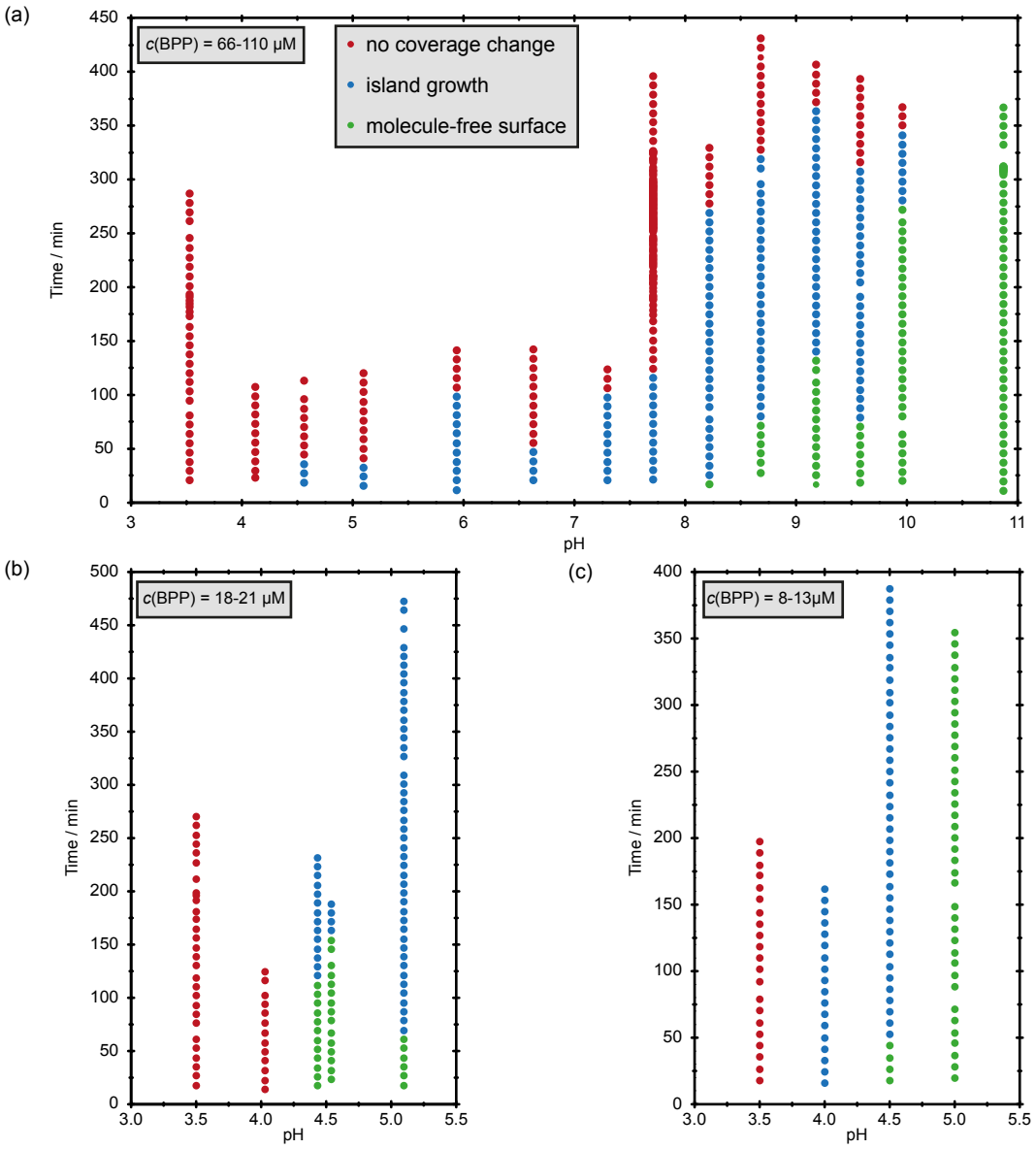

Fig. 5.7: System state diagram for the pH dependence of the molecule adsorption and island growth processes of BPP on calcite (10.4). For three different concentration ranges, the observed system state is plotted as the time displacement from the point of injecting the solution against the pH. (a) BPP concentration ranging from 66 to 110 μM, pH ranging from 3.5 up to almost 11. (b) BPP concentration ranging from 18 to 21 μM, pH ranging from 3.5 up to 5.5. (c) BPP concentration ranging from 8 to 13 μM, pH ranging from 3.5 up to 5.5. Every red dot corresponds to an AFM image where qualitatively no change in coverage is observable anymore. Every blue dot indicates already adsorbed BPP molecules and island growth in quantity and size. Every green dot represents a molecule-free calcite (10.4) surface.

However, the pH, at which no molecules are present and at which the situation is described as growth condition, respectively, decreases with decreasing BPP concentration. While for the highest concentrations (66-110 μM) the situation of no more coverage change at a pH of around 5 is reached within the first hour after injecting the solution, for the medium concentrations (18-21 μM), the same situation cannot

be reached at all. Here, we only observe adsorption of BPP molecules and growth of the BPP islands. For the lowest concentrations (8-13 μM) at a pH of around 5 no molecules at all can be found within the measuring time of the experiment. The lower the BPP concentration, the lower the pH of the solution, at which the molecule adsorption and island growth process is decelerated.

The adsorption of BPP molecules and growth of BPP islands on calcite (10.4), characterized by the existence of three consecutive system states, significantly depends on both, the pH of the solution and the BPP concentration. Variation of the pH allows for precise control of the timescale for BPP molecules adsorbing onto the calcite (10.4) surface and BPP island growth until the system reaches the situation of qualitatively no more coverage change. Increasing the pH decelerates the process and leads, within the time of the experiment, to a complete molecule free calcite (10.4) surface for high alkaline pH. Variation of the BPP concentration, in particular decreasing the concentration, shows that the pH window for the three identified system states narrows down, meaning that for lower BPP concentration only for acidic starting condition a molecule adsorption and island growth is visible.

Variation of the calcium ion concentration. Dissolved azo dyes molecules are known to form calcium complexes with free calcium ions in solution[27] and according to a proposed coupled dissolution and precipitation mechanism,[16] these calcium complexes might also adsorb onto the calcite (10.4) substrate. In undersaturated calcium carbonate solutions, calcium ions are released from an immersed calcite crystal into the bulk solution. If the formation of BPP islands on calcite proceeds *via* the adsorption of Ca-BPP clusters on the mineral surface, we should therefore observe a dependence of coverage with pH and with the amount of free calcium in solution. The first and simplest experiment that can be performed to test this hypothesis is to add additional calcium ions to solutions with different initial pH values and to see if we observe the earlier formation of molecular islands, as compared to a solution with the same initial pH, but with no additional calcium ions. We study solutions with BPP concentration of 72-84 μM, pH ranging from 3.5 to 9.2 and calcium ion concentration of 15-80 μM, resulting in a ratio of BPP molecules to free calcium ions of 1:5.5, 1:4, 1:2.7, 1:2 and 1:1 (BPP:Ca^{2+}), respectively. At all conditions, no significant acceleration of BPP adsorption and island formation can be observed in the presence of additional calcium ions. Instead, with increasing ion concentration in solution the surface coverage decreases up to the point where no molecules at all are adsorbed on the calcite (10.4) surface. Therefore, we propose that BPP indeed forms a complex with calcium in solution, but the complex seems not adsorb onto the calcite (10.4) substrate and rather the presence of calcium ions in the solution inhibits the structure formation of the molecular islands.

6

Benzopurpurine Self-Assembly at the Calcite (10.4)-Water Interface

The following chapter 6 is based on the second part of the article "*Where is the Most Hydrophobic Region? Benzopurpurine Self-Assembly at the Calcite-Water Interface*" by M. Nalbach, P. Raiteri, S. Klassen, S. Schäfer, J. D. Gale, R. Bechstein and A. Kühnle, which has been accepted for publication in *The Journal of Physical Chemistry C*.[90] The MD simulations shown in this section were performed and analyzed by P. Raiteri. The second part of the manuscript was written by P. Raiteri with comments by M. Nalbach, J. D. Gale and A. Kühnle. With the exception of the toc figure, figure 6.8 a and figure 9, all figures have been prepared by P. Raiteri. The toc figure, figure 6.8 a and figure 9 have been prepared by M. Nalbach. Parts of the article are reproduced verbatim, changes have been made to make this chapter consistent with the other sections in this thesis.

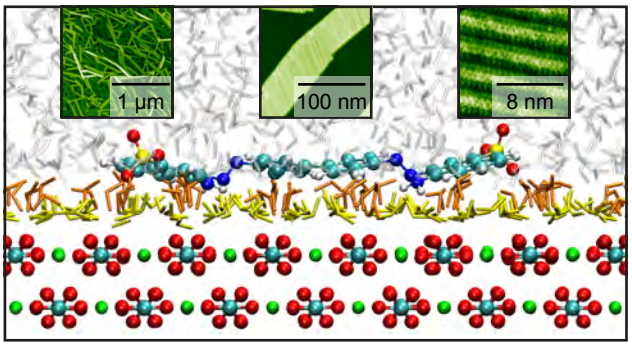

Control of molecular self-assembly at solid-liquid interfaces is challenging due to the complex interplay between molecule-molecule, molecule-surface, molecule-solvent and surface-solvent interactions. Here, we use in-situ dynamic atomic force microscopy to study the self-assembly of Benzopurpurine 4B into oblong islands with a highly ordered inner structure, yet incommensurate with the underlying calcite (10.4) surface. Molecular dynamics and free energy calculations provide insights by showing that Benzopurpurine 4B molecules do not anchor to the surface directly, but instead assemble on top of the second hydration layer. This seemingly peculiar behavior was then rationalized by considering that hydrophobic molecules placed atop the second water layer cause the least distortion to the already existing hydration structure.

Further experiments for the adsorption of Benzopurpurine 4B on other minerals indicate that the specific interfacial water structure on calcite is decisive for rationalizing the self-assembly of Benzopurpurine 4B in this system.

6.1 Molecular Dynamics Setup - Benzopurpurine

Molecular dynamics (MD) simulation of BPP in water with and without a calcite slab are performed using the LAMMPS code[122] augmented with the PLUMED2.2 plugin[123] for the calculation of the pairing adsorption free energies. All the simulations are performed at constant volume (NVT) after an initial equilibration of the cell at 1 atm. The equations of motions are integrated using the velocity-Verlet algorithm with a 1 fs time step and the temperature is kept at 300 K with a chain of 5 Nosé-Hoover thermostats and a relaxation time of 0.1 ps. The GAFF1.7 force field[124] is used to describe the BPP, BPP-water and BPP-calcite/gypsum interactions, as well as the intramolecular component for BPP; the calcite and sodium/calcite-water interactions come from previous works,[84,125–127] while the gypsum water interactions are taken from our recent work.[128]

It is important to note here that the calcite-water interactions used in this work have been carefully parameterized and tested against thermodynamic experimental data that include the hydration free energy of the ions, the solubility of calcite, the Ca-CO_3 ion pair association constant, as well as the water structure above the calcite surface that compares well with X-ray reflectivity data. Moreover, the SPC/Fw water model[129] used in this work gives an accurate representation of the liquid phase over a wide range of temperatures.

Properties, such as the water solvation free energy, dielectric constant and structure, are found to be in good agreement with experiment for this water model.[125] On the other hand, the interactions involving BPP are much harder to benchmark due to the lack of experimental data to compare against; quantities such as the solvation free energy of BPP or the BPP-calcium pairing free energy are indeed unknown. Due to the complexity of the molecule, it is currently too expensive to run *ab initio* calculations in bulk water for a sufficiently long time to obtain benchmark data against which to calibrate the force field. Although the precise quantitative values of the association and adsorption free energies obtained from the simulations need to be treated with appropriate caution, we believe the simulations can qualitatively reproduce and explain the experimental observations.

The free energies calculations are performed using the multiple walkers well-tempered metadynamics technique[130–132] and a bias factor of 12 is chosen to ensure convergence of the calculations. The initial Gaussian height is set to k_BT and their width to 0.2 Å. The pairing free energy between two BPP molecules is calculated by inserting two dye molecules and 4 Na^+ ions in a 100 Å box of water with 3D periodic boundary conditions (PBC). Because of the size of BPP the pairing mechanism could be quite complex and the reaction coordinate is not immediately evident, as for two monoatomic or small ions. We therefore repeated the calculations using two different collective variables (CV): the mean distance between all the atoms in the two BPP molecules and the distance between their centers of mass, as implemented in PLUMED2.2.

The adsorption free energy of BPP on the calcite (10.4) and gypsum (020) surfaces are computed using a 3D periodic cell containing a 12 and 8 layers thick slab, respectively. A 6x10 (10x10) surface supercell of calcite (gypsum) is created and separated from its periodic image by a space of approximately 40 Å (60 Å) which is then filled with water at the density of the bulk liquid. One BPP molecule and two Na^+ counter-ions are also inserted in the box. As the CV we used the z-component of the distance between the center of mass of BPP and a Ca^{2+} ion in the middle of the mineral slab.

We also consider the adsorption of a second BPP molecule on the mineral surface to form an adsorbed dimer, which could be regarded as the first nucleus of a BPP island. Because of the many different available pathways for this process, this is a very computationally challenging task and some simplifications of the problem are necessary. In order to estimate the adsorption free energy, we restrain one BPP to stay in the adsorbed state by using a harmonic potential acting on the z-component of the distance between the BPP center of mass and one calcium atom deep in the calcite slab. In order to minimize the effect of the restraint we use a spring constant of 0.4 eV/$Å^2$, which follows the adsorption free energy profile for one molecule. As a collective variable for the metadynamics calculations we decide to use the z-component of the distance between the centers of mass of the two BPP molecules and to limit the configurational space to be explored we place harmonic “walls“ at 20 Å. The bias factor is also reduced to 8 to accelerate the convergence. Unbiased MD simulations of a stack of 8 BPP molecules on the (10.4) surface of calcite have been performed in the NVT ensemble to assess the stability of the stack and assess whether the oscillations in the AFM measurements are compatible with this structure. The stack is built by replicating one of the configurations of the dimers 4 times along an axis normal to the BPP aromatic system. After the stack is inserted above the calcite surface the pressure is equilibrated by varying the z-axis in a 5 ns NPT run and the system is then further run for 15 ns in the NVT ensemble.

6.2 Results and Discussion II - Benzopurpurine

In order to rationalize the experimental observations, we use computer simulations to estimate the strength of BPP-BPP interactions, as well as the adsorption free energy of BPP on the calcite (10.4) surface. It is well known that organic dyes in aqueous solution tend to form stacks at high concentration[117,133–136] and BPP has been reported to form aggregates as long as several μm.[117] As per our previous work on the Sunset Yellow dye,[137] we calculate the free energy to separate two BPP molecules in water using metadynamics simulations.[130] The computed binding free energy is of the order of -31.5/-35.5 kJ/mol (fig. 6.1), which is similar to the value for Sunset Yellow (-28 kJ/mol[137]), and an experimental estimate ($\sim$ -26 kJ/mol[117]). For both BPP and Sunset Yellow, force field simulations predict a binding between the dyes that is approximately 10 kJ/mol stronger than the experimental estimates.

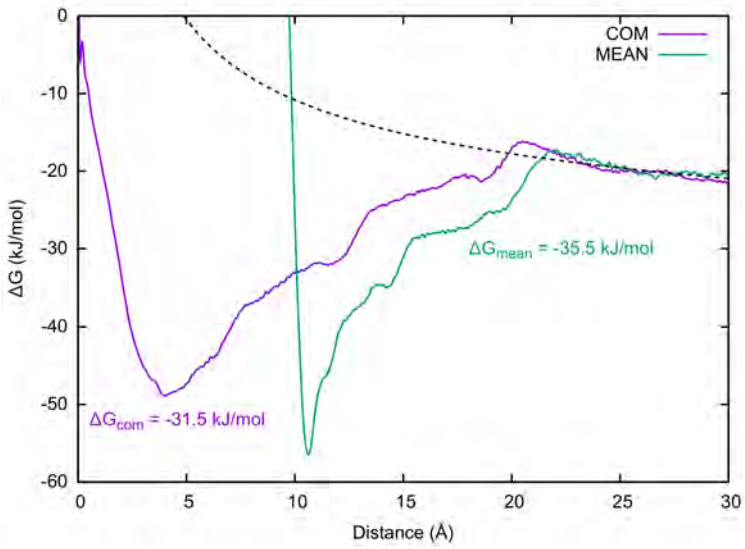

Fig. 6.1: Pairing free energy between two BPP molecules as a function of the distance between centers of mass ("COM") and of the mean distance ("MEAN") between two BPP molecules. The dashed line indicates the asymptotic limit for the binding free energy in the long-range limit which is used to demonstrate convergence and extract the free energy at standard conditions. Representative dimer conformations can be seen in fig. 6.2. It is reassuring that the computed binding free energy is largely independent of the CV used (in comparison to ambient thermal energy ($\tilde{k}_B$T).

Although there might be some fundamental differences between the calculated free energy and the experimental estimates, this discrepancy is most likely to be due to a systematic error in the force field hydration free energies. Analogously to Sunset Yellow, the molecules in a BPP dimer prefer a parallel arrangement (fig. 6.2) that maximizes π-π stacking and minimizes the amount of "surface" exposed to water. Due to this large exothermic binding free energy, the formation of aggregates (stacks) in solution is thermodynamically favorable, despite the negative charge

on the molecules, and is responsible for the formation of liquid crystals at high concentrations.[117,133–136] However, the BPP concentrations used in the present work (1.7-110 μM) are much lower than those required to form liquid crystals and simple models[137,138] that predict the average number of molecules in aggregates indicate that BPP is largely isolated in solution. It is therefore safe to assume that the adsorption of BPP on calcite is likely to proceed one molecule at a time, rather than *via* pre-assembled stacks.

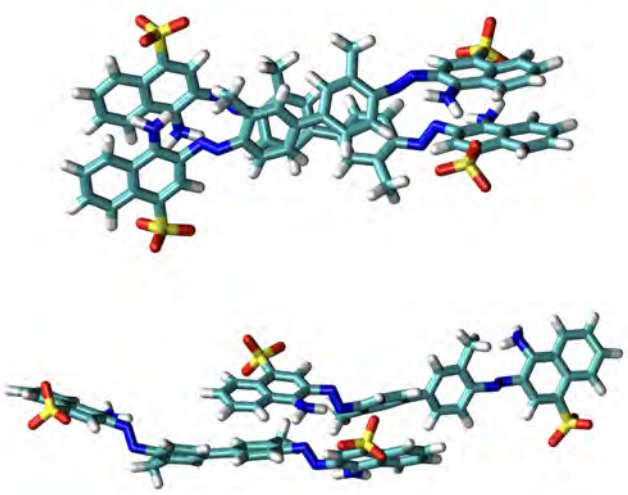

Fig. 6.2: Representative configurations of the BPP dimer corresponding to the minimum of the pairing free energy curve (top) and the small shoulder at 12 Å (15 Å) in the pairing free energy profile (bottom) in fig. 6.1, calculated using the distance between the centers of mass ("mean" distance) CV.

Our calculations of the adsorption of BPP on the basal plane of calcite predict the adsorption free energy is approximately -34 kJ/mol (fig. 6.3) and shows that the most stable adsorbed state has the BPP lying flat relative to the surface (fig. 6.4) while the shallow minimum at 15 Å above the surface corresponds to configurations where BPP is perpendicular (fig. 6.5). The somewhat surprising finding is that in both adsorbed states BPP is never in contact with the calcite surface, but instead lays on top of the second ordered water layer (fig. 6.3).

The above observation can be rationalized by considering that BPP has large hydrophobic sections and therefore tries to minimize its interaction with bulk water (fig. 6.6), an effect that, together with π-π interaction, is also responsible for the formation of long stacks of organic dyes in aqueous solution. When BPP approaches the calcite surface there are already two well organized water layers in which the water molecules are strongly coordinated to the calcium ions (first layer) or hydrogen bonded to carbonate (second layer).[84,114,139] The orientation of the water molecules above the calcite surface is therefore strongly dictated by the presence of the mineral and the hydrogen bonds within these two layers and with bulk water are therefore weakened.

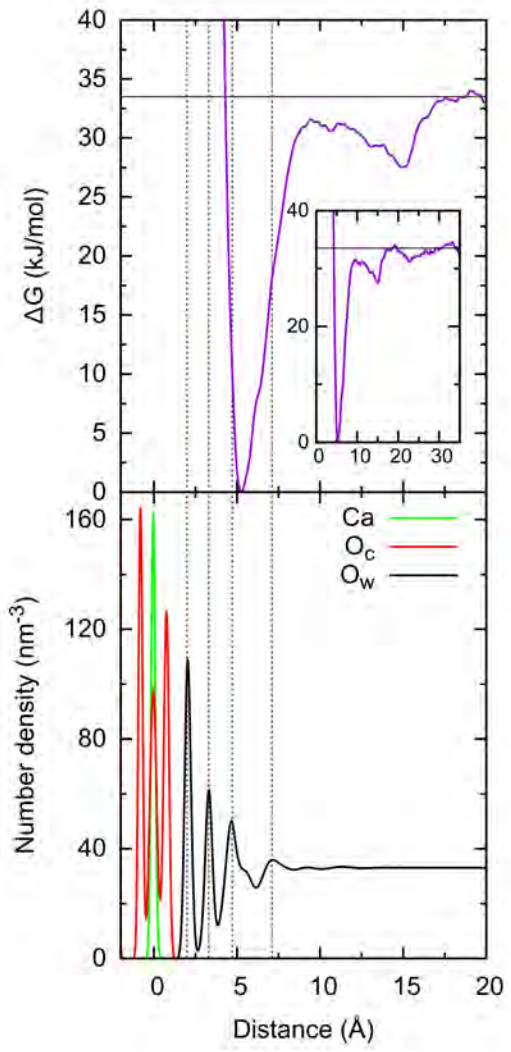

Fig. 6.3: Free energy of a single BPP molecule onto calcite (10.4) as a function of distance from the surface relative to the most stable adsorption site (top) and density profiles (bottom) for calcium (green) carbonate oxygen (red) and water oxygen (black). The position of the calcite surface, defined as the average position of the top Ca layer, is set to zero. The dashed vertical lines mark the positions of the four main peaks in the water density profile, while the solid horizontal black line at 33.5 kJ/mol indicates the estimated adsorption free energy of BPP on the calcite (10.4) surface.

Consequently, the adsorption of BPP on the second water layer has a smaller energy penalty than remaining in bulk water, where water molecules on both sides of BPP would incur a penalty for reorganizing their hydrogen bonding network. Moreover, removing the strongly bound water molecules from the first two layers to allow for direct binding of BPP to the calcite surface is also highly unfavorable (fig. 6.3). By borrowing a terminology commonly used in organic chemistry, we can say that the adsorption of BPP on calcite is driven by a "hydrophobic effect" rather than by electrostatic interactions with the mineral surface. Small regions of BPP, like the sulfonate ($-SO_3^-$) groups, the amino ($-NH_2$) groups or the diazo (-N=N-) bridges, can still interact electrostatically with the ionic surface of calcite, but because of the

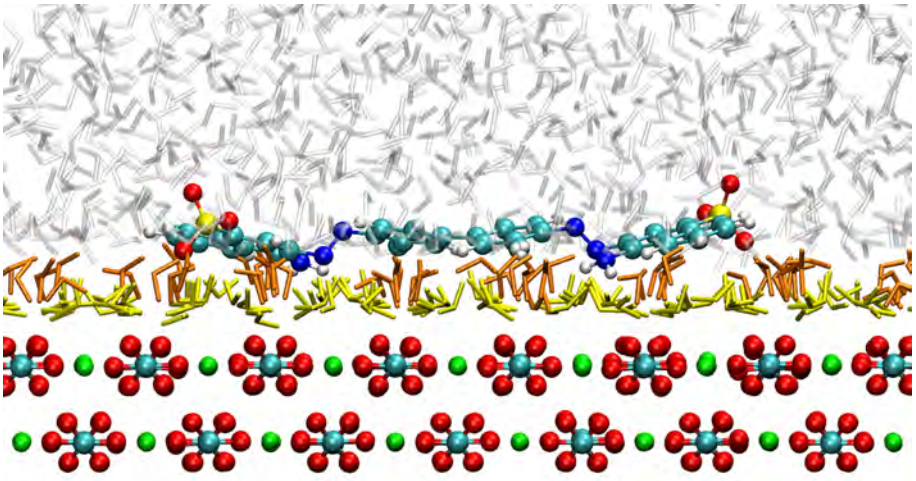

Fig. 6.4: A representative atomic configuration corresponding to the free energy minimum in fig. 6.3 is shown with calcium, carbon, oxygen, sulfur, nitrogen and hydrogen colored green, light blue, red, yellow, dark blue and white, respectively. Water molecules of the first calcite hydration layer are shown in yellow, those in the second hydration layer in orange and those in the outer layers are shown as transparent gray molecules. The positions of the atoms of the mineral are averaged over 5 ps to reduce noise, while the positions of the water and BPP atoms are from one single frame.

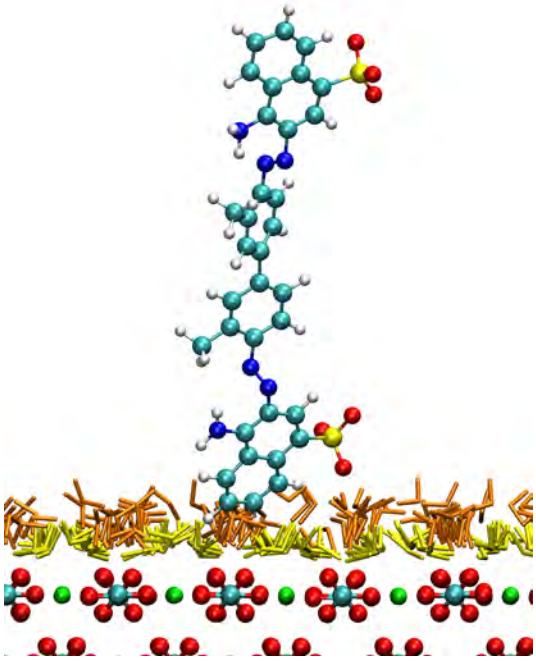

Fig. 6.5: A representative atomic configuration corresponding to the shallow minimum at 15 Å in fig. 6.3 is shown with calcium, carbon, oxygen, sulfur, nitrogen and hydrogen colored green, light blue, red, yellow, dark blue and white, respectively. Water molecules of the first calcite hydration layer are show in yellow, those in the second hydration layer in orange, while those in subsequent layers and bulk water are omitted for clarity. The positions of the atoms of the mineral have been averaged over 5 ps to reduce noise, while the positions of the water and BPP atoms are from one single frame.

relatively long range (> 5 Å) and the screening from the water layers, the forces are generally weak. This is consistent with the experimental observation that there is no preferred orientation for the adsorbed BPP molecules on the surface.

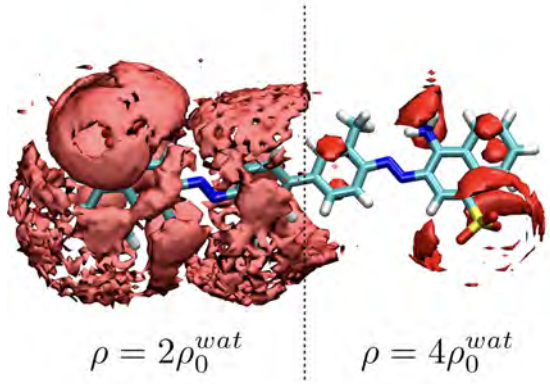

Fig. 6.6: 3D density profile of the water around a BPP molecule as obtained from a 15 ns MD simulation. The values of the iso-density surfaces shown in the figure are twice (left) and four times (right) the density of bulk water. High water density regions can be noted around the polar groups and above and below the aromatic ring (left), with one hydrogen pointing towards the center of the ring. Further away from the BPP molecule there is a cage-like structure where the water molecules rearrange to maximize the number of hydrogen bonds that they can form (right). A comparison between the radial pair distribution function of water molecules close to BPP with that of bulk water shows that on average their coordination number is reduced by 0.8. The formation of this "cage" during the solvation process of large aromatic fragments is energetically costly and is responsible for the hydrophobicity of organic dyes.

The adsorption free energy for a second BPP molecule to form a dimer on the calcite surface is also estimated by metadynamics calculations and found to be of the order of -48 kJ/mol (fig. 6.7).

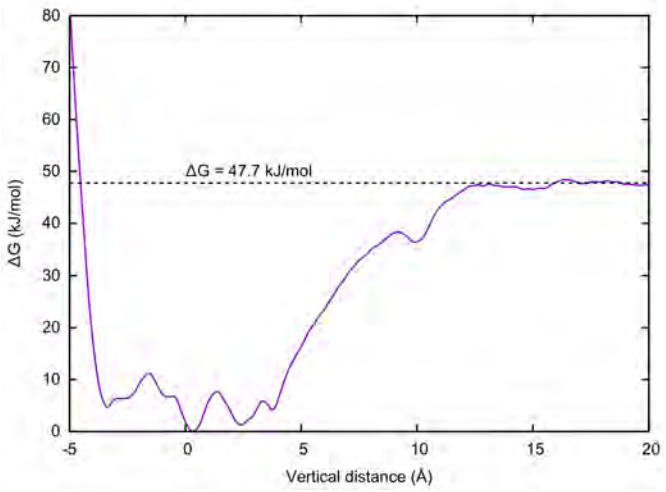

Fig. 6.7: Free energy of adsorbing a BPP molecule onto another BPP molecule restrained above the second water layer atop of calcite (10.4). The zero of free energy is set to that of the most stable bound configuration and the dashed line indicates the limit of dissociation, thereby giving the adsorption free energy.

This is larger than the pairing free energy obtained in bulk water, but because of the complexity of the calculations, we do not necessarily regard this difference as being significant since there may be convergence issues or artefacts due to the restraint that holds one BPP over the surface. Nevertheless, this confirms that the formation of BPP dimers on the surface of calcite is thermodynamically favorable.

Two possible dimer arrangements can be envisioned, one with the dimers standing sideways on the surface and one with the dimers laying parallel to the surface (fig. 6.8 a). Analysis of the atomic trajectories shows that one of the stable configurations for the adsorbed dimer has both molecules standing sideways onto the surface, which is then used to build a small island and assess its stability on the calcite surface. The small BPP island remain stable for the whole simulation ($\sim$ 20ns), though after $\sim$ 10 ns the two end molecules on one side turn to form a dimer that is aligned almost parallel to the surface (fig. 6.8 b), *i.e.*, the turned dimer represents the other dimer configuration shown in the schematics in fig. 6.8 a.

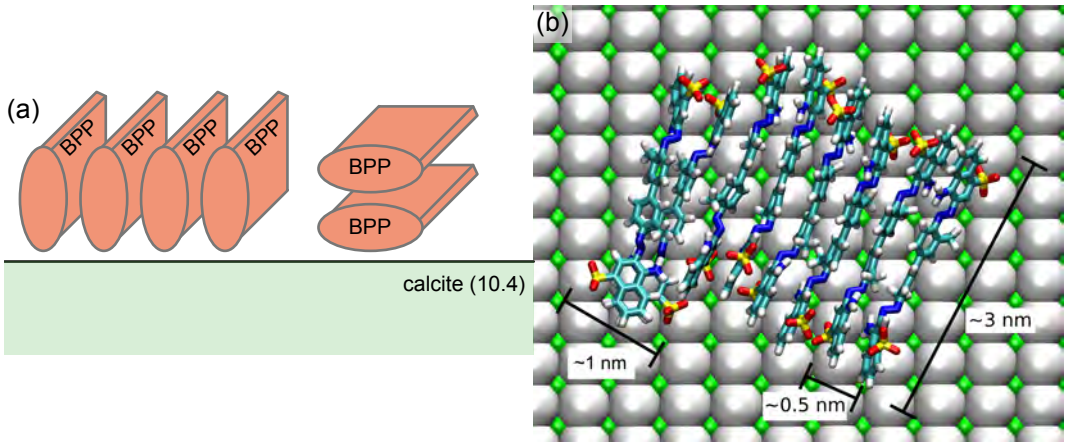

Fig. 6.8: (a) Schematic representation of the possible arrangements of the BPP molecules in the adsorbed islands. (b) Sample atomic configuration of a stack of eight BPP molecules on calcite (10.4) after $\sim$ 15 ns of MD equilibration. For clarity, the water molecules are removed and the carbonate ions of the calcite top layer are represented as large white spheres. The scale bars shown on the plot are approximate and are determined from the atomic trajectories.

It is worth noting that during the above simulations the BPP stack never comes into direct contact with the calcite surface, but remaines doubly solvent separated, as in the case of the adsorption of a single molecule or the dimer, and that the island slowly rotates during the MD run. These findings provide evidence for the fact that there is only a weak direct interaction between the calcite surface and BPP that might led to a preferred orientation. Regardless of the dimer orientation, the width of the simulated BPP stack ($\sim$ 3 nm) agrees remarkably well with the width of the stripes observed by AFM ($\sim$ 3.5 nm, fig. 5.3 d). The separation between the molecules stacked perpendicularly to the surface (0.3-0.5 nm) is consistent with the typical π-π stacking distance, this is about half an oscillation observed within the

stripe (approximately 0.8 nm, fig. 5.3 e). This factor of two could be due to specific AFM imaging conditions. For example, even for bare calcite it is known that certain tips image two surface features as a single one (so-called row pairing).[140] Thus, it is well possible that we image pairs of molecules aligned sideways. Another option is that the islands are instead formed by flat laying BPP dimers aligned next to each other. Then, the width of the dimers would be approximately 1 nm, which would then require the dimers to arrange in an overlapping manner to agree with the experimentally observed periodicity of 0.8 nm (fig. 5.3 e). Both arrangements shown in fig. 6.8 a seem to be plausible and it is difficult to obtain quantitative information regarding their relative stability, which would depend on the accuracy of the force field. The height of a BPP dimer relative to the surface is very similar to that of a BPP molecule standing sideways on the surface (from the MD trajectories, the highest atoms sits between 1 and 2 nm above the surface, defined as the z-position of the calcium ions) and therefore the apparent height observed in the AFM measurements for both these structures would be very similar. Because the apparent height in the AFM images would also depend on the structure of the water layers above the island, it is difficult to definitively rule out one arrangement or the other. Moreover, if we consider that a macroscopic BPP island carries a significant negative charge, it is likely that Na^+ ions will be intercalated between the molecules, increasing both the intermolecular separation and the stack width; an effect not considered during the simulations.

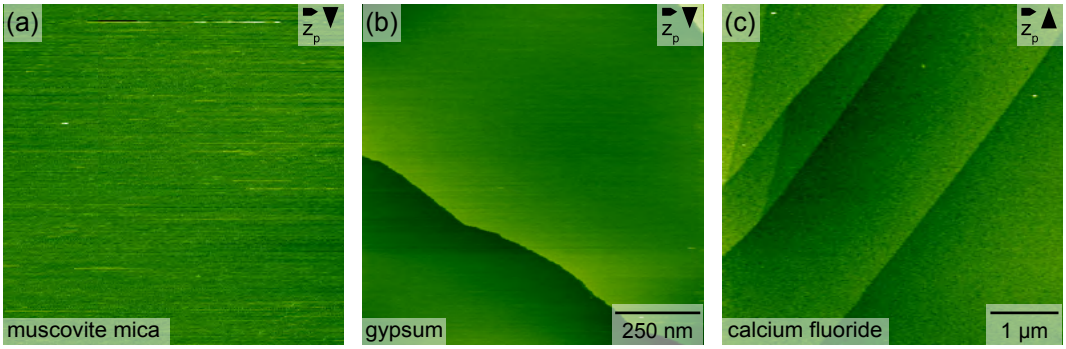

Fig. 6.9: (a) Muscovite mica (0001) surface in the presence of 83 μM BPP. (b) Gypsum ($CaSO_4 \cdot 2\,H_2O$) (020) surface in the presence of 83 μM BPP. (c) Calcium fluoride (CaF_2) (111) surface in the presence of 18 μM BPP. All *in-situ* AFM measurements are conducted at a pH of 3.5. For none of the four surfaces can any adsorption of molecular islands be observed.

The above discussion highlights the impact of the interfacial hydration structure on the self-assembly of BPP on calcite. To further verify this interpretation, we perform *in-situ* AFM measurements on three further substrates, namely muscovite mica (0001), gypsum ($CaSO_4 \cdot 2\,H_2O$) (020) and calcium fluoride (CaF_2) (111) surfaces. As can be seen in fig. 6.9, for none of these surfaces can we observe any adsorption of molecular islands when using a BPP concentration of 18-83 μM at a pH of 3.5. These results strengthen our hypothesis that the observed adsorption of BPP on

calcite is strongly related to the presence of the first two well-ordered water layers on this mineral's surface (fig. 6.3 and fig. 6.4). In particular, we argue that the key features that favor the adsorption of hydrophobic species on the hydrated calcite surface are the presence of strong hydrogen bonds between the water molecules in the second water layer and the mineral surface.

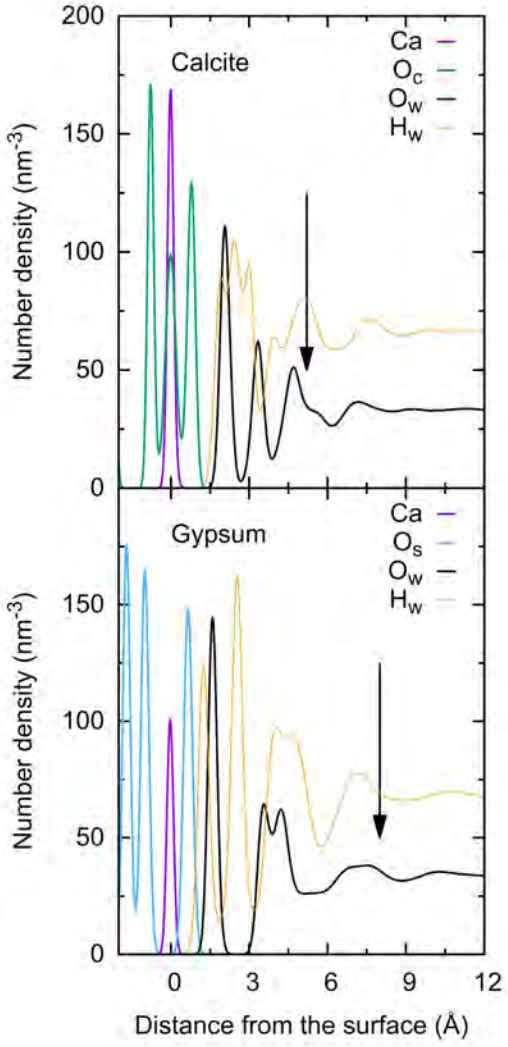

Fig. 6.10: Comparison between the 1D water density above calcite (10.4) surface (top) and the gypsum (020) surface (bottom). In both panels, the calcium, water oxygen and water hydrogen densities are shown in purple, black and orange, respectively. The carbonate and sulfate oxygens are shown in green and blue. The vertical arrows indicate the position of the adsorbed state for BPP above the mineral surface (fig. 6.11).

In the case of mica there is no clear separation between the second and third water layer,[141,142] and the presence of cations in the Stern layer, which are necessary for the local charge neutrality of the system, is probably responsible for the disruption of the hydrogen-bond network and of any lateral ordering of the hydration water. In the case of CaF_2, computer simulations of the water structure above the (111) surface[143] show that there are three well-defined water layers above the surface. Similar to calcite, the water molecules in first hydration layer are strongly localized

above the calcium ions and lay mostly flat above the surface. However, because fluoride (F^-) is not a good hydrogen bond acceptor, the water molecules in the second hydration layer are oriented differently to those on calcite and they form hydrogen bonds with the molecules in the third hydration layer.[143] This observation is consistent with the third water layer being further away from the mineral surface for CaF_2 than for calcite.

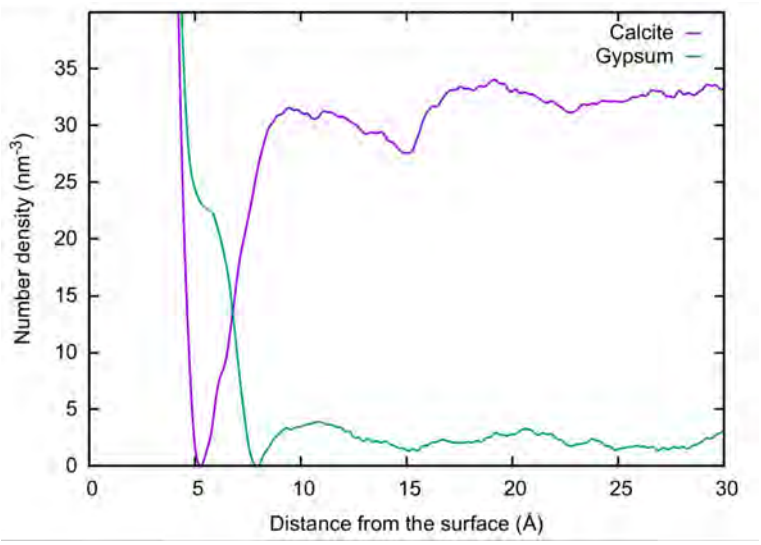

Fig. 6.11: 1D adsorption free energy as a function of the distance between the BPP center of mass and the calcite (10.4) (purple) and gypsum (020) (green) surfaces calculated using well-tempered metadynamics simulations. Unbiased 20 ns long MD simulations starting from the adsorption minima show that BPP remains adsorbed on calcite while it desorbs from gypsum, qualitatively confirming these results.

More interesting is the case of gypsum where the sulfate ($-SO_4$) groups at the surface can form hydrogen bonds with water and it is, therefore, expected to behave similarly to calcite. The 1D water density profiles above the two mineral surfaces is, however, markedly different (fig. 6.10) and, in agreement with the experimental results, metadynamics simulations predict that BPP should not adsorb on the (020) gypsum surface (fig. 6.11). Although three water layers can be clearly identified also above the (020) gypsum surface, these layers are significantly closer to the mineral surface (defined as the position of the topmost calcium layer) compared to calcite, and the second and third layers almost overlap. By analyzing the position and orientation of the water molecules above the gypsum (020) surface (fig. 6.10 and fig. 6.12) it is evident that the first hydration layer can be considered as continuation of the mineral lattice, and that, similarly to calcite, the molecules in the second layer form strong hydrogen bonds with the sulfate ions at the surface.

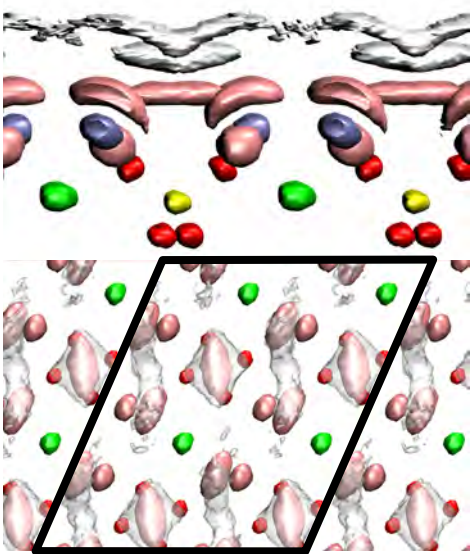

Fig. 6.12: 3D iso-density map of the top gypsum (020) surface layer and of the hydration water along the a-axis and along the c-axis. Regions of high density of calcium, sulfur and sulfate oxygens ions are shown in green, yellow and red, respectively. The oxygens of the water molecules in the first and second/third hydration layers are shown in mauve and white, while regions of high density for the hydrogens are shown in pink. For clarity, the iso-density surfaces for the oxygen atoms in the second/third hydration layer have been made transparent.

However, a detailed analysis of the geometry of the hydrogen bonds between the water and the mineral surfaces as a function of the distance from the surface reveals some interesting differences between the two minerals (fig. 6.13). A typical hydrogen bond in bulk water is characterized by an oxygen-oxygen distance of approximately 2.7 Å and by an O-H-O bond of approximately 165 degrees (fig. 6.14), and any deviations from this typical configuration would result in a weaker hydrogen bond.

It is, therefore, immediately evident that the strongest hydrogen bonds between water and the mineral surface are formed by the molecules in the second hydration layer above the calcite (10.4) surface and those in the first hydration layer above the gypsum (020) surface, while there are virtually no hydrogen bonds between calcite and its first hydration layer and between gypsum and its second hydration layer. The third hydration layer also forms very weak hydrogen bonds with both minerals due to its larger distance from the surfaces.

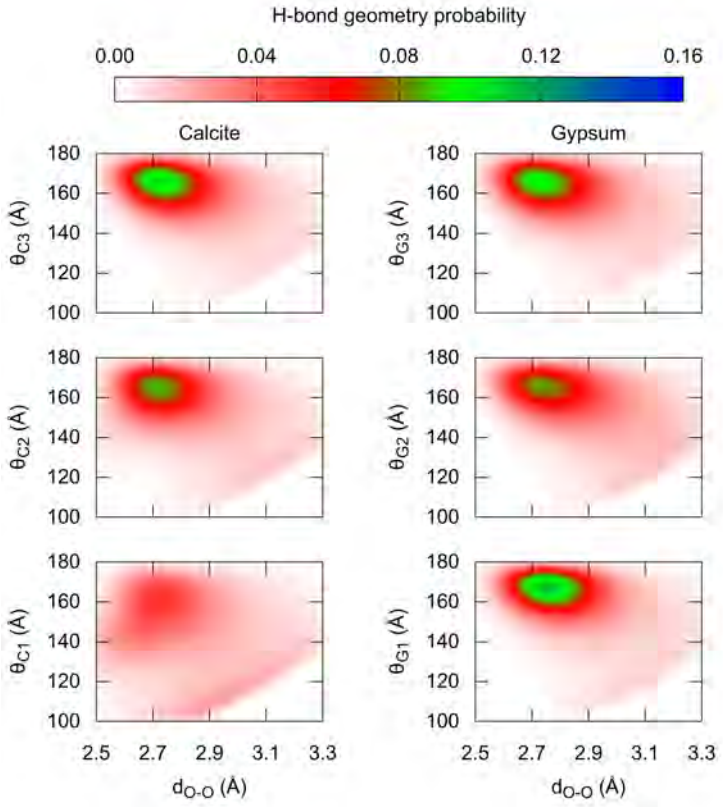

Fig. 6.13: 2D probability maps for finding two oxygen atoms at a distance d_{O-O} and with a O-H-O angle θ for the water molecules in the first (bottom panels), second (middle panels) or third hydration layer (top panels) above calcite (10.4) (left panels) or gypsum (020) (right panels). These probabilities have been calculated by considering only water/carbonate pairs.

This observation supports our hypothesis that the second water layer above calcite has a strong lateral ordering due to the interaction with the mineral and it is, therefore, an optimal place for BPP due to the lower entropic cost associated with locating a hydrophobic adsorbent on top of the second layer rather than in the bulk solution. On the other hand, the second hydration layer above the gypsum (020) surface forms very weak hydrogen bonds with the mineral, hence it has a smaller lateral ordering and it can be viewed as more "bulk-like". Therefore, there is no entropic gain for BPP to leave the bulk solution and adsorb on gypsum. From this comparison, we can conclude that the specific hydration layer structure is critical for the adsorption of organic molecules at the interface. Interestingly, even seemingly similar surfaces such as calcite (10.4) and gypsum (020) can greatly vary in their interaction with hydrophobic molecules due to details of their hydration structure.

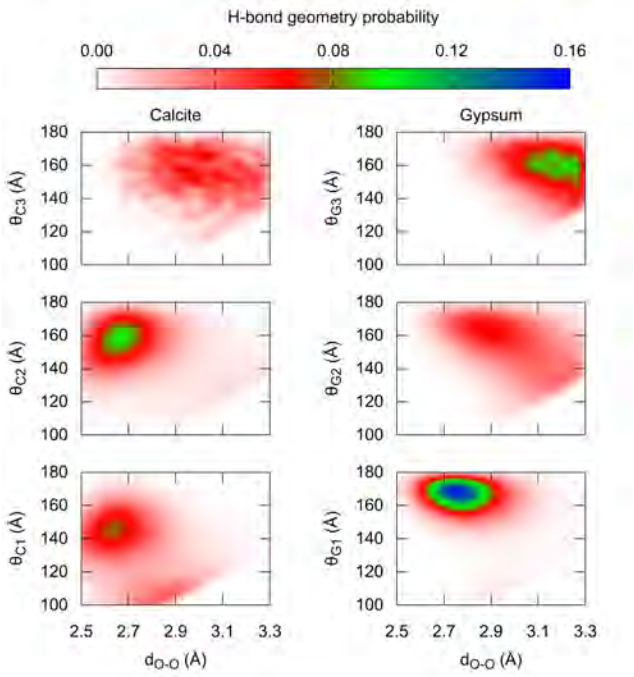

Fig. 6.14: 2D probability maps for finding two oxygen atoms at a distance d_{O-O} and with a O-H-O angle θ for the water molecules in the first (bottom panels), second (middle panels) or third hydration layer (top panels) above calcite (10.4) (left panels) or gypsum (020) (right panels). The hydrogen bond geometry in the third water layer (top) panel is practically indistinguishable from that of bulk water. These probabilities have been calculated by considering all oxygen/oxygen pairs.

6.3 Summary and Conclusion - Benzopurpurine

Using *in-situ* high-resolution dynamic AFM and MD calculations we study the adsorption of BPP at the calcite (10.4)-water interface. BPP forms well-ordered molecular islands that appear not to be commensurate with respect to the underlying substrate lattice. The islands exhibit a characteristic inner structure with lateral periodicities of about 3.5 and 0.8 nm. From MD simulations and free energy calculations, we find that BPP does not bind to the calcite surface directly but instead adopts a position above the second hydration layer. This unexpected adsorption position can be understood by the fact that the water structure is least disturbed by the molecule when positioned in the most hydrophobic region, which is atop the second hydration layer. This finding rationalizes why the experimentally observed islands are not commensurate with the underlying calcite lattice, which in turn supports the finding of the simulations. We corroborate this finding by comparing the results obtained on calcite (10.4) with other mineral surfaces that exhibit different interfacial hydration structures and show that the formation of the island-like structures of BPP seems to be highly selective for the calcite (10.4) surface, despite the lack of direct interaction, because of the unique structure of its mineral-water interface.

Part IV

Calcite Nucleation and Growth

7

Influence of Initial pH on Calcite Nucleation and Growth

Abstract

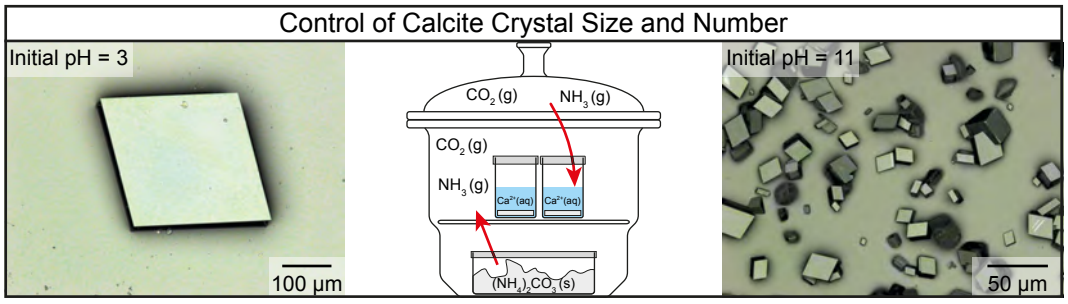

The ammonia diffusion method is a widely used approach for investigating the impact of additive molecules on calcium carbonate nucleation and growth. In the absence of additives, rhombohedral calcite crystals form. To elucidate the effect of various additives on crystallite number, size and morphology, an extensively used strategy is comparing the results of crystallization in the presence and absence of these additives. Here, we explore the impact of changing the starting pH value of the solution on the resulting calcite crystal number and size using the ammonia diffusion method in the absence of additives. Our work demonstrates that few but large crystals are obtained at low initial pH, while many but small crystals form at high initial pH. We discuss our results in the view of the classical LaMer theory for nucleation and growth. The revealed pH-dependence of the particle number is compared to what is expected when using a simplified picture assuming, among others, a constant addition rate. However, in the ammonia diffusion method the situation is far more complex, making a precise description of the effect of the pH on the interplay of the involved rates extremely challenging. Our work demonstrates that care has to be taken when assigning the particle number to a specific effect of the additive as the particle number is also a function of the pH and, thus, might be only indirectly related to the presence of the additive.

7.1 Introduction - Ammonia Diffusion Method

Calcite, the most stable polymorph of calcium carbonate ($CaCO_3$), plays a pivotal role in many natural but also technological fields, including, *e.g.*, geochemistry,[3] biomineralization,[20,21] as well as scale inhibition and sea water desalination.[144] In most of these fields, the properties of calcite are significantly modified by the presence of organic additives.[14] For example, the outstanding properties of biominerals are controlled by the presence of organic additives that are capable of greatly altering the crystallization process, resulting in highly sophisticated, tailor-made crystal morphologies. While great effort has been made to elucidate the role of additives in nucleation and growth, the detailed mode of action of many additives still remains unclear.[14]

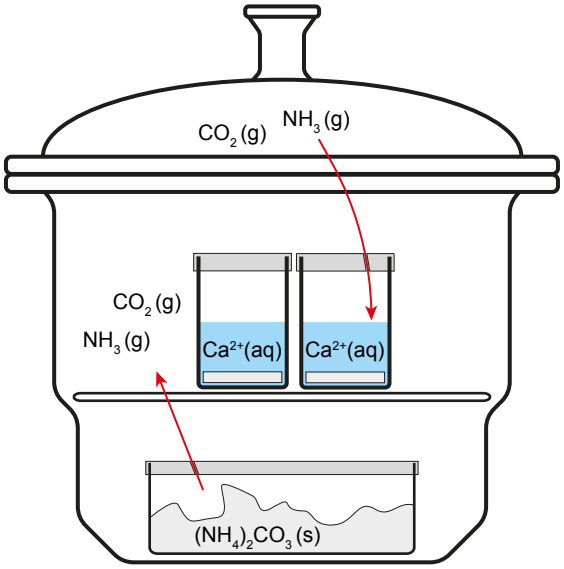

Fig. 7.1: Schematics illustrating the ammonia diffusion method setup for controlled calcium carbonate precipitation. Ammonium carbonate decomposes at room temperature and ammonia and carbon dioxide diffuse into the solutions containing calcium chloride. For a solution with an initial pH smaller than 9.5, the ammonia addition increases the pH value of the solution and, thus, shifts the carbonate equilibrium towards the carbonate side. As a result, the carbonate concentration is increased, which results in precipitation of calcium carbonate.

To shed light on the impact of added molecules on the crystallization of calcium carbonate, the ammonia diffusion method (ADM) has been widely used,[15,76,145–147] as this approach allows for a straightforward assessment of the influence of dissolved molecules during well-controlled calcium carbonate precipitation. In brief, this method is based on the diffusion of both carbon dioxide (CO_2) and ammonia (NH_3) into a solution containing calcium chloride ($CaCl_2$). This is realized by thermal decomposition of ammonium carbonate ($(NH_4)_2CO_3$) in a desiccator, which also contains the calcium solution(s) (fig. 7.1). The diffusion of CO_2 into the solution increases the carbonate concentration due to the carbon dioxide-bicarbonate-

carbonate equilibrium. When starting with a pH value lower than 9.5, the addition of NH_3 increases the pH of the solution, until a final pH of 9.5 is reached.[148] The increase in pH shifts the carbonate equilibrium to higher carbonate ratios/contents, which in the presence of calcium ions precipitates as calcium carbonate. The corresponding equations are given as follows.

$$(NH_4)_2CO_3(s) \xrightarrow{\Delta} 2\,NH_3(g) + CO_2(g) + H_2O(g) \tag{7.1}$$

$$NH_3(g) \rightleftharpoons NH_3(aq) \tag{7.2}$$

$$CO_2(g) \rightleftharpoons CO_2(aq) \tag{7.3}$$

$$NH_3(aq) + H_2O \rightleftharpoons {NH_4}^+(aq) + OH^-(aq) \tag{7.4}$$

$$CO_2(aq) + H_2O \rightleftharpoons H_2CO_3(aq) \tag{7.5}$$

$$H_2CO_3(aq) + H_2O \rightleftharpoons {HCO_3}^-(aq) + H_3O^+(aq) \tag{7.6}$$

$${HCO_3}^-(aq) + H_2O \rightleftharpoons {CO_3}^{2-}(aq) + H_3O^+(aq) \tag{7.7}$$

$${Ca}^{2+}(aq) + {CO_3}^{2-}(aq) \rightleftharpoons CaCO_3(s) \tag{7.8}$$

In the absence of additive molecules, rhombohedral crystals form, indicating the formation of calcite, the thermodynamically stable modification of calcium carbonate. In the presence of additive molecules in the solution, this crystallization process can be altered significantly, and the resulting particle's size, shape and crystal structure provides valuable information on the mechanisms governing the additive-controlled crystallization process.[147] Of course, as the pH shifts the carbonate equilibrium, it impacts the formation of calcite crystals. Thus, added molecules can influence the calcium carbonate precipitation both in a direct way, *e.g.*, by preferential adsorption onto certain crystal planes, and in an indirect way, namely by changing the pH of the

solution. Therefore, it is mandatory to study the impact of changing the pH value of the solution separately from the effect of additives to arrive at a correct description of both direct and indirect influences. Here, we perform calcium carbonate precipitation using the ammonia diffusion method in the absence of additives. To evaluate the impact of the initial pH value of the calcium chloride solution, we study different starting pH values. While few but large crystals are obtained at low starting pH value, many but small crystals are formed at high starting pH value. This result is discussed in the view of the classical LaMer theory for homogeneous nucleation and growth. The obtained pH-dependence of the particle number is compared to what is expected when using a simplified model based on several assumptions including, *e.g.*, a constant addition rate. However, as the pH affects the complex interplay of the carbonate addition and, therefore, the particle nucleation and growth rates, a precise prediction of particle number and size is not straightforward. Despite this, we show that the crystal number and size can be controlled by tuning the initial pH of the solution.

7.2 Instrumentation - Ammonia Diffusion Method

Thoroughly cleaned and freshly rinsed beakers are filled with 5 ml of diluted calcium chloride solution (5 mM, stock solution volumetric grade from Sigma Aldrich with a concentration of 500 mM) using pure water (18 MΩ·cm). The pH value of these solutions is adjusted using NaOH (0.1 M, volumetric standard solution, Carl Roth) and HCl (0.1 M, volumetric standard solution, Carl Roth) to obtain starting pH values of 3, 7 and 11, respectively. A glass slide for optical microscopy is placed at the bottom in each of the three beakers, then the beakers are placed in a desiccator, which also contained a Petri dish with 5 g ammonium carbonate (ACS reagent, Sigma Aldrich). The desiccator is kept at a temperature of 22-24°C. Twenty-four hours after placing the beakers in the desiccator, the glass slides are removed from the beakers, rinsed with pure water and acetone (ACS reagent, reag. ISO, reag. Ph. Eur., Sigma Aldrich), dried in a nitrogen flow and inspected with a laser scanning microscope (VK-8710 Color 3D Laser Microscope from Keyence). For each sample, several areas on the glass slide are evaluated to obtain a representative view. The reproducibility is ensured by repeating the experiment three times.

The glass slides for optical microscopy are cleaned prior to each experiment in an ultrasonic bath using EtOH (absolute, reag. ISO, reag. Ph. Eur., ≥99.8%, Sigma Aldrich), HCl (0.1 M, volumetric standard solution, Carl Roth) and NaOH (0.1 M, volumetric standard solution, Carl Roth), for 15 minutes each. Between each cleaning step and also in the end glass slides are rinsed with pure water and finally dried in a nitrogen flow. The clean glass slides are placed at the bottom of the beakers and filled with the calcium chloride solution. Then the pH is adjusted using

NaOH and HCl and after sealing placed in the desiccator. The beakers, as well as the Petri dish are covered with sealing film (Parafilm, Neenah). The sealing film of the beakers is punctured with three holes, the sealing film of Petri dish with one hole.

7.3 Results and Discussion

Particle number and size as a function of the pH value. To evaluate the impact of the starting pH value on the number and size of calcite crystals precipitated using the ammonia diffusion method in the absence of additives, we prepare solutions with different starting pH values. Twenty-four hours after starting the precipitation experiment, the glass slides are removed from the beakers and the obtained particle size and number on the slide are evaluated using light microscopy. A representative overview is given in fig. 7.2. While few but large crystals are found at a low starting pH of 3, many but small crystals are obtained at a starting pH of 11. At an initial pH of 7, an intermediate number of medium-sized crystals are obtained. After 24 hours, the final pH is measured to be 9.5, regardless of the initial conditions.

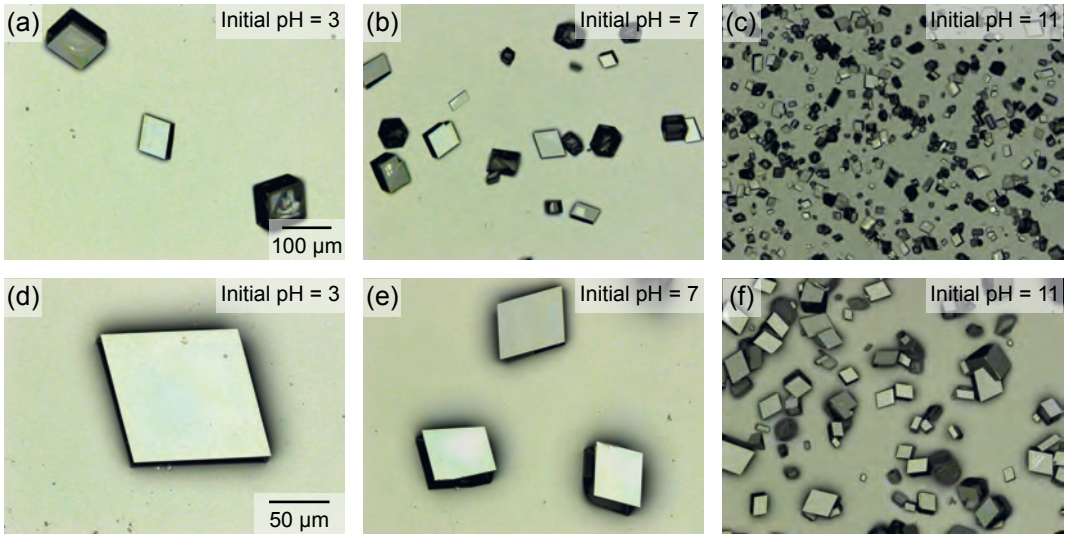

Fig. 7.2: Light microscopy images taken 24 hours after starting the precipitation experiment. Depending on the starting pH value either few but large crystals (initial pH 3, left column) or many but small crystals (initial pH 11, right column) are obtained. For an initial pH of 7 (middle column), an intermediate number of medium-sized particles are formed.

Principle of the ADM. To understand the pH-dependent crystal number and size, we analyze the processes occurring during the ammonia diffusion method. Due to thermal decomposition of the ammonium carbonate, ammonia and carbon dioxide are formed. Both gases diffuse into the solutions and dissolve partially. For an initial pH lower than 9.5, the dissolved ammonia causes the pH of the solution to rise until a final pH of 9.5 is reached.[148] For a pH larger than 9.5, the pH drops initially until a constant pH of 9.5 is reached. Dissolved carbon dioxide transforms partially into carbonate. The respective fraction of carbon dioxide, bicarbonate and

carbonate is given by the carbonate equilibrium, which is pH-dependent. For low pH values, the majority of carbon exists as dissolved carbon dioxide, while only little bicarbonate and even less carbonate is present. For high pH, the situation is opposite with the majority of carbon being present in the form of carbonate, while only little bicarbonate and even less dissolved carbon dioxide is present (fig. 7.3). This equilibrium is characterized by the pK_a values 6.35 (same amount of carbon dioxide and bicarbonate) and 10.33 (same amount of bicarbonate and carbonate).[149,150] Thus, the carbonate concentration in the ADM is defined by two different processes, namely the continuous addition of dissolved carbon dioxide and the changing pH value.

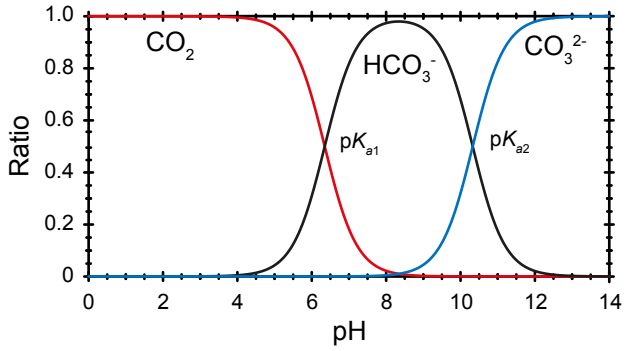

Fig. 7.3: Carbonate equilibrium showing the respective fraction of carbon dioxide, bicarbonate and carbonate at a given pH.

Upon starting the experiment with a solution having a low pH, the carbonate concentration increases only marginally due to fact that the carbonate equilibrium dictates that virtually no carbonate is present until a pH of about 8.5 is reached.[151] Further increasing the pH, however, results in a drastic increase in the carbonate concentration. When a steady pH of 9.5 is reached, the formation rate is only controlled by the diffusion of CO_2 into the solution. In contrast, starting the experiment with a pH larger than 9.5, the pH decreases in the course of the experiment. In this case, comparing starting situations with the same concentration of dissolved CO_2, the carbonate formation rate is higher in the beginning and decreases due to the pH-dependent decrease in carbonate fraction. When the final pH is reached, the same diffusion-controlled formation rate is obtained as in the case for low starting pH. Notably, in both cases, the carbonate addition rate is not constant in the ADM.

Carbonate equilibrium species distribution calculation. In aqueous solutions the concentration of carbonic acid is very low and the equilibrium described in eq. (7.5) is shifted towards the dissolved CO_2. The widely accepted combination of the equilibrium eq. (7.5) and eq. (7.6) leads to eq. (7.9), representing the first deprotonation step for carbonic acid.

$$\mathrm{CO_2(aq) + 2\,H_2O(aq) \rightleftharpoons HCO_3^-(aq) + H_3O^+(aq)} \tag{7.9}$$

$$\mathrm{HCO_3^-(aq) + H_2O(aq) \rightleftharpoons CO_3^{2-}(aq) + H_3O^+(aq)} \tag{7.10}$$

For each protonation / deprotonation step, the acid dissociation constant (K_{ai}) is defined by the quotient of the respective equilibrium concentrations.

$$K_{a1} = \frac{c(\mathrm{H_3O^+}) \cdot c(\mathrm{HCO_3^-})}{c(\mathrm{CO_2})} \tag{7.11}$$

$$K_{a2} = \frac{c(\mathrm{H_3O^+}) \cdot c(\mathrm{CO_3^{2-}})}{c(\mathrm{HCO_3^-})} \tag{7.12}$$

For carbonic acid the two acid dissociation constants are given as follows.[149,150]

Tab. 7.1: Acid dissociation constants for the two protonation / deprotonation step of carbonic acid.[149,150]

Molecule	K_{a1} [mol l^{-1}]	K_{a1} [mol l^{-1}]
H_2CO_3	4.45×10^{-7}	4.84×10^{-11}

Calculation of the carbonate equilibrium species distribution is performed using the relevant protonation / deprotonation equilibrium equations for an *n*-protic acid ($H_{n-i+1}A^{(i-1)-}$).[89]

$$H_{n-i+1}A^{(i-1)-}(aq) + \mathrm{H_2O} \rightleftharpoons H_{n-i}A^{i-}(aq) + \mathrm{H_3O^+}(aq) \tag{7.13}$$

The total concentration (C) for carbonate is the sum over all protonated / deprotonated species being present in the solution at every pH.

$$C = \sum_{i=0}^{n} c\left(H_{n-i}A^{i-}(aq)\right) \tag{7.14}$$

Numerical analysis of the resulting system of linear equations enables the precise determination of the equilibrium concentration of all protonated / deprotonated species at a given pH.

$$c\left(H_{n-i+1}A^{(i-1)-}\right) = \frac{c^{n-1}(\mathrm{H_3O^+}) \cdot C(H_nA) \cdot \prod_{j=1}^{i} K_{Sj}}{\sum_{r=0}^{n}\left[c^{n-r}(\mathrm{H_3O^+}) \cdot \prod_{j=1}^{r} K_{Sj}\right]} \tag{7.15}$$

For the carbonate equilibrium in the crystallization reaction the total concentration of carbonate is unknown. However the calculation of the species distribution is possible because fig. 7.3 illustrates the ratio of the protonated / deprotonated species. The ratio is only given by the actual pH of the solution and, therefore, equal for any arbitrary value of *C*.

LaMer theory for nucleation and growth. Regardless of the details in carbonate formation, the situation in an ADM experiment can be described by a gradual addition of carbonate to a calcium containing solution. Consequently, at a certain concentration of carbonate, the precipitation of calcium carbonate sets in. Particle nucleation and growth upon gradual addition of one component A to a solution containing a fix concentration of another component B can be described by the theory introduced by LaMer and Dinegar in 1950.[152] In this description, the saturation *S* is monitored as a function of time. For a binary system as calcium carbonate the saturation is given by:

$$S = \frac{[A] \cdot [B]}{K_{SP}} \tag{7.16}$$

with [A] and [B] being the concentrations of carbonate and calcium, respectively. The constant K_{SP} is the solubility product of the compound AB. In the course of the experiment, the saturation depends on the interplay of three rates, namely the addition rate, R_A (which is considered to be constant in the simplest case), as well as the particle nucleation and growth rate, R_N and R_G, respectively. Using classical, homogeneous nucleation theory, an expression for the nucleation and the radius growth rates can be given as follows:[153]

$$R_N = \frac{dN}{dt} = A \cdot exp\left[\frac{-16\pi\gamma^3 V_m^2}{3k_B^3 T^3 N_A^2 (lnS)^2}\right] \tag{7.17}$$

$$R_G = \frac{dr}{dt} = V_m \cdot D \cdot C^0_{flat} \cdot \frac{S - exp\left(\frac{2\gamma V_m}{rN_A k_B T}\right)}{r + \frac{D}{k_g^{flat}} \cdot exp\left(\alpha \frac{2\gamma V_m}{rN_A k_B T}\right)} \tag{7.18}$$

with *N*, *A*, γ, V_m, *T*, k_B, N_A and α being the particle number, the pre-exponential factor, the bulk surface energy, the molar volume, the temperature, the Boltzmann constant, the Avogadro number and the transfer coefficient for growth. Moreover, *D*, C^0_{flat}, and k_g^{flat} are the diffusion coefficient, the solubility of the bulk material (*i.e.*, $\sqrt{K_{SP}}$) and the rate constant for growth of a flat ($r = \infty$) surface, respectively.[153] Note that both rates depend on the saturation, while the growth rate additionally depends on the particle radius.

The complex interplay between addition, nucleation and growth rates results in the classical "LaMer curve" that is shown schematically in fig. 7.4.[152,154] In regime I, the concentration of component A increases linearly due to a constant addition of component A to the system containing a known concentration of component B. Accordingly, the saturation *S* raises linearly, which is often displayed instead of the concentration of component A. As can be seen in fig. 7.4, the linear increase continues even after a saturation of S=1 is reached.

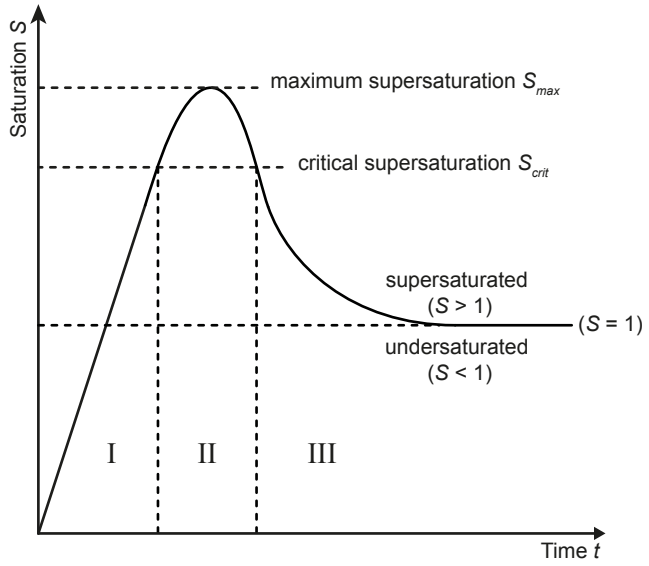

Fig. 7.4: Typical shape of a "LaMer curve".[152] Upon constant addition of one component to another, the saturation linearly increases in regime I, until particle nucleation and growth results in a deviation from this linear increase in regime II. At the point of maximum saturation, the sum of nucleation and growth rates of all stable particles compensates the addition rate. After the maximum saturation, the sum of nucleation and growth rates overcompensate the addition rate, causing the saturation to drop. In regime III, the existing particles grow in size, no new stable particles are formed.

Now, the system is supersaturated. Only after a critical saturation, S_{crit}, is reached, particle nucleation is stable, resulting in a deviation from a linear increase in the saturation, as a certain amount of AB is precipitated. Note that particle nucleation occurs in the entire range of regime I, however, the associated growth rates are negative, *i.e.*, the nuclei that form in regime I have a very high probability to dissociate immediately after formation. When the critical saturation, S_{crit}, is passed, the system enters into regime II. Here, the growth rates become positive, thus, the nucleating particles now possess a very high probability to remain stable. At the maximum saturation, S_{max}, the sum of the nucleation and the growth rates of all stable particles compensate the addition rate, *i.e.*, the derivative of the saturation with respect to the time equals zero. Then, the increasing number of stable particles with increasing size causes the sum of nucleation rate and growth rates to overcompensate the addition rate, *i.e.*, the saturation decreases again.[2] When the critical saturation is reached again, regime III is entered. This regime is characterized by the growth of the existing particles. No new particles are formed, as the growth rates of newly formed particles are, again, negative. Thus, in regime III, the decrease in saturation is exclusively due to particle growth. As long as the saturation is larger than 1, the sum of the growth rates of all stable particles is larger than the addition rate. When a saturation of S=1 is reached, the system enters into a dynamic equilibrium, which is defined by the saturation concentration of AB, $\sqrt{K_{SP}}$, *i.e.*, an amount equivalent to the added A is incorporated in the existing particles. Therefore, the growth rate exactly compensates the addition rate and the curve has a zero slope.

Discussion of the pH dependence of the particle number and size. We now discuss the experimentally obtained pH-dependence of the particle number using the assumptions made by T. Sugimoto.[155] Using these assumptions, the final particle number N_∞ is a simple function of the addition rate, the molar volume and the mean volume growth rate ν and given as follows:

$$N_\infty = \frac{R_A \cdot V_m}{\dot{\nu}} \tag{7.19}$$

This equation is based on the assumptions that the addition rate is constant, and the number of final particles can be estimated by only considering the nucleation close to the maximum of the LaMer curve. The latter assumption results in far-reaching simplifications, including a constant saturation during nucleation, the same radius for a stable nuclei and, consequently, the same volume growth rate for all stable particles. Assuming the volume growth rate being the same in both, the acidic and alkaline case, the final particle number only depends on the addition rate. As

[2] We note that the nucleation rate decreases as the saturation decreases, thus, the fact that the sum of nucleation and growth rates overcompensates the addition rate is caused by the increasing number of stable particles.

the addition rate is larger in the alkaline case as compared to the acidic case, it follows that the final particle number should be larger for alkaline starting condition. However, even so this conclusion nicely describes the observed results, this could be by coincidence only. As already pointed out by T. Sugimoto,[155] the volume growth rate can be influenced by the addition rate. In this case, the simple linear dependence of the final particle number on the addition rate is no longer valid. For a comprehensive description, the saturation-dependence of the nucleation and growth rates as stated in eq. (7.17) and eq. (7.18) has to be considered explicitly within the entire regime II. Due to their interdependence this can be a challenging task. The observed size difference is most likely a consequence of the final particle number assuming that roughly the same amount of carbonate is distributed among the existing particles. If only few particles are present after nucleation has finished, these particles will, therefore, grow larger as compared to a situation with many particles present. Therefore, the different size of the crystals is most likely a consequence of the different number of particles present after regime II.

7.4 Summary and Conclusion

The impact of different starting pH values on the calcite crystal number and size using the ammonia diffusion method is discussed. We show that the particle number is increased for alkaline as compared to acidic starting conditions. The particles remain smaller in the case of alkaline starting condition. We discuss nucleation and growth rates from classical LaMer theory to elucidate the mechanism behind the different number of final particles. The obtained difference in final particle number is considered using a commonly applied simplified picture that is based on several assumptions. In this model, the final particle number is a linear function of the addition rate solely. Although our results are well described by this model, the made assumptions are not necessarily valid. We argue that disentangling the effect of the pH on nucleation and growth rates as well as nucleation time is challenging, illustrating the complex interplay of the involved rates in the ammonia diffusion method. Despite these challenges, our results unambiguously show that the crystal size can be controlled by tuning the initial pH value. This has to be considered when using the ammonia diffusion method to assess the effect of additive molecules on calcite.

Part V

Summary

8 Summary

This thesis presents a detailed characterization of the calcite (10.4)-water interface in the presence of organic molecules. Using *in-situ* high-resolution dynamic AFM, I particularly focus on the impact of organophosphonates and organic azo dyes on two different dynamic interfacial processes: calcite (10.4) dissolution and surface restructuring, as well as the adsorption and molecular self-assembly of the molecules on step edges and terraces of the calcite (10.4) substrate.

Understanding dissolution and surface restructuring processes is highly relevant for geochemical and industrial processes, such as: scale inhibition and corrosion protection. Systematically varying the size and the number of functional end groups, I study the effect of six different organophosphonate molecules, three tetraphosphonates and three diphosphonates, on the dissolution process of the calcite (10.4) surface in chapter 3. Independent of the pH, a very pronounced restructuring of the calcite (10.4) surface is observed for each molecule, resulting in the formation of characteristically shaped etch pits (olive-shaped for the tetraphosphonates and triangular-shaped for the diphosphonates). As I observe the very same resulting surface morphology within each group, I conclude that the process of surface restructuring is only affected by the presence of one amino-*bis*(methylenephosphonate) end group and neither by the protonation and deprotonation state, nor by the size of the molecules. This observation points towards a general property of organophosphonate molecules to alter and restructure the (10.4) surface of calcite during dissolution.

The interplay of surface restructuring and molecular self-assembly is of tremendous importance for biomineralization processes and demonstrated for five different Eriochrome azo dyes in chapter 4. Irrespective of the specific dye structure and independent of the pH, all five dye molecules induce a characteristic surface restructuring during calcite (10.4) dissolution. The restructuring of the surface appears to be the result of the adsorption of the molecules to specific step edges, favoring both non-polar, acute step edges ($[4\bar{4}\bar{1}]$ and $[48\bar{1}]$) and the polar step edge along the [010] direction. In contrast, the formation of self-assembled molecular rows along the $[42\bar{1}]$ direction on calcite (10.4) terraces is observed for one Eriochrome azo dye exclusively and furthermore limited to a very narrow pH range around 3.6. The results indicate that the surface restructuring mechanism seems to be very robust, whereas molecular self-assembly requires a more rigorous control of molecular structure, conformation and protonation and deprotonation state.

Nevertheless, the precise control of molecular self-assembly at mineral-water interfaces is extremely challenging due to the complex interplay of molecule-molecule, molecule-surface, molecule-water, surface-water and water-water interactions. For the first time, in chapter 5, I demonstrate three possibilities to control systematically the adsorption of the organic azo dye BPP and its subsequent self-assembly into highly ordered molecular islands on the calcite (10.4) surface. Varying the molecule concentration, the pH and the concentration of calcium ions in the solution, allows for steering the coverage of BPP molecules adsorbed onto calcite (10.4), as well as the timescale of the molecule adsorption and island growth process.

The hydration structure above the calcite (10.4) surface plays a decisive role for the adsorption behavior of organic molecules and their self-assembly into ordered molecular structures. In chapter 6, MD simulations of BPP at the calcite (10.4)-water interface reveal that the molecule adsorbs at the interface, but not as expected, directly on calcite (10.4). Instead, the molecule adsorbs onto the second hydration layer, approximately 5 Å above the substrate surface. This somewhat surprising adsorption position can be understood by the fact that the unique water structure above calcite (10.4) creates a hydrophobic region in which the molecule causes the least disturbance of the ordered water structure at the interface. Transferring this finding and comparing it with the hydration structure of other minerals provides fundamental insights into the interactions of organic molecules at mineral–water interfaces, particularly for adsorption and structure formation phenomena.

The last chapter, chapter 7, is a study of the pH dependency of calcite nucleation and growth by using the ammonia diffusion method. Systematically varying the initial pH of the crystallization solution shows the possibility to directly steer the resulting calcite crystal number and size. Few but large calcite crystals are obtained at low initial pH, whereas many but small calcite crystals result from high initial pH. The results a critically discussed in the view of the classical LaMer theory for homogeneous nucleation and growth.

In summary, this thesis provides high-resolution insights into dissolution, surface restructuring and molecular self-assembly at the calcite (10.4)-water interface in the presence of organic molecules. Furthermore, it highlights that when aiming for a rational understanding, modelling and predicting of interfacial processes, a molecular-scale knowledge of the composition of the entire interface is essential. This includes the mineral surface, the hydration structure, as well as the behavior of the additive molecules in solution and at the interface.

Bibliography

[1] A. Lüttge, R. S. Arvidson, "The Mineral-Water Interface" in *Kinetics of Water-Rock Interaction*, (Eds.: S. L. Brantley *et al.*), Springer New York, New York, NY, **2008**, pp. 73–107.

[2] G. E. Brown, "How Minerals React with Water", *Science* **2001**, *294*, 67–69.

[3] G. E. Brown, G. Calas, "Mineral-Aqueous Solution Interfaces and Their Impact on the Environment", *Geochem. Perspect.* **2012**, 483–742.

[4] C. V. Putnis, E. Ruiz-Agudo, "The Mineral-Water Interface: Where Minerals React with the Environment", *Elements* **2013**, *9*, 177–182.

[5] A. Putnis, "Why Mineral Interfaces Matter", *Science* **2014**, *343*, 1441–1442.

[6] J. R. Reeder, *Carbonates: Mineralogy and Chemistry*, Mineralogical Society of America, **1983**.

[7] W. A. Deer, R. A. Howie, J. Zussman, *An Introduction to the Rock-Forming Minerals*, Mineralogical Society of Great Britain and Ireland, **1992**.

[8] H. A. Lowenstam, "Minerals formed by organisms", *Science* **1981**, *211*, 1126–1131.

[9] F. Heberling *et al.*, "Reactivity of the calcite-water interface, from molecular scale processes to geochemical engineering", *Appl. Geochem.* **2014**, *45*, 158–190.

[10] F. C. Meldrum, H. Cölfen, "Controlling mineral morphologies and structures in biological and synthetic systems", *Chem. Rev.* **2008**, *108*, 4332–4432.

[11] M. D. Hollingsworth, "Calcite Biocomposites Up Close", *Science* **2009**, *326*, 1194–1195.

[12] J. Rieger, M. Kellermeier, L. Nicoleau, "Formation of Nanoparticles and Nanostructures-An Industrial Perspective on $CaCO_3$, Cement, and Polymers", *Angew. Chem. Int. Ed.* **2014**, *53*, 12380–12396.

[13] S. Mann *et al.*, "Crystallization at inorganic-organic interfaces: Biominerals and biomimetic synthesis", *Science* **1993**, *261*, 1286–1292.

[14] R.-Q. Song, H. Cölfen, "Additive controlled crystallization", *CrystEngComm* **2011**, *13*, 1249–1276.

[15] M. Schreiber *et al.*, "How deprotonation changes molecular self-assembly - an AFM study in liquid environment", *Soft Matter* **2013**, *9*, 7145–7149.

[16] E. Ruiz-Agudo, C. V. Putnis, A. Putnis, "Coupled dissolution and precipitation at mineral-fluid interfaces", *Chem. Geol.* **2014**, *383*, 132–146.

[17] R. Momper *et al.*, "Stabilization of Polar Step Edges on Calcite (10.4) by the Adsorption of Congo Red", *Langmuir* **2015**, *31*, 7283–7287.

[18] M. Ricci *et al.*, "Growth and Dissolution of Calcite in the Presence of Adsorbed Stearic Acid", *Langmuir* **2015**, *31*, 7563–7571.

[19] M. Nalbach *et al.*, "Molecular Self-Assembly Versus Surface Restructuring During Calcite Dissolution", *Langmuir* **2016**, *32*, 9975–9981.

[20] F. C. Meldrum, "Calcium carbonate in biomineralisation and biomimetic chemistry", *Int. Mater. Rev.* **2003**, *48*, 187–224.

[21] F. Nudelman, Sommerdijk, Nico A. J. M., "Biomineralization as an Inspiration for Materials Chemistry", *Angew. Chem. Int. Ed.* **2012**, *51*, 6582–6596.

[22] A. N. Kofina, K. D. Demadis, P. G. Koutsoukos, "The Effect of Citrate and Phosphocitrate On Struvite Spontaneous Precipitation", *Cryst. Growth Des.* **2007**, *7*, 2705–2712.

[23] K. D. Demadis, Z. Anagnostou, H. Zhao, "Novel Calcium Carboxyphosphonate / polycarboxylate Inorganic-Organic Hybrid Materials from Demineralization of Calcitic Biomineral Surfaces", *ACS Appl. Mater. Interfaces* **2009**, *1*, 35–38.

[24] H. Ehrlich *et al.*, "Principles of demineralization: Modern strategies for the isolation of organic frameworks. Part II. Decalcification", *Micron* **2009**, *40*, 169–193.

[25] J. H. Harding *et al.*, "Computational Techniques at the Organic−Inorganic Interface in Biomineralization", *Chem. Rev.* **2008**, *108*, 4823–4854.

[26] C. T. Hendley *et al.*, "Microscopy techniques for investigating the control of organic constituents on biomineralization", *MRS Bull.* **2015**, *40*, 480–489.

[27] H. Diehl, J. Ellingbee, "Azo Dyes as Indicators for Calcium and Magnesium", *Anal. Chem.* **1960**, *32*, 1120–1123.

[28] K. D. Demadis, P. Baran, "Chemistry of organophosphonate scale growth inhibitors: Two-dimensional, layered polymeric networks in the structure of tetrasodium 2-hydroxyethyl-amino-*bis*(methylenephosphonate)", *J. Solid State Chem.* **2004**, *177*, 4768–4776.

[29] J. Jupille, "Analysis of Mineral Surfaces by Atomic Force Microscopy", *Reviews in Mineralogy and Geochemistry* **2014**, *78*, 331–369.

[30] G. Binnig, C. F. Quate, C. Gerber, "Atomic Force Microscope", *Phys. Rev. Lett.* **1986**, *56*, 930–933.

[31] G. Meyer, N. M. Amer, "Novel optical approach to atomic force microscopy", *Appl. Phys. Lett.* **1988**, *53*, 2400–2402.

[32] R. García, R. Pérez, "Dynamic atomic force microscopy methods", *Surf. Sci. Rep.* **2002**, *47*, 197–301.

[33] H. Söngen, R. Bechstein, A. Kühnle, "Quantitative atomic force microscopy", *J. Phys.: Condens. Matter* **2017**, *29*, 274001.

[34] T. Fukuma *et al.*, "True atomic resolution in liquid by frequency-modulation atomic force microscopy", *Appl. Phys. Lett.* **2005**, *87*, 34101.

[35] T. Fukuma *et al.*, "True molecular resolution in liquid by frequency-modulation atomic force microscopy", *Appl. Phys. Lett.* **2005**, *86*, 193108.

[36] T. R. Albrecht *et al.*, "Frequency modulation detection using high-Q cantilevers for enhanced force microscope sensitivity", *J. Appl. Phys.* **1991**, *69*, 668–673.

[37] S. Rode *et al.*, "Modification of a commercial atomic force microscopy for low-noise, high-resolution frequency-modulation imaging in liquid environment", *Rev. Sci. Instrum.* **2011**, *82*, 073703.

[38] H. Adam *et al.*, "Photothermal excitation setup for a modified commercial atomic force microscope", *Rev. Sci. Instrum.* **2014**, *85*, 023703.

[39] T. E. Schäffer *et al.*, "Studies of vibrating atomic force microscope cantilevers in liquid", *J. Appl. Phys.* **1996**, *80*, 3622–3627.

[40] S. Kuhn *et al.*, "Identifying the absolute orientation of a low-symmetry surface in real space", *Phys. Rev. B* **2014**, *90*, 904.

[41] A. O. Harstad, S. L. S. Stipp, "Calcite dissolution: Effects of trace cations naturally present in Iceland spar calcites", *Geochim. Cosmochim. Acta* **2007**, *71*, 56–70.

[42] M. Nalbach *et al.*, "Structure-Dependent Dissolution and Restructuring of Calcite Surfaces by Organophosphonates", *Cryst. Growth Des.* **2017**, *just accepted manuscript*.

[43] R. Murugavel *et al.*, "Metal Complexes of Organophosphate Esters and Open-Framework Metal Phosphates: Synthesis, Structure, Transformations, and Applications", *Chem. Rev.* **2008**, *108*, 3549–3655.

[44] J. A. Dean, *Lange's handbook of chemistry and physics*, McGraw Hill Inc., New York, 15th edition, **1999**.

[45] K. D. Demadis, "Chemistry of Organophosphonate Scale Inhibitors, Part 4: Stability of Amino-*tris*-(Methylene Phosphonate) Towards Degradation by Oxidizing Biocides", *Phosphorus Sulfur Silicon Relat. Elem.* **2006**, *181*, 167–176.

[46] K. D. Demadis, N. Stavgianoudaki, "Chapter 14: Structural Diversity in Metal Phosphonate Frameworks: Impact on Applications" in *Metal Phosphonate Chemistry: From Synthesis to Applications*, The Royal Society of Chemistry, **2012**, pp. 438–492.

[47] L. Wang *et al.*, "Visualizing Organophosphate Precipitation at the Calcite–Water Interface by in Situ Atomic-Force Microscopy", *Environ. Sci. Technol.* **2016**, *50*, 259–268.

[48] E. Ruiz-Agudo *et al.*, "Interactions between Organophosphonate-Bearing Solutions and (1014) Calcite Surfaces: An Atomic Force Microscopy and First-Principles Molecular Dynamics Study", *Cryst. Growth Des.* **2010**, *10*, 3022–3035.

[49] W. El Malti *et al.*, "Surface modification of calcium carbonate with phosphonic acids", *J. Mater. Chem.* **2012**, *22*, 1212–1218.

[50] E. Akyol *et al.*, "Systematic Structural Determinants of the Effects of Tetraphosphonates on Gypsum Crystallization", *Cryst. Growth Des.* **2009**, *9*, 5145–5154.

[51] E. Barouda *et al.*, "Barium Sulfate Crystallization in the Presence of Variable Chain Length Aminomethylenetetraphosphonates and Cations (Na^+ or Zn^{2+})", *Cryst. Growth Des.* **2007**, *7*, 321–327.

[52] L. Wang *et al*., "Imaging Organophosphate and Pyrophosphate Sequestration on Brucite by in Situ Atomic Force Microscopy", *Environ. Sci. Technol.* **2017**, *51*, 328–336.

[53] C. A. Orme *et al*., "Formation of chiral morphologies through selective binding of amino acids to calcite surface steps", *Nature* **2001**, *411*, 775–779.

[54] H. Cölfen, M. Antonietti, "Mesocrystals: Inorganic Superstructures Made by Highly Parallel Crystallization and Controlled Alignment", *Angew. Chem. Int. Ed.* **2005**, *44*, 5576–5591.

[55] L. Sonnenberg *et al*., "Quantitative Single Molecule Measurements on the Interaction Forces of Poly(l-glutamic acid) with Calcite Crystals", *J. Am. Chem. Soc.* **2007**, *129*, 15364–15371.

[56] A. S. Schenk *et al*., "Hierarchical Calcite Crystals with Occlusions of a Simple Polyelectrolyte Mimic Complex Biomineral Structures", *Adv. Funct. Mater* **2012**, *22*, 4668–4676.

[57] K. K. Sand *et al*., "Biomineralization: Long-Term Effectiveness of Polysaccharides on the Growth and Dissolution of Calcite", *Cryst. Growth Des.* **2014**, *14*, 5486–5494.

[58] A. Hellal, S. Chafaa, N. Chafai, "Synthesis, characterization and computational studies of three α-amino-phosphonic acids derivatives from Meta, Ortho and Para aminophenol", *J. Mol. Struct.* **2016**, *1103*, 110–124.

[59] K. Moedritzer, R. R. Irani, "The Direct Synthesis of α-Aminomethylphosphonic Acids. Mannich-Type Reactions with Orthophosphorous Acid", *J. Org. Chem.* **1966**, *31*, 1603–1607.

[60] M. F. Mady, M. A. Kelland, "Overview of the Synthesis of Salts of Organophosphonic Acids and Their Application to the Management of Oilfield Scale", *Energy Fuels* **2017**, *31*, 4603–4615.

[61] Y. Liang, D. R. Baer, A. S. Lea, "Dissolution of $CaCO_3$ (1014) Surface", *Mater. Res. Soc. Symp. Proc.* **1994**, *355*, 409–414.

[62] N.-S. Park *et al*., "Tribological Enhancement of $CaCO_3$ Dissolution during Scanning Force Microscopy", *Langmuir* **1996**, *12*, 4599–4604.

[63] D. W. Britt, V. Hlady, "In-Situ Atomic Force Microscope Imaging of Calcite Etch Pit Morphology Changes in Undersaturated and 1-Hydroxyethylidene-1,1-diphosphonic Acid Poisoned Solutions", *Langmuir* **1997**, *13*, 1873–1876.

[64] T. Ichikawa, K. Sawada, "Structure and NMR Behavior of Cobalt(III) Polyamine Complexes of α,ω-Alkylenediamine-*N,N,N'N'*-tetramethylenetetraphosphonate in Aqueous Solution", *Bull. Chem. Soc. Jpn.* **1997**, *70*, 2111–2123.

[65] K. Popov, H. Rönkkömäki, L. H. J. Lajunen, "Critical evaluation of stability constants of phosphonic acids (IUPAC Technical Report)", *Pure Appl. Chem.* **2001**, *73*, 1641–1677.

[66] E. Ruiz-Agudo, C. Rodriguez-Navarro, E. Sebastián-Pardo, "Sodium Sulfate Crystallization in the Presence of Phosphonates: Implications in Ornamental Stone Conservation", *Cryst. Growth Des.* **2006**, *6*, 1575–1583.

[67] A.-W. Xu, Y. Ma, H. Cölfen, "Biomimetic mineralization", *J. Mater. Chem.* **2007**, *17*, 415–449.

[68] H. Cölfen, "Biomineralization: A crystal-clear view", *Nat. Mater.* **2010**, *9*, 960–961.

[69] J. Rieger *et al.*, "Precursor structures in the crystallization/precipitation processes of $CaCO_3$ and control of particle formation by polyelectrolytes", *Faraday Discuss.* **2007**, *136*, 265–277.

[70] S. L. S. Stipp, C. M. Eggleston, B. S. Nielsen, "Calcite Surface-Structure Observed at Microtopographic and Molecular Scales with Atomic-Force Microscopy (AFM)", *Geochim. Cosmochim. Acta* **1994**, *58*, 3023–3033.

[71] R. Kristensen, S. L. S. Stipp, K. Refson, "Modeling steps and kinks on the surface of calcite", *J. Chem. Phys.* **2004**, *121*, 8511–8523.

[72] S. Rode *et al.*, "True Atomic-Resolution Imaging of (1014) Calcite in Aqueous Solution by Frequency Modulation Atomic Force Microscopy", *Langmuir* **2009**, *25*, 2850–2853.

[73] K. Henriksen, S. L. S. Stipp, "Controlling Biomineralization: The Effect of Solution Composition on Coccolith Polysaccharide Functionality", *Cryst. Growth Des.* **2009**, *9*, 2088–2097.

[74] K. K. Sand *et al.*, "Binding of ethanol on calcite: the role of the OH bond and its relevance to biomineralization", *Langmuir* **2010**, *26*, 15239–15247.

[75] I. S. Pasarin *et al.*, "Atomic modifications by synchrotron radiation at the calcite-ethanol interface", *J. Synchrotron Rad.* **2012**, *19*, 530–535.

[76] M. Dietzsch *et al.*, "PAA-PAMPS Copolymers as an Efficient Tool to Control $CaCO_3$ Scale Formation", *Langmuir* **2013**, *29*, 3080–3088.

[77] C. Marutschke *et al.*, "Three-dimensional hydration layer mapping on the (10.4) surface of calcite using amplitude modulation atomic force microscopy", *Nanotechnology* **2014**, *25*, 335703.

[78] V. Nelea *et al.*, "Effects of Full-Length Phosphorylated Osteopontin and Constituent Acidic Peptides and Amino Acids on Calcite Dissolution", *Cryst. Growth Des.* **2014**, *14*, 979–987.

[79] A. S. Schenk *et al.*, "Systematic Study of the Effects of Polyamines on Calcium Carbonate Precipitation", *Chem. Mater.* **2014**, *26*, 2703–2711.

[80] K. Rae Cho *et al.*, "Direct observation of mineral-organic composite formation reveals occlusion mechanism", *Nat. Commun.* **2016**, *7*.

[81] S. Hofmann *et al.*, "Visualising the molecular alteration of the calcite (104)-water interface by sodium nitrate", *Sci. Rep.* **2016**, *6*, 21576.

[82] T. Fukuma *et al.*, "Atomic-Scale Distribution of Water Molecules at the Mica-Water Interface Visualized by Three-Dimensional Scanning Force Microscopy", *Phys. Rev. Lett.* **2010**, *104*, 016101.

[83] H. Imada, K. Kimura, H. Onishi, "Water and 2-Propanol Structured on Calcite (104) Probed by Frequency-Modulation Atomic Force Microscopy", *Langmuir* **2013**, *29*, 10744–10751.

[84] P. Fenter *et al.*, "Is the Calcite–Water Interface Understood? Direct Comparisons of Molecular Dynamics Simulations with Specular X-ray Reflectivity Data", *J. Phys. Chem. C* **2013**, *117*, 5028–5042.

[85] G. Schwarzenbach, W. Biedermann, “Komplexone X. Erdalkalikomplexe von o, o’-Dioxyazofarbstoffen”, *Helv. Chim. Acta* **1948**, *31*, 678–687.

[86] G. Schwarzenbach, W. Biedermann, “Die komplexometrische Titration der Erdalkalien und einiger anderer Metalle mit Eriochromschwarz T”, *Chimia* **1948**, *2*, 56–59.

[87] M. S. Masoud, H. H. Hammud, H. Beidas, “Dissociation constants of eriochrome black T and eriochrome blue black R indicators and the formation constants of their complexes with Fe(III), Co(II), Ni(II), Cu(II), Zn(II), Cd(II), Hg(II), and Pb(II), under different temperatures and in presence of different solvents”, *Thermochim. Acta* **2002**, *381*, 119–131.

[88] H.-R. Sagaster, G. Röbisch, A. Mehlhorn, “Untersuchungen zur Tautomerie von o,o’-Dihydroxy-azofarbstoffen der Eriochrom-Reihe”, *J. Prakt. Chem.* **1987**, *329*, 1045–1051.

[89] C. Bliefert, *pH-Wert-Berechnungen*, Verlag Chemie, Weinheim New York, **1978**.

[90] M. Nalbach *et al.*, “Where is the Most Hydrophobic Region? Benzopurpurine Self-Assembly at the Calcite-Water Interface”, *J. Phys. Chem. C* **2017**, *just accepted manuscript*.

[91] G. M. Whitesides, J. P. Mathias, C. T. Seto, “Molecular Self-Assembly and Nanochemistry: A Chemical Strategy for the Synthesis of Nanostructures”, *Science* **1991**, *254*, 1312–1319.

[92] J. V. Barth, “Molecular Architectonic on Metal Surfaces”, *Annu. Rev. Phys. Chem.* **2007**, *58*, 375–407.

[93] F. Rosei *et al.*, “Organic Molecules Acting as Templates on Metal Surfaces”, *Science* **2002**, *296*, 328–331.

[94] S. M. Barlow, R. Raval, “Complex organic molecules at metal surfaces: Bonding, organisation and chirality”, *Surf. Sci. Rep.* **2003**, *50*, 201–341.

[95] J. V. Barth, G. Costantini, K. Kern, “Engineering atomic and molecular nanostructures at surfaces”, *Nature* **2005**, *437*, 671–679.

[96] T. Glatzel *et al.*, “Molecular assemblies grown between metallic contacts on insulating surfaces”, *Appl. Phys. Lett.* **2009**, *94*, 063303.

[97] C. M. Hauke *et al.*, “Controlling Molecular Self-Assembly on an Insulating Surface by Rationally Designing an Efficient Anchor Functionality That Maintains Structural Flexibility”, *ACS Nano* **2013**, *7*, 5491–5498.

[98] P. Rahe *et al.*, “Tuning molecular self-assembly on bulk insulator surfaces by anchoring of the organic building blocks”, *Adv. Mater.* **2013**, *25*, 3948–3956.

[99] J. C. Love *et al.*, “Self-Assembled Monolayers of Thiolates on Metals as a Form of Nanotechnology”, *Chem. Rev.* **2005**, *105*, 1103–1170.

[100] C. L. McGuiness *et al.*, “Molecular Self-Assembly at Bare Semiconductor Surfaces: Preparation and Characterization of Highly Organized Octadecanethiolate Monolayers on GaAs(001)”, *J. Am. Chem. Soc.* **2006**, *128*, 5231–5243.

[101] M. Lackinger *et al.*, “Self-Assembly of Trimesic Acid at the Liquid−Solid Interface - a Study of Solvent-Induced Polymorphism”, *Langmuir* **2005**, *21*, 4984–4988.

[102] I. Destoop *et al.*, "Solvent-Induced Homochirality in Surface-Confined Low-Density Nanoporous Molecular Networks", *J. Am. Chem. Soc.* **2012**, *134*, 19568–19571.

[103] T. Sirtl *et al.*, "Solvent-Dependent Stabilization of Metastable Monolayer Polymorphs at the Liquid–Solid Interface", *ACS Nano* **2013**, *7*, 6711–6718.

[104] K. Tahara *et al.*, "Formation of Multicomponent Star Structures at the Liquid/Solid Interface", *Langmuir* **2015**, *31*, 7032–7040.

[105] A. Della Pia *et al.*, "Molecular self-assembly of substituted terephthalic acids at the liquid/solid interface: Investigating the effect of solvent", *Faraday Discuss.* **2017**, –.

[106] R. Otero *et al.*, "Molecular Self-Assembly at Solid Surfaces", *Adv. Mater.* **2011**, *23*, 5148–5176.

[107] T. Hiasa, K. Kimura, H. Onishi, "Cross-Sectional Structure of Liquid 1-Decanol over Graphite", *J. Phys. Chem. C* **2012**, *116*, 26475–26479.

[108] J. J. De Yoreo, S. Chung, R. W. Friddle, "In Situ Atomic Force Microscopy as a Tool for Investigating Interactions and Assembly Dynamics in Biomolecular and Biomineral Systems", *Adv. Funct. Mater* **2013**, *23*, 2525–2538.

[109] K. Suzuki *et al.*, "Atomic-Resolution Imaging of Graphite–Water Interface by Frequency Modulation Atomic Force Microscopy", *Appl. Phys. Express* **2011**, *4*, 125102.

[110] A. Labuda *et al.*, "Monotonic damping in nanoscopic hydration experiments", *Phys. Rev. Lett.* **2013**, *110*, 066102.

[111] T. Fukuma *et al.*, "Mechanism of atomic force microscopy imaging of three-dimensional hydration structures at a solid-liquid interface", *Phys. Rev. B* **2015**, *92*, 155412.

[112] D. Martin-Jimenez *et al.*, "Atomically resolved three-dimensional structures of electrolyte aqueous solutions near a solid surface", *Nat. Commun.* **2016**, *7*, 12164.

[113] H. Söngen *et al.*, "Chemical Identification at the Solid-Liquid Interface", *Langmuir* **2017**, *33*, 125–129.

[114] P. Geissbühler *et al.*, "Three-dimensional structure of the calcite–water interface by surface X-ray scattering", *Surf. Sci.* **2004**, *573*, 191–203.

[115] F. Heberling *et al.*, "Structure and reactivity of the calcite-water interface", *J. Colloid Interface Sci.* **2011**, *354*, 843–857.

[116] C. Robinson, H. A. T. Mills, "The Colloid Chemistry of Dyes: The Aqueous Solutions of Benzopurpurine 4B and Its Isomer Prepared from m-Tolidine. Part I", *Proc. R. Soc. London Ser. A* **1931**, *131*, 576–595.

[117] C. B. McKitterick *et al.*, "Aggregation Properties of the Chromonic Liquid Crystal Benzopurpurin 4B", *J. Phys. Chem. B* **2010**, *114*, 1888–1896.

[118] D. Nečas, P. Klapetek, "Gwyddion: an open-source software for SPM data analysis", *Cent. Eur. J. Phys.* **2012**, *10*, 181–188.

[119] A. Hantzsch, "Blaue und rote Kongofarbstoffsäure; ein Beitrag zur Theorie der Indicatoren", *Ber. Dtsch. Chem. Ges.* **1915**, *48*, 158–167.

[120] E. Pigorsch, A. Elhaddaoui, S. Turrell, "Spectroscopic study of pH and solvent effects on the structure of Congo red and its binding mechanism to amyloid-like proteins", *Spectrochim. Acta Part A* **1994**, *50*, 2145–2152.

[121] M. A. Rauf, S. Hisaindee, N. Saleh, "Spectroscopic studies of keto-enol tautomeric equilibrium of azo dyes", *RSC Adv.* **2015**, *5*, 18097–18110.

[122] S. Plimpton, "Fast Parallel Algorithms for Short-Range Molecular Dynamics", *J. Comput. Phys.* **1995**, *117*, 1–19.

[123] G. A. Tribello *et al.*, "PLUMED 2: New feathers for an old bird", *Comput. Phys. Commun.* **2014**, *185*, 604–613.

[124] J. Wang *et al.*, "Development and Testing of a General Amber Force Field", *J. Comput. Chem.* **2004**, *25*, 1157–1174.

[125] P. Raiteri, R. Demichelis, J. D. Gale, "Thermodynamically Consistent Force Field for Molecular Dynamics Simulations of Alkaline-Earth Carbonates and Their Aqueous Speciation", *J. Phys. Chem. C* **2015**, *119*, 24447–24458.

[126] M. Kellermeier *et al.*, "Entropy Drives Calcium Carbonate Ion Association", **2016**, *17*, 3535–3541.

[127] M. De La Pierre *et al.*, "Uncovering the Atomistic Mechanism for Calcite Step Growth", *Angew. Chem. Int. Ed.* **2017**, *56*, 1–5.

[128] E. H. Byrne, P. Raiteri, J. D. Gale, "Computational Inisghts into the Calicum-Sulfate Ion Pair Formation", **2017**.

[129] Y. Wu, H. L. Tepper, G. A. Voth, "Flexible simple point-charge water model with improved liquid-state properties", *J. Chem. Phys.* **2006**, *124*, 024503.

[130] A. Laio, M. Parrinello, "Escaping free-energy minima", *Proc. Natl. Acad. Sci. U.S.A.* **2002**, *99*, 12562–12566.

[131] P. Raiteri *et al.*, "Efficient Reconstruction of Complex Free Energy Landscapes by Multiple Walkers Metadynamics", *J. Phys. Chem. B* **2006**, *110*, 3533–3539.

[132] A. Barducci, G. Bussi, M. Parrinello, "Well-Tempered Metadynamics: A Smoothly Converging and Tunable Free-Energy Method", *Phys. Rev. Lett.* **2008**, *100*, 020603.

[133] H.-S. Park *et al.*, "Self-Assembly of Lyotropic Chromonic Liquid Crystal Sunset Yellow and Effects of Ionic Additives", *J. Phys. Chem. B* **2008**, *112*, 16307–16319.

[134] A. J. Dickinson *et al.*, "Aggregate Structure and Free Energy Changes in Chromonic Liquid Crystals", *Mol. Cryst. Liq. Cryst.* **2009**, *509*, 9/[751]–20/[762].

[135] T. Ostapenko *et al.*, "Aggregation, pretransitional behavior, and optical properties in the isotropic phase of lyotropic chromonic liquid crystals studied in high magnetic fields", *Soft Matter* **2013**, *9*, 9487–9498.

[136] D. M. Agra-Kooijman *et al.*, "Columnar molecular aggregation in the aqueous solutions of disodium cromoglycate", **2014**, *89*, 062504.

[137] W. Xiao *et al.*, "Structural Correspondence of Solution, Liquid Crystal, and Crystalline Phases of the Chromonic Mesogen Sunset Yellow", *Cryst. Growth Des.* **2014**, *14*, 4166–4176.

[138] F. C. MacKintosh, S. A. Safran, P. A. Pincus, "Self-Assembly of Linear Aggregates: The Effect of Electrostatics on Growth.", *Europhys. Lett.* **1990**, *12*, 697.

[139] P. Raiteri *et al.*, "Derivation of an Accurate Force-Field for Simulating the Growth of Calcium Carbonate from Aqueous Solution: A New Model for the Calcite-Water Interface", *J. Phys. Chem. C* **2010**, *114*, 5997–6010.

[140] P. Rahe, J. Schütte, A. Kühnle, "NC-AFM contrast formation on the calcite (1014) surface", *J. Phys.: Condens. Matter* **2012**, *24*, 084006.

[141] L. Cheng *et al.*, "Molecular-Scale Density Oscillations in Water Adjacent to a Mica Surface", *Phys. Rev. Lett.* **2001**, *87*, 156103.

[142] J. Wang *et al.*, "Structure, Energetics, and Dynamics of Water Adsorbed on the Muscovite (001) Surface: A Molecular Dynamics Simulation", *J. Phys. Chem. B* **2005**, *109*, 15893–15905.

[143] B. Reischl, M. Watkins, A. S. Foster, "Free Energy Approaches for Modeling Atomic Force Microscopy in Liquids", *J. Chem. Theory Comput.* **2013**, *9*, 600–608.

[144] J. Rieger, J. Thieme, C. Schmidt, "Study of Precipitation Reactions by X-ray Microscopy: $CaCO_3$ Precipitation and the Effect of Polycarboxylates", *Langmuir* **2000**, *16*, 8300–8305.

[145] L. Addadi, S. Weiner, "Interactions between acidic proteins and crystals: stereochemical requirements in biomineralization", *Proc. Natl. Acad. Sci. U.S.A.* **1985**, *82*, 4110–4114.

[146] L. Addadi *et al.*, "A chemical model for the cooperation of sulfates and carboxylates in calcite crystal nucleation: Relevance to biomineralization", *Proc. Natl. Acad. Sci. U.S.A.* **1987**, *84*, 2732–2736.

[147] C. Beato *et al.*, "Calcium carbonate crystallization in tailored constrained environments", *CrystEngComm* **2015**, *17*, 5953–5961.

[148] N. Gehrke *et al.*, "Superstructures of Calcium Carbonate Crystals by Oriented Attachment", *Cryst. Growth Des.* **2005**, *5*, 1317–1319.

[149] J. Curry, C. L. Hazelton, "The First Thermodynamic Ionization Constant of Deuteriocarbonic Acid at 25°", *J. Am. Chem. Soc.* **1938**, *60*, 2773–2776.

[150] H. S. Harned, S. R. Scholes Jr., "The Ionization Constant of HCO_3^- from 0 to 50°", *J. Am. Chem. Soc.* **1941**, *63*, 1706–1709.

[151] J. Ihli *et al.*, "Elucidating Mechanisms of Diffusion-Based Calcium Carbonate Synthesis Leads to Controlled Mesocrystal Formation", *Adv. Funct. Mater* **2013**, *23*, 1965–1973.

[152] V. K. LaMer, R. H. Dinegar, "Theory, Production and Mechanism of Formation of Monodispersed Hydrosols", *J. Am. Chem. Soc.* **1950**, *72*, 4847–4854.

[153] D. V. Talapin *et al.*, "Evolution of an Ensemble of Nanoparticles in a Colloidal Solution: Theoretical Study", *J. Phys. Chem. B* **2001**, *105*, 12278–12285.

[154] Y. Wang *et al.*, "Thermodynamics versus kinetics in nanosynthesis", *Angew. Chem. Int. Ed.* **2014**, *54*, 2022–2051.

[155] T. Sugimoto, *Monodispersed Particles*, Amsterdam London New York Oxford Paris Shannon Tokyo, **2001**.

List of Figures

2.1 Schematic FM-AFM setup 11
2.2 Experimental *in-situ* AFM setup 12
2.3 AFM liquid cells 13
2.4 Thermal noise cantilever spectrum 13
2.5 Calcite crystal sample holder 14

3.1 Model of tetraphosphonates, diphosphonates and calcite (10.4) 21
3.2 Calcite (10.4) dissolution in the presence of organophosphonates . . . 24
3.3 Calcite (10.4) etch pit geometries in the presence and absence of organophosphonates 26
3.4 EDTMP-C_2-T protonation / deprotonation sequence 27
3.5 EABMP-C_2-D protonation / deprotonation sequence 28
3.6 Calcite (10.4) surface restructuring in the presence of organophosphonates 29

4.1 Model of EBT, EBA and calcite (10.4) 35
4.2 Calcite (10.4) dissolution in the presence of EBT 36
4.3 Large-scale restructured calcite (10.4) surface in the presence of EBT . 37
4.4 Calcite (10.4) step edge models in the presence and absence of EBT . . 38
4.5 Calcite (10.4) step edge termination in the presence of EBT 39
4.6 EBT species distribution and protonation / deprotonation sequence . . 40
4.7 EBA species distribution 41
4.8 EBT azo-hydrazo tautomerization sequence 42
4.9 Calcite (10.4) surface restructuring in the presence of EBT 42
4.10 Molecular stripe formation on calcite (10.4) in the presence of EBA . . 43
4.11 Interactions at the calcite (10.4)-water interface in the presence of organic molecules 44

5.1 Model of BPP and calcite (10.4) 48
5.2 Molecular adsorption of BPP on calcite (10.4) 50
5.3 Molecular island formation on calcite (10.4) in the presence of BPP . . 51
5.4 Coverage of BPP on calcite (10.4) as a function of the BPP concentration 52
5.5 BPP protonation / deprotonation and tautomerization sequence 54
5.6 pH dependent molecule adsorption and island growth 55
5.7 System state diagram for BPP on calcite (10.4) 57

6.1 Pairing free energy between two BPP molecules in solution 62
6.2 BPP dimer configurations in solution 63
6.3 Free energy plot of BPP on calcite (10.4) and calcite density profiles . . 64
6.4 Atomic configuration of BPP on calcite (10.4) I 65
6.5 Atomic configuration of BPP on calcite (10.4) II 65
6.6 3D density profile of water around a BPP molecule 66
6.7 Free energy plot of a BPP dimer on calcite (10.4) 66
6.8 Molecular adsorption of BPP dimers on calcite (10.4) 67
6.9 BPP on muscovite mica, gypsum and calcium fluoride 68
6.10 Calcite (10.4) and gypsum (020) 3D density profiles 69
6.11 Free energy plot of BPP on calcite (10.4) and gypsum (020) 70
6.12 3D iso-density map of the gypsum (020) surface and the hydration water 71
6.13 2D probability maps for water above calcite (10.4) and gypsum (020) I 72
6.14 2D probability maps for water above calcite (10.4) and gypsum (020) II 73

7.1 Schematic ammonia diffusion method setup 78
7.2 pH-dependent calcite crystal growth 81
7.3 Carbonate species distribution 82
7.4 LaMer curve for nucleation and growth 85

List of Tables

3.1 Names and abbreviations of the organophosphonate molecules 22

4.1 Acid dissociation constants for EBT and EBA 41

7.1 Acid dissociation constants for carbonic acid 83

List of Abbreviations

AFM	Atomic force microscopy
AFM	Atomic force microscope
FM	Frequency modulation
AM	Amplitude modulation
MD	Molecular dynamics
UHV	Ultra high vacuum
EBT	Eriochrome Black T
EBA	Eriochrome Black A
EBBB	Eriochrome Blue Black B
EBBR	Eriochrome Blue Black R
ERB	Eriochrome Red B
BPP	Benzopurpurine 4B
CR	Congo Red

EDTMP-C_2-T Ethylenediamine-*tetrakis*(methylenephosphonic acid)

HDTMP-C_6-T Hexamethylenediamine-*tetrakis*(methylenephosphonic acid)

DDTMP-C_{12}-T Dodecamethylenediamine-*tetrakis*(methylenephosphonic acid

EABMP-C_2-D Ethylamine-*bis*(methylenephosphonic acid)

HABMP-C_6-D *n*-Hexamethylamine-*bis*(methylenephosphonic acid)

DABMP-C_{12}-D *n*-Dodecamethylamine-*bis*(methylenephosphonic acid)

Publications & Contributions

Publications I have (co)-authored

- **Where is the Most Hydrophobic Region? Benzopurpurine Self-Assembly at the Calcite-Water Interface**
  M. Nalbach, P. Raiteri, S. Klassen, S. Schäfer, J. D. Gale, R. Bechstein, A. Kühnle
  Journal of Physical Chemistry C **2017**, *accepted*

- **Structure-Dependent Dissolution and Restructuring of Calcite Surfaces by Organophosphonates**
  M. Nalbach, A. Moschona, K. D. Demadis, S. Klassen, R. Bechstein, A. Kühnle
  Crystal Growth & Design **2017**, *accepted*

- **High Strength Reversible Adhesive Closures**
  D. R. King, M. D. Bartlett, **M. Nalbach**, D. J. Irschick, A. J. Crosby
  Journal of Polymer Science, Part B: Polymer Physics **2017**, *accepted*

- **Molecular Self-Assembly Versus Surface Restructuring During Calcite Dissolution**
  M. Nalbach, S. Klassen, R. Bechstein, A. Kühnle
  Langmuir **2016**, *32*, 9975-9981

- **Three-dimensional Atomic Force Microscopy Mapping at the Solid-Liquid Interface with Fast and Flexible Data Acquisition**
  H. Söngen, **M. Nalbach**, H. Adam, A. Kühnle
  Review of Scientific Instruments **2016**, *87*, 063704

- **Stabilization of Polar Step Edges on Calcite (10.4) by the Adsorption of Congo Red**
  R.Momper, **M. Nalbach**, K. Lichtenstein, R. Bechstein, A. Kühnle
  Langmuir **2015**, *31*, 7283-7287

- **How Deprotonation Changes Molecular Self-Assembly – An AFM Study in Liquid Environment**
  M. Schreiber, M. Eckardt, S. Klassen, H. Adam, **M. Nalbach**, L. Greifenstein, F. Kling, M. Kittelmann, R. Bechstein, A. Kühnle
  Soft Matter **2013**, *9*, 7145-7149

Contributions I have (co)-authored

- **Supramolecular Systems at Liquid–Solid Interfaces: General Discussion**
  D. Amabilino, I. Bâldea, P. Besenius, P. Beton, M. Blunt, M. Buck, N. Champness, L. Chi, S. Clarke, G. Costantini, S. De Feyter, Y. Diaz Fernandez, D. Dwivedi, K.-H. Ernst, A. Flood, B. Hirsch, R. Jones, A. Kühnle, M. Lackinger, T. Linderoth, N. Martsinovich, A. Mount, **M. Nalbach**, C.-M. Pradier, T. Rahman, R. Raval, N. Robinson, M. Sacchi, S. Schwaminger, S. Tait, P. Woodruff, H. Zuilhof
  Faraday Discussion **2017**, *204*, 1-26

- **Probing Properties of Molecule-Based Interface Systems: General Discussion and Discussion of the Concluding Remarks**
  D. Amabilino, I. Bâldea, J. Batteas, P. Beton, N. Bilbao, G. Costantini, J. Davidson, S. De Feyter, Y. Diaz Fernandez, K.-H. Ernst, B. Hirsch, A. Jabbarzadeh, R. Jones, A. Kühnle, M. Lackinger, Z. Li, N. Lin, T. Linderoth, N. Martsinovich, **M. Nalbach**, C.-M. Pradier, T. Rahman, R. Raval, N. Robinson, F. Rosei, M. Sacchi, M. Samperi, A. Sanz Matias, A. Saywell, Se. Schwaminger, S. Tait
  Faraday Discussion **2017**, *204*, 1-28

Publications in preparation

- **Influence of Initial pH on Calcite Nucleation and Growth Using the Ammonia Diffusion Method**
  M. Nalbach, M. Susewind, A. Kühnle
  in preparation

Talks

(presenting author underlined)

- **Comprehensive Control of Molecular Self-Assembly at the Calcite (10.4)-Water Interface**
  M. Nalbach, P. Raiteri, S. Klassen, S. Schäfer, J. D. Gale, R. Bechstein, A. Kühnle
  (27th Goldschmidt Conference, 2017, Paris, France)

- **Atomic Force Microscopy at Mineral-Water Interfaces: From High-Resolution Imaging to Chemical Identification**
  H. Söngen, H. Adam, S. Klassen, S. Seibert, M. Nalbach, R. Bechstein, A. Kühnle
  (27th Goldschmidt Conference, 2017, Paris, France)

- **High-Resolution Atomic Force Microscopy at the Mineral-Water Interface**
  M. Nalbach, H. Söngen, C. Marutschke, M. Schreiber, R. Bechstein, A. Kühnle
  (Kolloquium für Kristallographie und technische Mineralogie, 2017, Ludwig-Maximilians-Universität München, Germany)

- **Surface Restructuring of Calcite (10.4) in the Presence of Organic Additives**
  M. Nalbach, S. Klassen, R. Bechstein, A. Kühnle
  (The Granada-Münster Discussion Meeting, 2016, Münster, Germany)

- **Three-dimensional Atomic Force Microscopy Mapping at the Solid-Liquid Interface with Fast and Flexible Data Acquisition**
  H. Söngen, R. Bechstein, M. Nalbach, H. Adam, A. Kühnle
  (19th International Conference on Non-Contact Atomic Force Microscopy, 2016, Nottingham, UK)

- ***In-situ* Visualization of Molecular Self-Assembly and Surface Restructuring at the Mineral-Water Interface**
  M. Nalbach, M. Schreiber, R. Momper, S. Klassen, R. Bechstein, A. Kühnle
  (26th Goldschmidt Conference, 2016, Yokohama, Japan)

- **Surface Morphology Control Versus Molecular Self-Assembly on Calcite (10.4)**
  M. Nalbach, S. Klassen, H. Söngen, R. Bechstein, A. Kühnle
  (251st American Chemical Society National Meeting & Exposition, 2016, San Diego, USA)

- **Investigating the Mineral-Water Interface Using *in-situ* High-Resolution Atomic Force Microscopy Techniques**
  M. Nalbach, C. Marutschke, R. Momper, M. Schreiber, R. Bechstein, A. Kühnle
  (251st American Chemical Society National Meeting & Exposition, 2016, San Diego, USA)

- **Studying Molecular Self-Assembly on Calcite (10.4) in Liquid Environments**
  M. Nalbach, M. Schreiber, R. Momper, R. Bechstein, A. Kühnle
  (XIIIth International Symposium on Biomineralization (BiominXIII), 2015, Granada, Spain)

Poster Presentations

(presenting author underlined)

- **How to Control Molecular Self-Assembly at the Calcite (10.4)-Water Interface - An *in-situ* High-Resolution AFM Study**
  M. Nalbach, P. Raiteri, S. Klassen, S. Schäfer, J. D. Gale, R. Bechstein, A. Kühnle
  Complex Molecular Surfaces and Interfaces Faraday Discussion, 2017, Sheffield, United Kingdom)

- **Molecular Self-Assembly Versus Surface Restructuring During Calcite Dissolution**
  M. Nalbach, S. Klassen, R. Bechstein, A. Kühnle
  2nd German-French Summer School on noncontact atomic force microscopy, 2016, Osnabrück, Germany)

- **Exploring pH-Dependent $CaCO_3$ Nucleation and Growth Processes**
  M. Nalbach, M. Susewind, R. Bechstein, A. Kühnle
  (XIIIth International Symposium on Biomineralization (BiominXIII), 2015, Granada, Spain)

- **How Deprotonation Changes Molecular Self-Assembly - An AFM Study in Liquid Environment**
  M. Schreiber, M. Eckardt, S. Klassen, H. Adam, M. Nalbach, L. Greifenstein, F. Kling, M. Kittelmann, R. Bechstein, A. Kühnle
  (GDCh-Wissenschaftsforum Chemie 2013, Darmstadt, Germany)

- **Molecular Self-Assembly of Alizarin Red S on Calcite (10.4) in Liquid Environment**
  M. Schreiber, M. Eckardt, S. Klassen, H. Adam, M. Nalbach, L. Greifenstein, F. Kling, M. Kittelmann, R. Bechstein, A. Kühnle
  (16th International Conference on Non-Contact Atomic Force Microscopy, 2013, Maryland, USA)

Acknowledgment

An dieser Stelle möchte ich mich recht herzlich bei allen Menschen bedanken, die mich während der Promotion unterstützt und mir es dadurch ermöglicht haben, diese Arbeit zu schreiben.

> *Because sometimes... the truth isn't good enough. Sometimes people deserve more. Sometimes people deserve to have their faith rewarded.*
>
> **— The Dark Knight**

Mein ganz besonderer Dank gilt zuallererst:

- [redacted] für die herausragende Betreuung dieser Doktorarbeit, für ihre beispiellose Unterstützung bei Fragen rund um die Promotion, für ihr entgegengebrachtes Vertrauen und für ihr stets offenes Ohr. Nicht zu vergessen, die schöne Dienstreise nach San Diego, sowie den herzlichen Empfang in Osnabrück.
- [redacted] für die Übernahme des Zweitgutachtens.
- [redacted] für die Übernahme des Prüfungsvorsitzes.

I am very grateful to my collaborators:

- [redacted] for the computational insights into Benzopurpurine at the calcite-water interface and his enormous support from the other end of the world.
- [redacted] for the idea of the "most hydrophobic region" and his very helpful English native speaker assistance.
- [redacted] for the organophosphonate molecules, his patience but also for his encouragement in the last two years.

Weiterhin möchte ich ganz besonders danken:

Meinen aktuellen und ehemaligen Arbeitskollegen/innen für die gute Zusammenarbeit und die nette Arbeitsatmosphäre. Im Einzelnen möchte ich danken:

- … [redacted] für das Beantworten meiner unendlichen Anzahl an Fragen, für seine immer phänomenal hilfreichen Ideen und Ratschläge, sowie für die Initiierung des Kicker Managerspiels.

- … [redacted] für das Wiederbeleben des blauen Lasers, für den HF2, für die Vielzahl an (Fach-)Gesprächen mit und ohne 50° Nord und für seinen entschlossenen Nachdruck beim Finalisieren dieser Doktorarbeit.

- … [redacted] für ihre unbezahlbare Unterstützung bei der Durchführung der Experimente, für die sportlichen und nicht sportlichen Challenges und für die schöne Dienstreise nach Fernost.

- … [redacted] für ihre umfassende mütterliche Fürsorge, für ihre allzeit hilfreiche Stilberatung und für ihren grünen Daumen im schönsten Büro der Universität.

- … [redacted] for teaching me the most important Spanish words, for the unforgettable days in the office during weekends and holidays and for his all time supply with Lomo.

- … [redacted] dafür, dass er mir als Doktorbuddy immer zur Seite gestanden hat.

- … [redacted] für die hervorragenden dienstlichen Fotoshootings und die nachmittäglichen Auszeiten.

- … [redacted] für ihre administrative Unterstützung.

- … [redacted] für ihre liebenswerte Art und Weise Fragen zu stellen.

- … [redacted] für die Pionierarbeit mit Benzopurpurin.

- … [redacted] für unvergessliche Momente in der Mainzer Wand.

- … [redacted] für die herausragende Partie Tennis in Stanford und für seinen Heimatort Rüegsau.

· · · [redacted] für N_2 am Morgen, die vielen Fußball-Fachgespräche und für seinen Amazon Prime Account.

· · · [redacted] für das Zitat von Kurfürst Friedrich Wilhelm von Brandenburg, für die Weitergabe seines umfassenden Wissens vor und während der Doktorarbeit und für die kulinarischen Reisen durch Mainz.

· · · [redacted] für die umfassenden Vorarbeiten mit *in-situ* high-resolution AFM auf Calcit (10.4), für Alizarinrot S und Kongorot und für die vielen bestärkenden Telefonate nach Feierabend.

· · · [redacted] für die Ernennung zum AFM-Präsidenten, für seine stetigen Glückwünsche und für seine immer aktuellen Flughafenstandorte.

· · · [redacted] für die legendäre OC-Grundpraktikumsparty, für seine unvergesslichen Sprüche und für den gemeinsamen Kauf des Lego Superstern-zerstörers.

· · · [redacted] für seine rund-um-die-Uhr Bewerbungsberatung, für den gemeinsamen Humor und für die schöne Zeit im Labor mit Ronny Schäfer.

· · · [redacted] for the international supply with not accessible publications, for the tremendous amount of postcards from all over the world and for her English native speaker proofreading.

Zu guter Letzt danke ich:

· · · [redacted] und besonders [redacted], die immer an mich geglaubt und unterstützt haben.

· · · [redacted] für die schönen Momente abseits der Wissenschaft.

· · · [redacted], dass sie für mich da ist und so viel Geduld für und Verständnis mit mir hat.

Colophon

This thesis was typeset with LaTeX 2_ε. It uses the *Clean Thesis* style developed by Ricardo Langner. The design of the *Clean Thesis* style is inspired by user guide documents from Apple Inc.

Download the *Clean Thesis* style at `http://cleanthesis.der-ric.de/`.